Supplementary Information

TiO_2-facet-dependent reconstruction of Pt nanoparticles during CO oxidation

Jihun Kim†[1], Yunkyung Kim†[2], Daewon Oh[1], Seokhyun Choung[2], Hyeongeon Lee[1], Hogyun Lee[1], Eonu Nam[1], Shinjae Lee[1], Jeongjin Kim[3], Sinmyung Yoon[1,4*], Jeong Woo Han[2*], and Kwangjin An[1*]

[1]*School of Energy and Chemical Engineering, Ulsan National Institute of Science and Technology (UNIST), Ulsan 44919, Republic of Korea*
[2]*Department of Materials Science and Engineering, Research Institute of Advanced Materials, Seoul National University, Seoul 08826, Republic of Korea.*
[3]*Pohang Light Source II, Pohang University of Science and Technology (POSTECH), Pohang, Gyeongbuk 37673, Republic of Korea*
[4]*Delaware Energy Institute, University of Delaware, 221 Academy St., Newark, DE 19716, United States*

†These authors contributed equally to this work. Correspondence and requests for materials should be addressed to S.Y. (smyoon@udel.edu), J.W.H. (jwhan98@snu.ac.kr) and K.A. (kjan@unist.ac.kr).

This file includes:

Supplementary Figs. 1 to 62

Supplementary Table 1 to 8

Supplementary Note 1 to 14

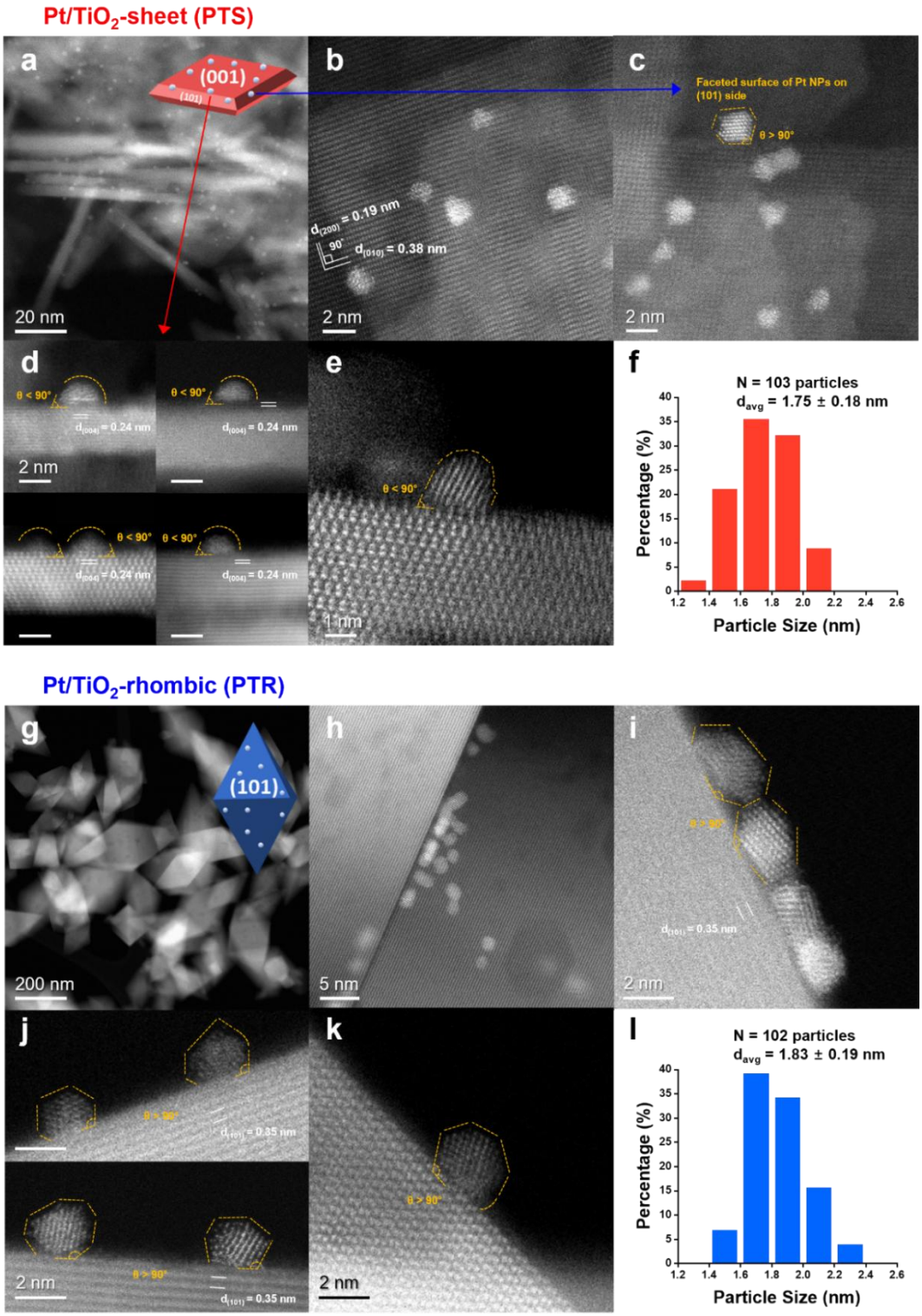

Supplementary Figure 1. Morphology and NP size distributions of as-prepared Pt/TiO_2 catalysts. (a–e, g–k) HAADF-STEM images of the as-prepared Pt/TiO_2 catalysts: (a–e) PTS with exposed (001) facets and (g–k) PTR with exposed (101) facets. (f, l) Corresponding histograms showing the Pt NP size distributions for (f) PTS and (l) PTR. For PTS, Pt NPs located on the TiO_2(001) facet are marked with red arrows, whereas those positioned on the nanosheet (101) termination are indicated with blue arrows. The Pt morphology observed on the nanosheet (101) termination resembles that on the TiO_2(101) facet in PTR, consistent with facet-dependent Pt morphology.

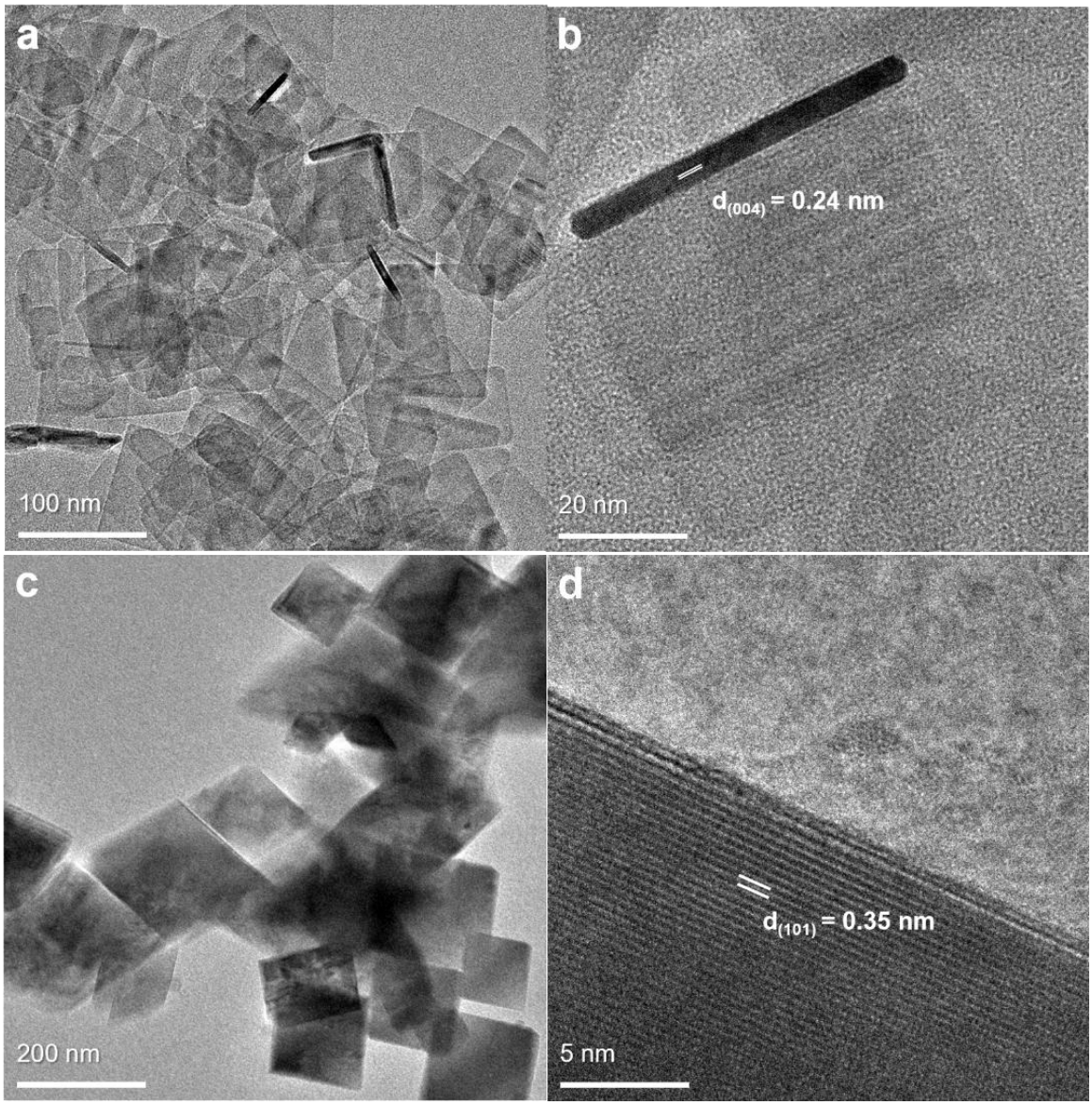

Supplementary Figure 2. Morphology-controlled synthesis of TiO_2 crystals exposing distinct crystal facets. (a–d) TEM images of as-synthesized TiO_2 crystals with controlled morphologies: (a–b) nanosheets predominantly exposing the (001) facet and (c–d) rhombic-shaped crystals primarily exposing the (101) facet.

Supplementary Table 1. Physicochemical properties of Pt/TiO_2 catalysts, including average Pt NP size, Pt loading, CO chemisorption capacity, and dispersion.

Catalysts	Pt size by TEM (nm)[a]	Pt (wt %)[b]	Chemisorbed CO ($mmol \cdot g^{-1}$)[c]	D_{Pt} (%)[d]
PTS	1.75 ± 0.2	0.32	0.00897	51.5
PTR	1.83 ± 0.2	0.45	0.01038	49.1
PtA	1.93 ± 0.3	0.43	0.00984	44.8

[a]Average Pt NP size determined from HAADF-STEM analysis.

[b]Pt content measured by ICP-OES

[c] Chemisorbed CO amount estimated by single-pulse injection of 2% CO/He (30 sccm, 5 s).

[d]Pt dispersion (D_{Pt}) calculated using CO chemisorption and ICP-OES data according to D_{Pt} (%) = X_M N_s / N_T × 100, assuming a Pt/CO stoichiometry (X_M) of 1:1. N_T is the total number of Pt atoms per unit weight and *N*s is the number of exposed Pt atoms.

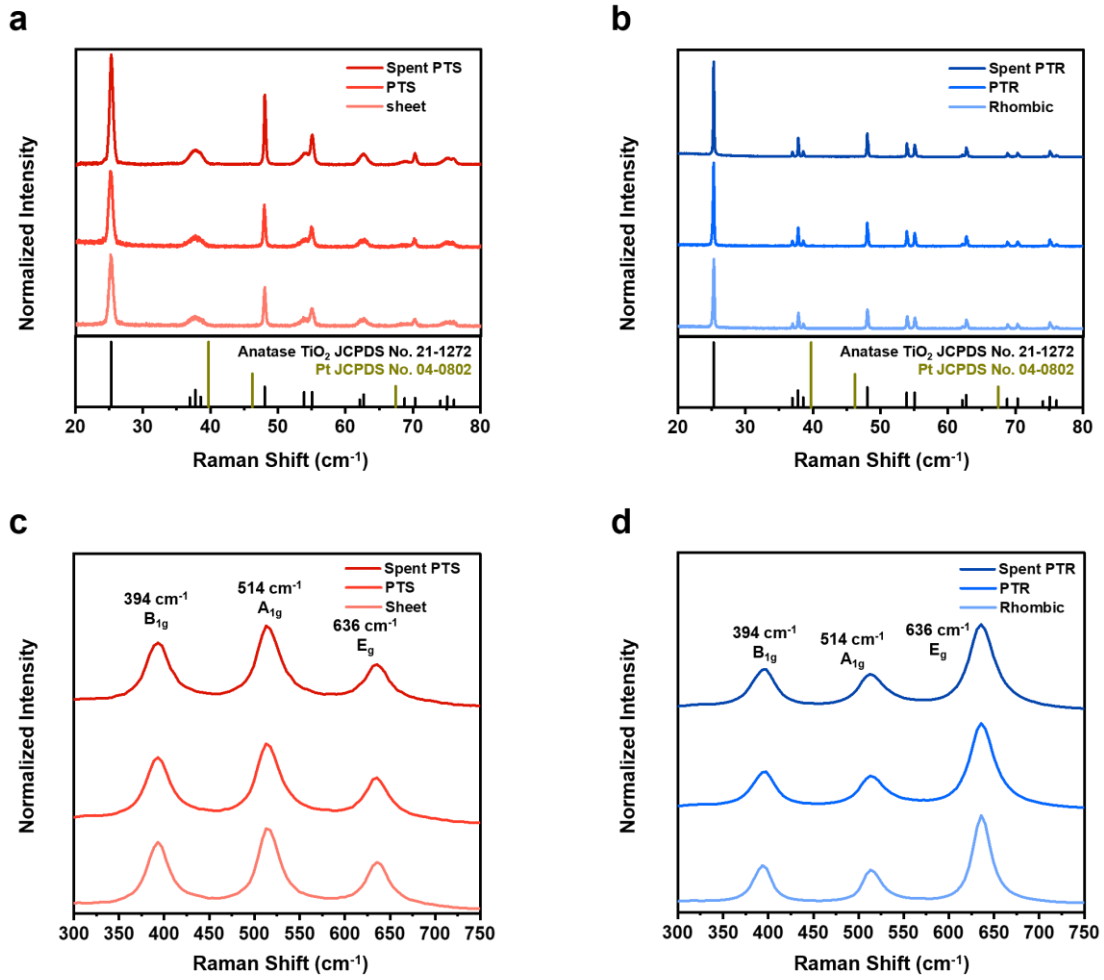

Supplementary Figure 3. Structural stability of Pt/TiO_2 catalysts. (a–b) XRD patterns and (c–d) Raman spectra of TiO_2 supports and Pt/TiO_2 catalysts before and after CO oxidation. (a, c) Sheet-shaped TiO_2 with predominantly exposed (001) facets, fresh PTS, and spent PTS; (b, d) Rhombic TiO_2 with predominantly exposed (101) facets, fresh PTR, and spent PTR. Spent catalysts were prepared by treating the samples at 240 °C for 2 h (CO/O_2 = 1).

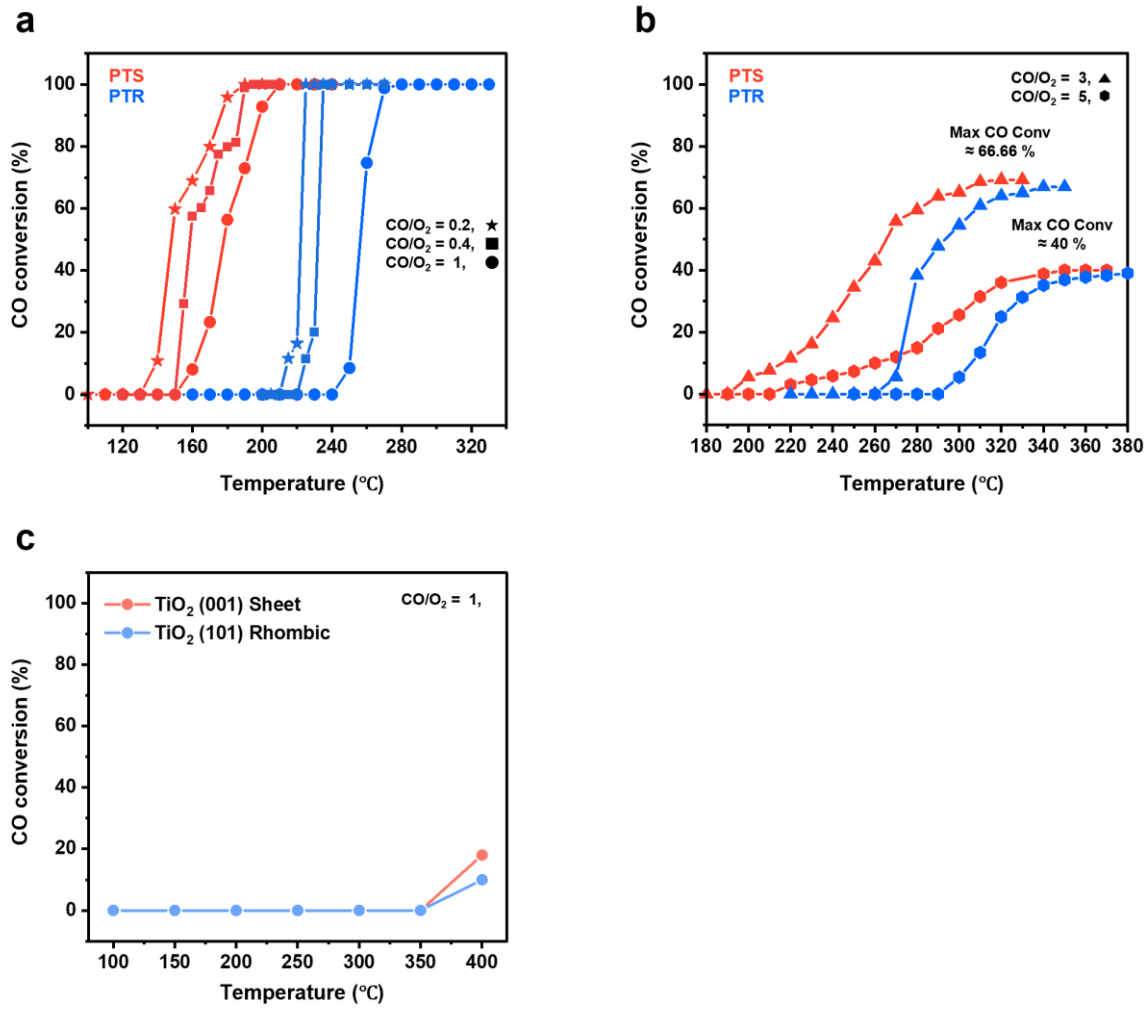

Supplementary Figure 4. Catalytic CO oxidation under different CO/O_2 reaction atmospheres. Temperature-dependent CO conversion profiles of PTS and PTR catalysts under varying CO/O_2 ratios. (a) Conversion curves under O_2-rich to limited conditions: CO/O_2 = 0.2 (1% CO / 5% O_2, ★), 0.4 (1% CO / 2.5% O_2, ■), and 1 (1% CO / 1% O_2, ●). (b) Conversion curves under CO-rich conditions: CO/O_2 = 3 (3% CO / 1% O_2, ▲) and 5 (5% CO / 1% O_2, ⬢). (c) CO conversion curves of pristine TiO_2 under CO/O_2 = 1 condition. The total gas flow rate was maintained at 50 mL·min^{-1} for all measurements.

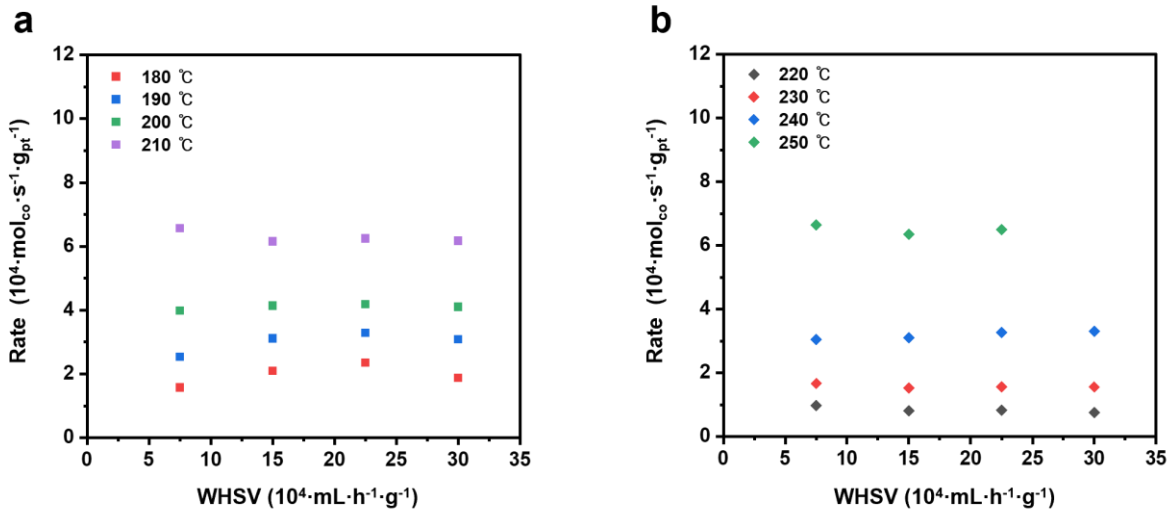

Supplementary Figure 5. Verification of kinetic control during CO oxidation. CO oxidation rates over a range of total gas flow rates for (a) PTS and (b) PTR catalysts. The constant reaction rates across varying flow rates confirm that the CO oxidation is controlled by surface kinetics rather than mass transfer limitations. The apparent activation energy (E_a) was calculated under a total flow rate of 100 mL·min^{-1} with a CO/O_2 ratio of 1, specifically within the kinetically relevant regime (15% CO conversion).

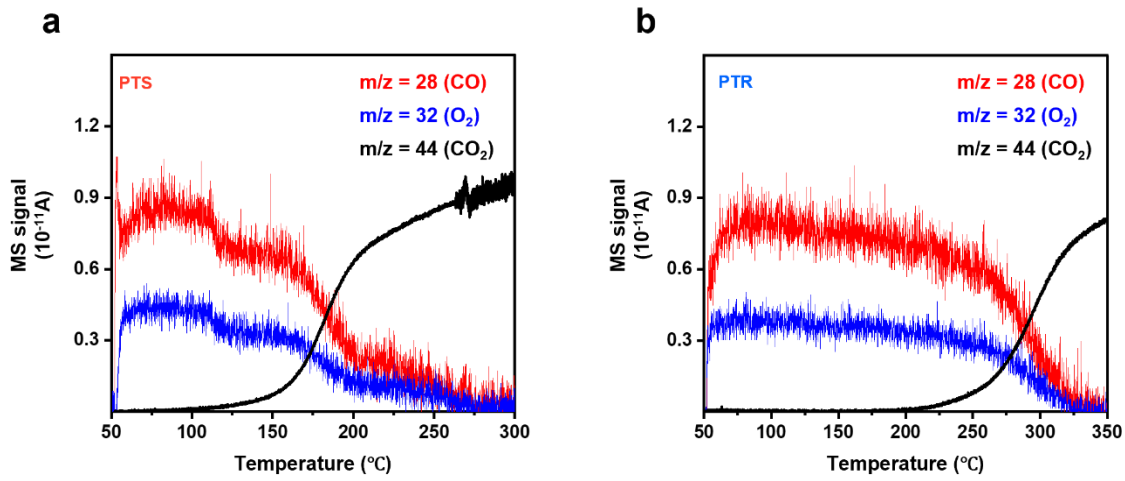

Supplementary Figure 6. CO-assisted reducibility of Pt/TiO_2 catalysts. CO-TPR profiles and corresponding CO_2 mass spectrometry (MS) signals for (a) PTS and (b) PTR catalysts. The CO_2 MS signal intensities reflect the reducibility and surface oxygen availability of the Pt/TiO_2 catalysts under CO-rich conditions, providing insights into the MvK reaction pathway.

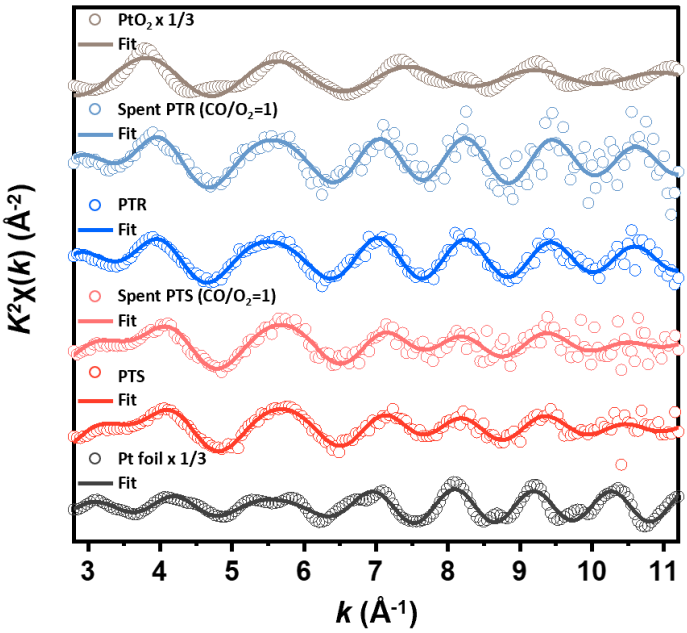

Supplementary Figure 7. Pt local coordination environments revealed by Pt *L*$_3$-edge EXAFS. Pt L_3-edge EXAFS k^2-weighted χ(k) spectra of fresh and spent Pt/TiO_2 catalysts, compared with Pt foil and PtO_2 reference samples. Spent catalysts (CO/O_2 = 1) were prepared by treating the samples at 240 °C for 2 h.

Supplementary Table 2. EXAFS fitting parameters of Pt/TiO_2 catalysts. Fitting results of the Pt L_3-edge EXAFS spectra for fresh and spent Pt/TiO_2 catalysts under different CO/O_2 ratios (0.2, 1, and 5), compared with Pt foil and PtO_2 references. Spent catalysts were prepared by treating the samples at 240 °C for 2 h (CO/O_2 = 0.2 and 1) and 350 °C for 2 h (CO/O_2 = 5). Further details regarding the temperature selection criteria are provided in Supplementary Note 2.

Catalysts	shell	CN	d (Å)	σ^2	E_0 shift	R factor
Pt foil	Pt–Pt	12.0	2.76 ± 0.01	0.004 ± 0.001	7.1 ± 0.7	0.0095
PtO_2	Pt–O	6.0	2.02 ± 0.01	0.003 ± 0.001	10.5 ± 1.5	0.0063
Fresh PTS	Pt–Pt	6.4 ± 1.2	2.71 ± 0.01	0.010 ± 0.002	5.5 ± 1.7	0.0113
	Pt–O	1.6 ± 0.4	1.97 ± 0.01	0.005 ± 0.003		
Spent PTS, O_2-rich (CO/O_2=0.2)	Pt–Pt	6.6 ± 2.2	2.74 ± 0.02	0.010 ± 0.003	8.2 ± 2.5	0.0063
	Pt–O	1.9 ± 0.7	2.00 ± 0.02	0.005 ± 0.004		
Spent PTS (CO/O_2=1)	Pt–Pt	6.8 ± 1.7	2.70 ± 0.02	0.011 ± 0.003	4.0 ± 1.9	0.0162
	Pt–O	1.7 ± 0.4	1.96 ± 0.02	0.004 ± 0.003		
Spent PTS, CO-rich (CO/O_2=5)	Pt–Pt	8.6 ± 1.6	2.73 ± 0.01	0.010 ± 0.002	5.3 ± 1.6	0.0096
	Pt–O	1.3 ± 0.6	1.97 ± 0.02	0.005 ± 0.004		
Fresh PTR	Pt–Pt	8.1 ± 1.2	2.74 ± 0.01	0.008 ± 0.001	6.7 ± 1.7	0.0077
	Pt–O	1.4 ± 0.8	2.00 ± 0.03	0.011 ± 0.009		
	Pt–Pt	8.2 ± 1.4	2.74 ± 0.01	0.007 ± 0.001	6.2 ± 1.3	0.0115

Spent PTR, O_2-rich (CO/O_2=0.2)	Pt–O	1.2 ± 0.5	1.97 ± 0.01	0.007 ± 0.005		
Spent PTR (CO/O_2=1)	Pt–Pt	8.2 ± 1.2	2.74 ± 0.01	0.007 ± 0.001	7.0 ± 1.3	0.0032
	Pt–O	1.2 ± 0.4	1.97 ± 0.02	0.005 ± 0.004		
Spent PTR, CO-rich (CO/O_2=5)	Pt–Pt	9.8 ± 0.8	2.75 ± 0.01	0.007 ± 0.001	6.3 ± 0.6	0.0033
	Pt–O	1.1 ± 0.4	1.99 ± 0.02	0.010 ± 0.006		

CN represents the average coordination number around the Pt absorber atom, σ^2 is the Debye–Waller factor, *d* is the bond distance, and R-factor indicates the quality of the fit. The amplitude reduction factor (S_0^2) was fixed at 0.77, as determined from Pt foil fitting. EXAFS fitting was performed using k^2-weighted spectra over the ranges: 2.8(3.0) < *k* < 10.8(11.2) Å^{-1} and 1(1.3) < *r* < 3.3(3.5) Å. Only single-scattering paths from the first coordination shell were included in the EXAFS fitting.

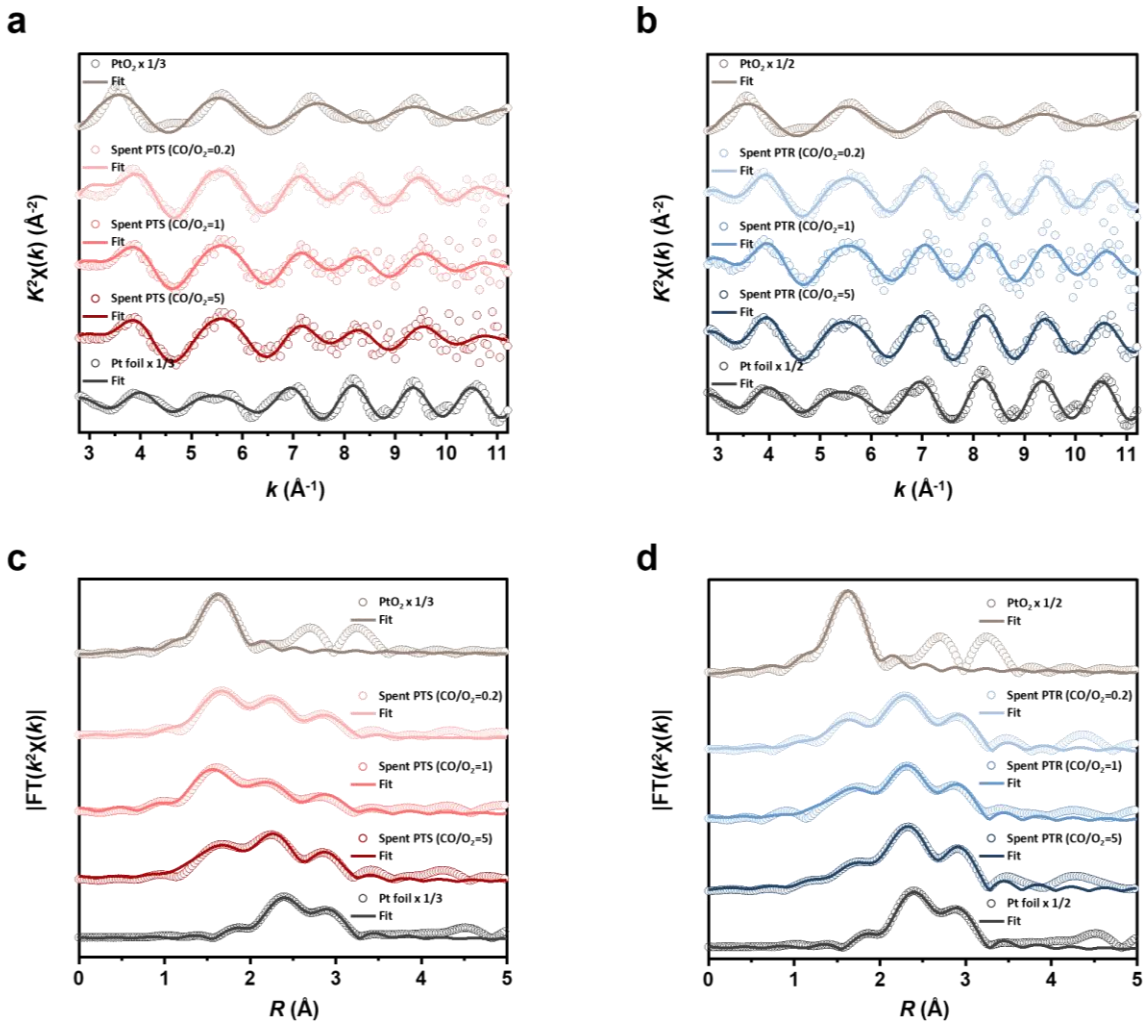

Supplementary Figure 8. EXAFS analysis of Pt local structures after CO oxidation. (a, b) k^2-weighted $\chi(k)$ functions of Pt L_3-edge EXAFS spectra for spent Pt/TiO_2 catalysts after CO oxidation under different CO/O_2 ratios (0.2, 1, and 5). (c, d) Corresponding FT-EXAFS spectra and fitting results, showing the local coordination environment of Pt after catalytic reaction. Spent catalysts were prepared by treating the samples at 240 °C for 2 h (CO/O_2 = 0.2 and 1) and 350 °C for 2 h (CO/O_2 = 5). Further details regarding the temperature selection criteria are provided in Supplementary Note 2.

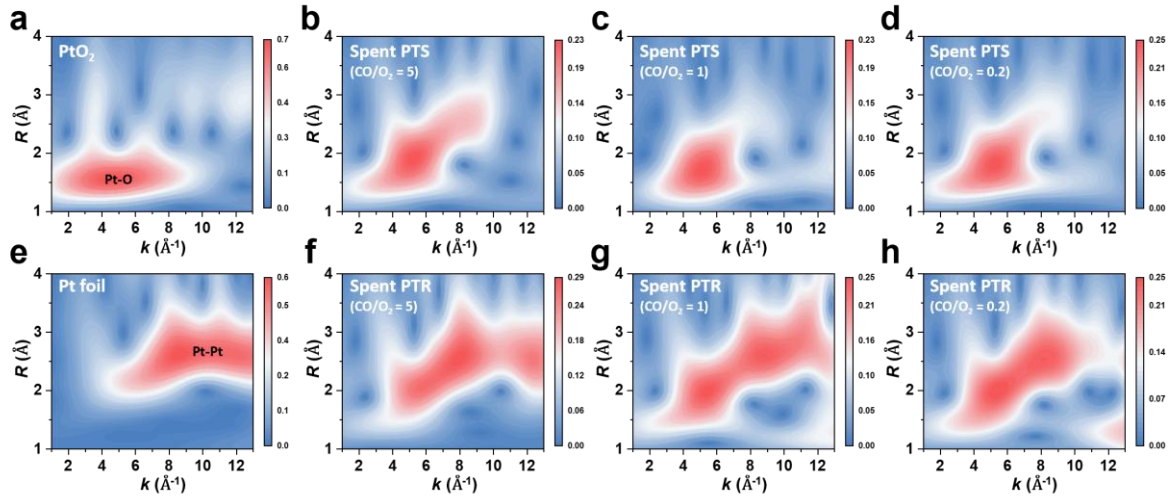

Supplementary Figure 9. Wavelet transform analysis of Pt coordination under different reaction atmospheres. WT contour maps of $k^2\chi(k)$ functions from Pt L_3-edge EXAFS for spent Pt/TiO_2 catalysts after CO oxidation under various CO/O_2 ratios, compared with reference materials: (a) PtO_2, (b–d) spent PTS at CO/O_2 = 5, 1, and 0.2, respectively, (e) Pt foil, and (f–h) spent PTR at CO/O_2 = 5, 1, and 0.2, respectively. Spent catalysts were prepared by treating the samples at 240 °C for 2 h (CO/O_2 = 0.2 and 1) and 350 °C for 2 h (CO/O_2 = 5). Further details regarding the temperature selection criteria are provided in Supplementary Note 2. These maps visualize changes in Pt coordination and bonding environments induced by different reaction conditions.

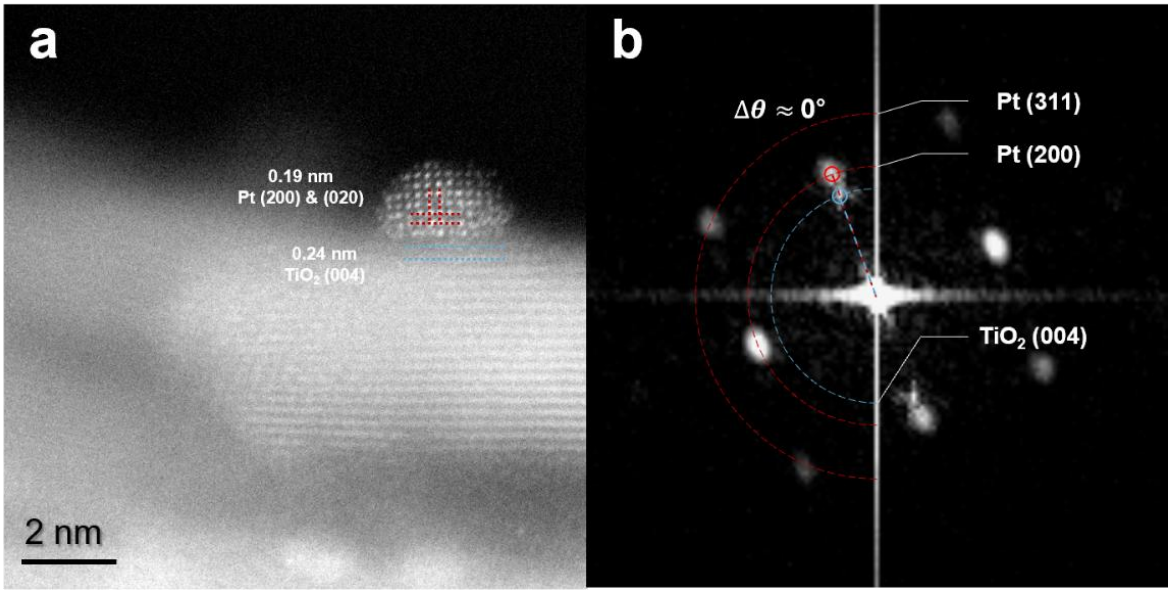

Supplementary Figure 10. Atomic-scale structure of reconstructed Pt NPs on TiO_2(001). (a) HAADF-STEM image of the spent PTS catalyst after CO oxidation. (b) Corresponding fast Fourier transform (FFT) pattern image, indicating lattice alignment and potential epitaxial relationship between Pt and the TiO_2(001) facet. Spent catalysts were prepared by treating the samples at 240 °C for 2 h (CO/O_2 = 1)

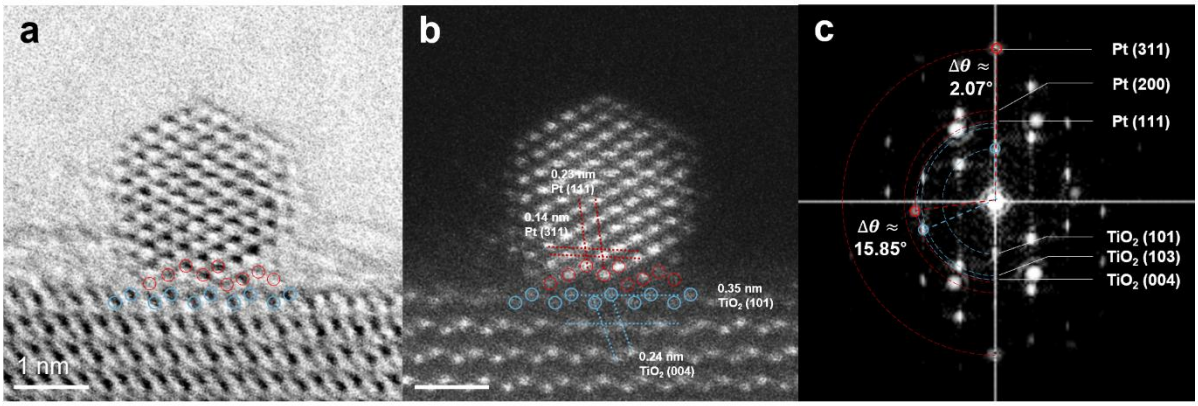

Supplementary Figure 11. Atomic-scale structure of reconstructed Pt NPs on TiO_2(101). (a) Bright-field and (b) dark-field STEM images of the spent PTR catalyst after CO oxidation. (c) Corresponding FFT pattern of image (b). The positions of Pt and Ti atoms in (b) are indicated by red and blue circles, respectively, based on contrast differences observed in (a), highlighting the lattice mismatches and interface step structures between Pt and the TiO_2(101) facet. Spent catalysts were prepared by treating the samples at 240 °C for 2 h (CO/O_2 = 1)

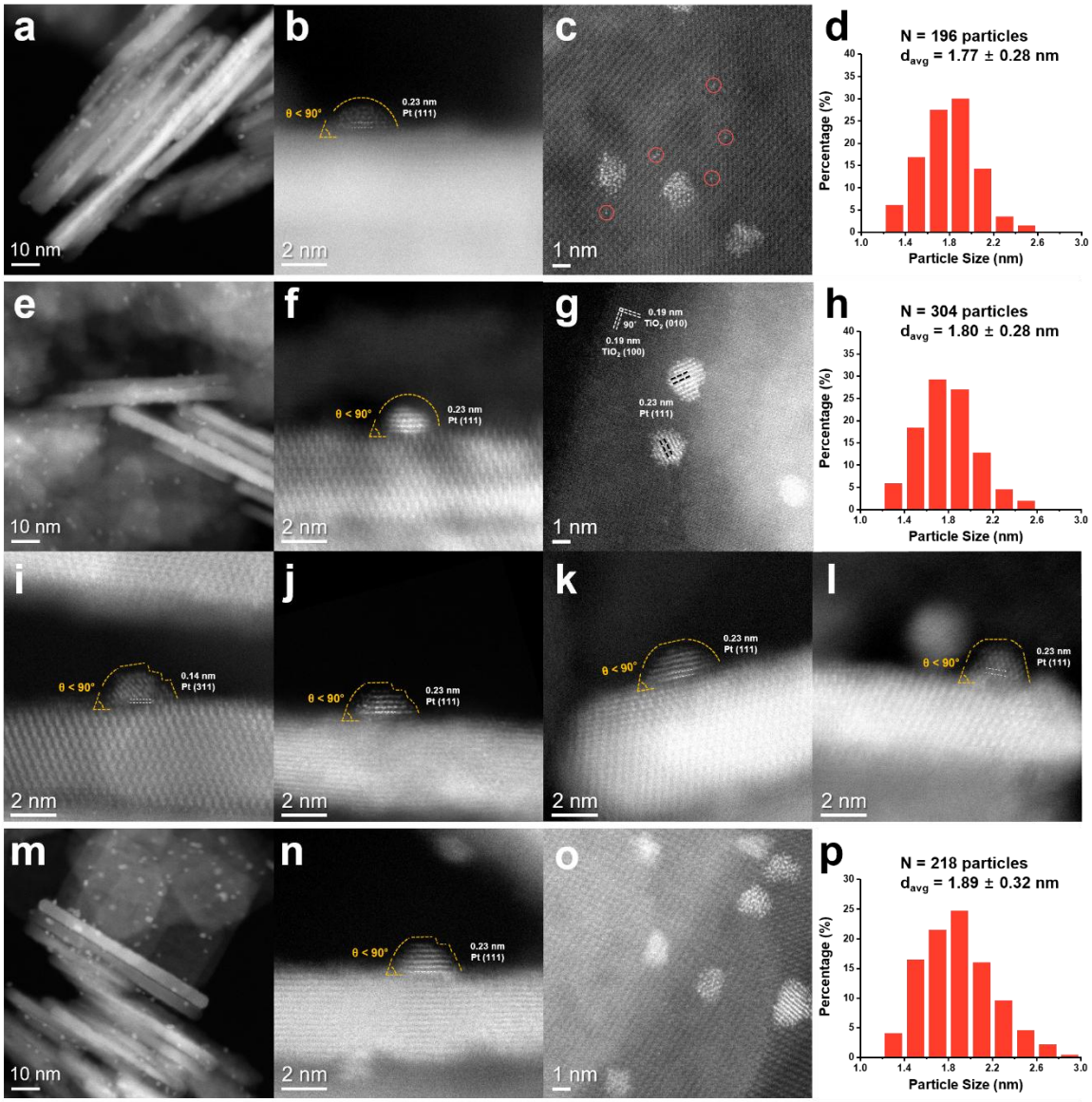

Supplementary Figure 12. Facet-dependent reconstruction of Pt NPs on TiO_2(001). HAADF−STEM images and corresponding Pt NP size distributions of the spent PTS catalyst after CO oxidation under varying CO/O_2 ratios: (a–d) CO/O_2 = 0.2, (e–l) CO/O_2 = 1, and (m–p) CO/O_2 = 5. Each set shows representative NP morphology and size histogram, indicating facet-dependent reconstruction behavior of Pt on TiO_2(001). For CO/O_2 = 0.2 and 1, the catalysts were treated at 240 °C for 2 h to prevent thermally induced sintering while ensuring that the CO-adsorbate-induced reconstruction process is fully reflected. For CO/O_2 = 5, the spent catalyst was treated at 350 °C for 2 h, corresponding to the maximum-conversion temperature of the undiluted PTR catalyst. No significant sintering of the spent PTS catalyst was observed across all conditions. Further details regarding the temperature selection criteria are provided in Supplementary Note 2.

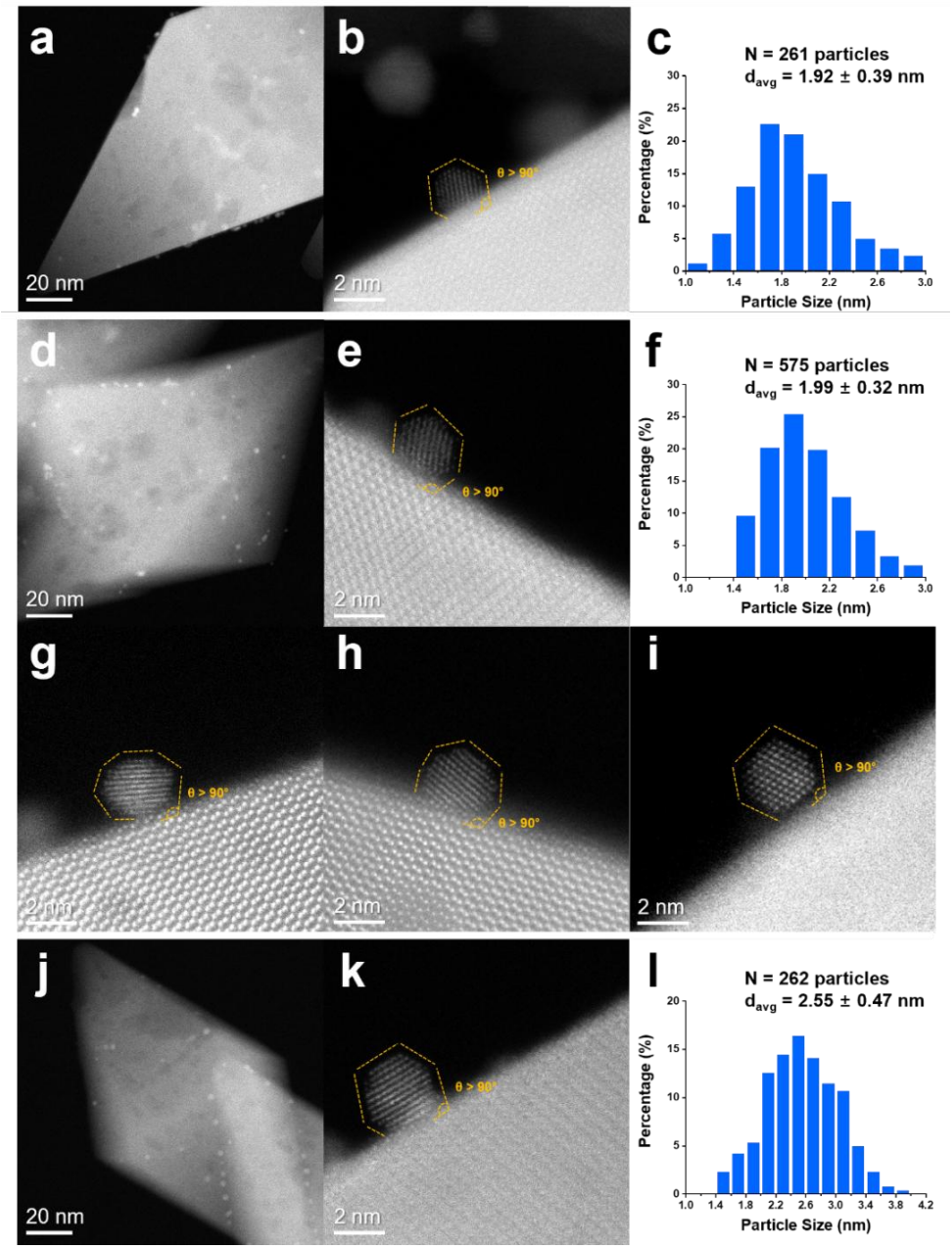

Supplementary Figure 13. Facet-dependent reconstruction of Pt NPs on TiO_2(101). HAADF−STEM images and corresponding Pt NP size distributions of the spent PTR catalyst after CO oxidation under various CO/O_2 ratios: (a–c) CO/O_2 = 0.2, (d–i) CO/O_2 = 1, and (j–l) CO/O_2 = 5. Each set shows representative NP morphology and size histogram, indicating facet-dependent reconstruction behavior of Pt on TiO_2(101). For CO/O_2 = 0.2 and 1, the catalysts were treated at 240 °C for 2 h to prevent thermally induced sintering while ensuring that the CO-adsorbate-induced reconstruction process is fully reflected. For CO/O_2 = 5, the spent catalyst was treated at 350 °C for 2 h, corresponding to the maximum-conversion temperature of the undiluted PTR catalyst; slight sintering was observed under this condition. Further details regarding the temperature selection criteria are provided in Supplementary Note 2.

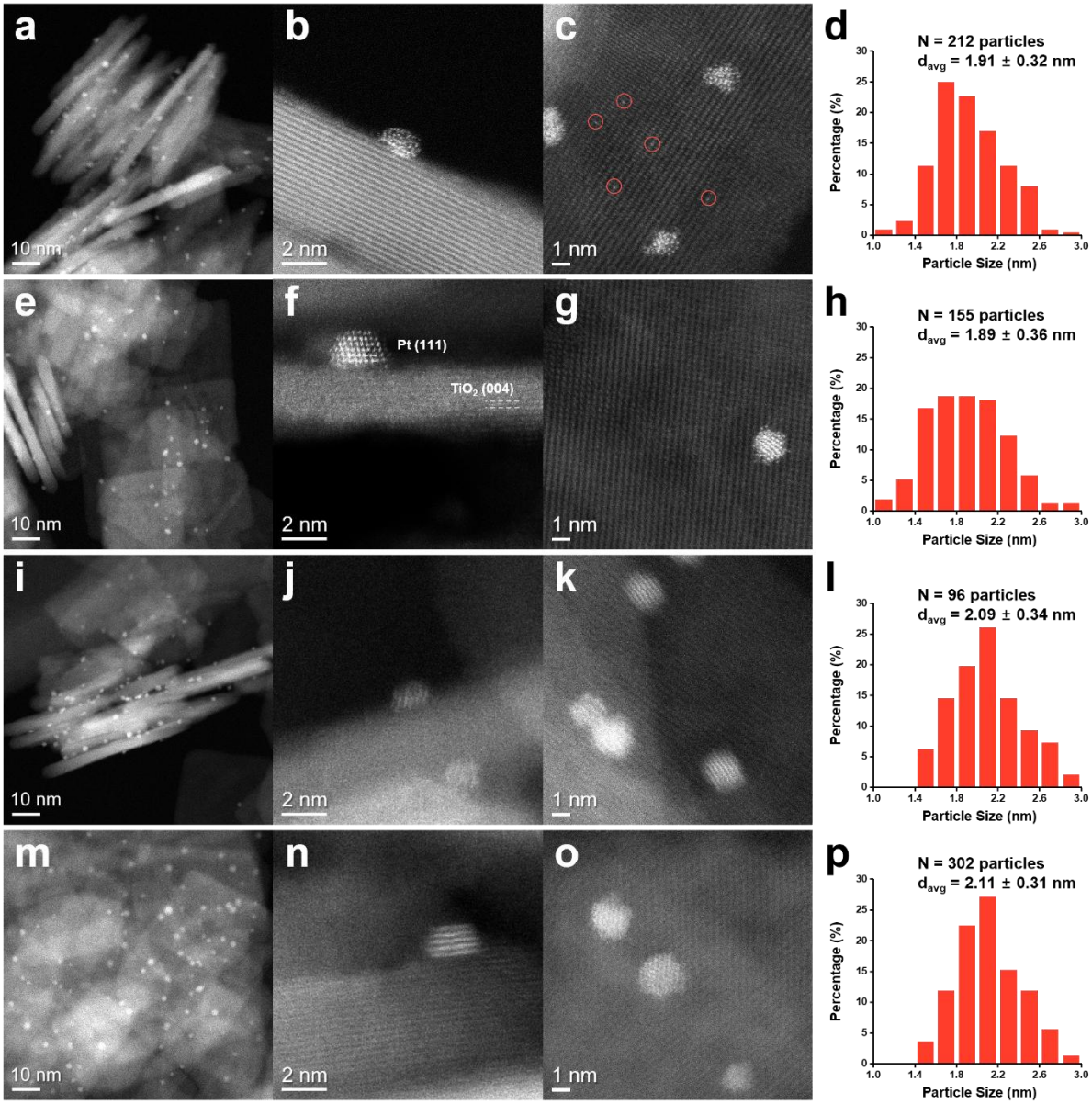

Supplementary Figure 14. Facet-dependent reconstruction of Pt NPs on TiO_2(001) under high-temperature reaction conditions. HAADF−STEM images and corresponding Pt NP size distributions of the spent PTS catalyst after CO oxidation under varying CO/O_2 ratios: (a–d) CO/O_2 = 0.2, (e–h) CO/O_2 = 1, (i–l) CO/O_2 = 3, and (m–p) CO/O_2 = 5. Each set shows representative NP morphology and size histogram, indicating facet-dependent reconstruction behavior of Pt on TiO_2(001). Spent catalysts were prepared by treating the samples at 300 °C for 2 h (CO/O_2 = 0.2 and 1), 350 °C for 2 h (CO/O_2 = 3), and 400 °C for 2 h (CO/O_2 = 5). No significant sintering of the spent PTS catalyst was observed across all conditions. Further details regarding the temperature selection criteria are provided in Supplementary Note 2.

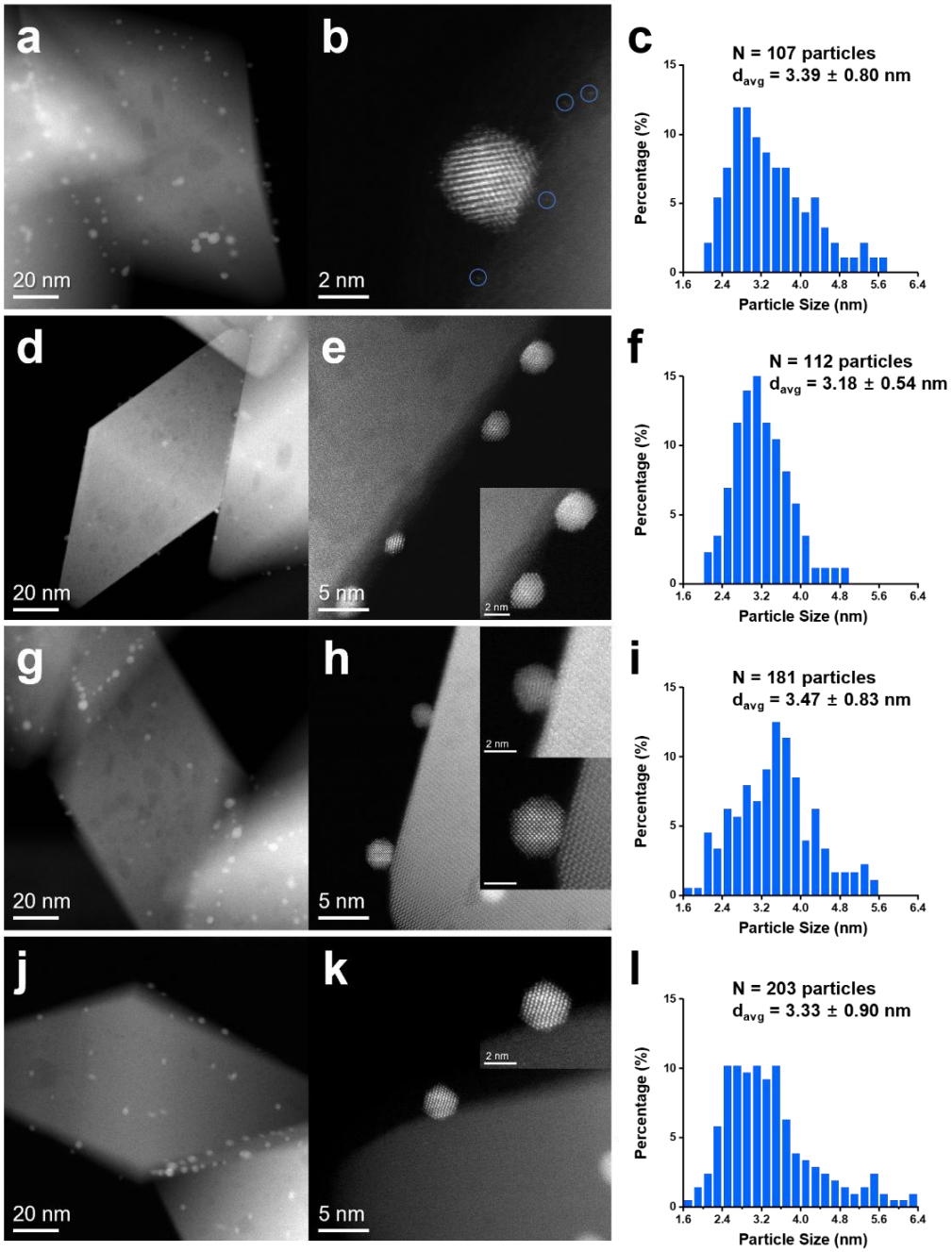

Supplementary Figure 15. Facet-dependent reconstruction of Pt NPs on TiO_2(101) under high-temperature reaction conditions. HAADF−STEM images and corresponding Pt NP size distributions of the spent PTR catalyst after CO oxidation under various CO/O_2 ratios: (a–c) CO/O_2 = 0.2, (d–f) CO/O_2 = 1, (g–i) CO/O_2 = 3, and (j–l) CO/O_2 = 5. Each set shows representative NP morphology and size histogram, indicating facet-dependent reconstruction behavior of Pt on TiO_2(101). Spent catalysts were prepared by treating the samples at 300 °C for 2 h (CO/O_2 = 0.2 and 1), 350 °C for 2 h (CO/O_2 = 3), and 400 °C for 2 h (CO/O_2 = 5). Significant sintering of the spent PTR catalyst was observed across all conditions, indicating intrinsically weaker Pt–TiO_2 interactions compared with PTS. Further details regarding the temperature selection criteria are provided in Supplementary Note 2.

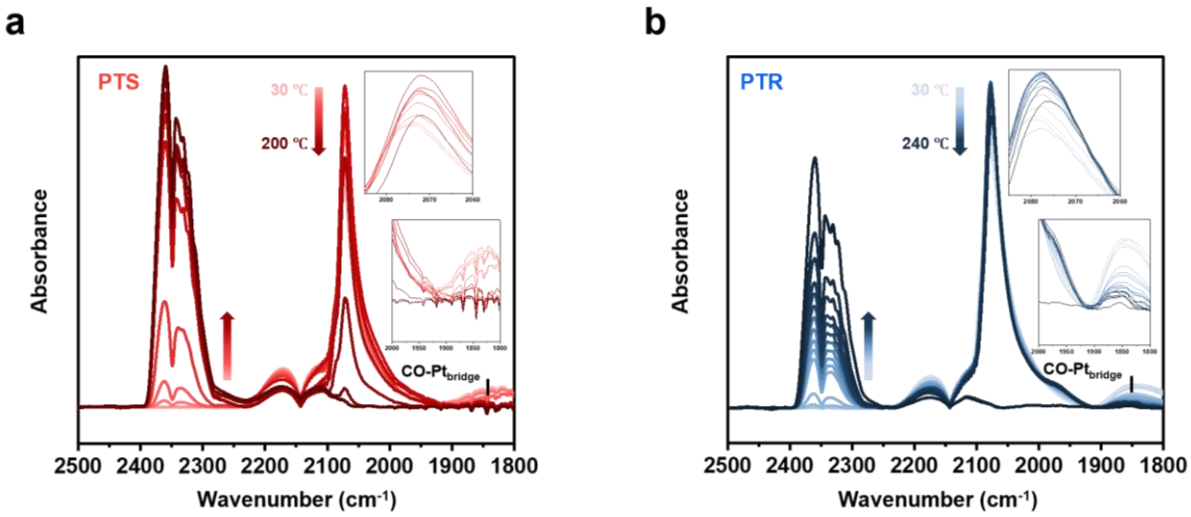

Supplementary Figure 16. Temperature-dependent evolution of surface species during CO oxidation. Full *in situ* DRIFTS spectra of (a) PTS and (b) PTR catalysts recorded under CO oxidation conditions (CO/O_2 = 1) at various temperatures. The spectra capture the temperature-dependent evolution of surface species, including CO adsorption and CO_2 formation.

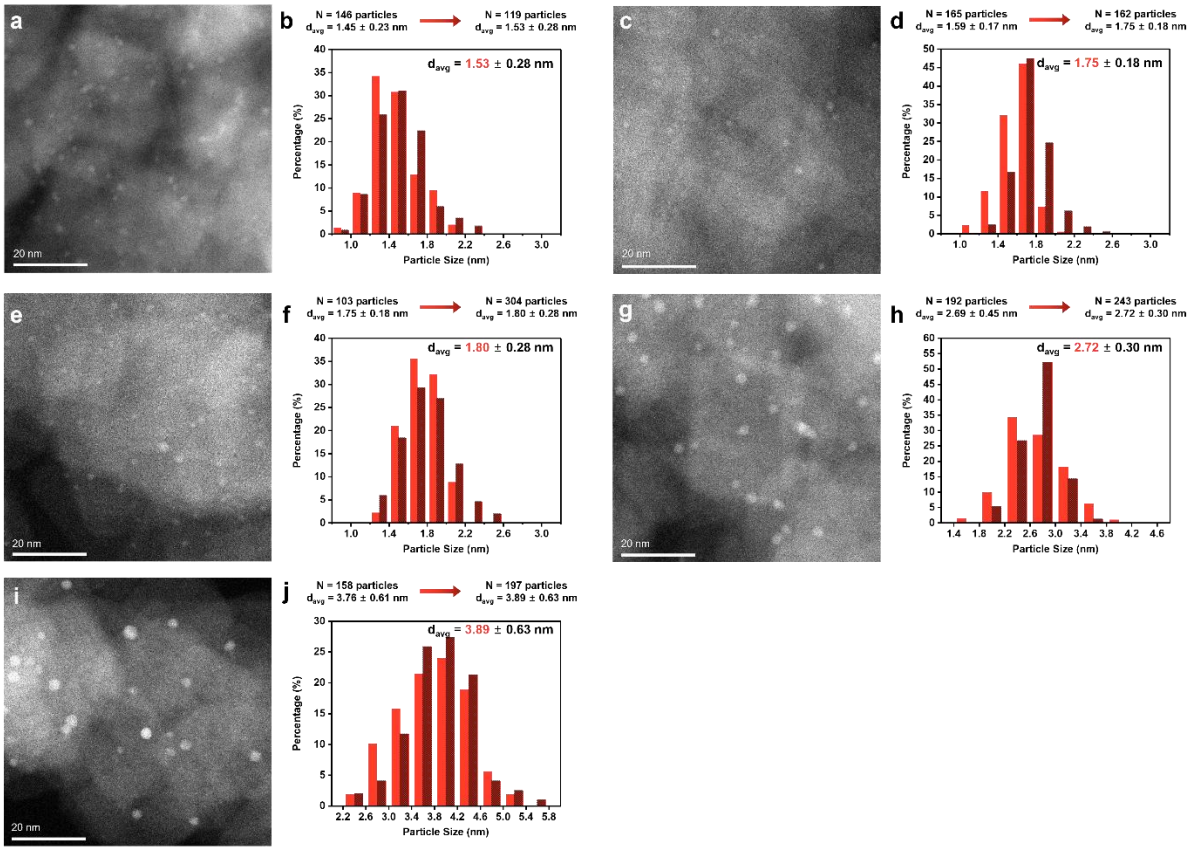

Supplementary Figure 17. Size distributions of Pt/TiO_2(001) catalysts with controlled Pt sizes. HAADF–STEM images and corresponding Pt NP size distributions of the size-controlled Pt/TiO_2(001) catalysts after CO oxidation, with final Pt sizes of (a, b) 1.53 nm, (c, d) 1.75 nm, (e, f) 1.80 nm, (g, h) 2.72 nm, and (i, j) 3.89 nm. Each set shows the post-reaction STEM image together with the corresponding pre- and post-reaction size distributions. All samples were treated at 240 °C for 2 h under CO/O_2 = 1 to prevent thermal sintering while ensuring that CO-adsorbate-induced reconstruction is reflected.

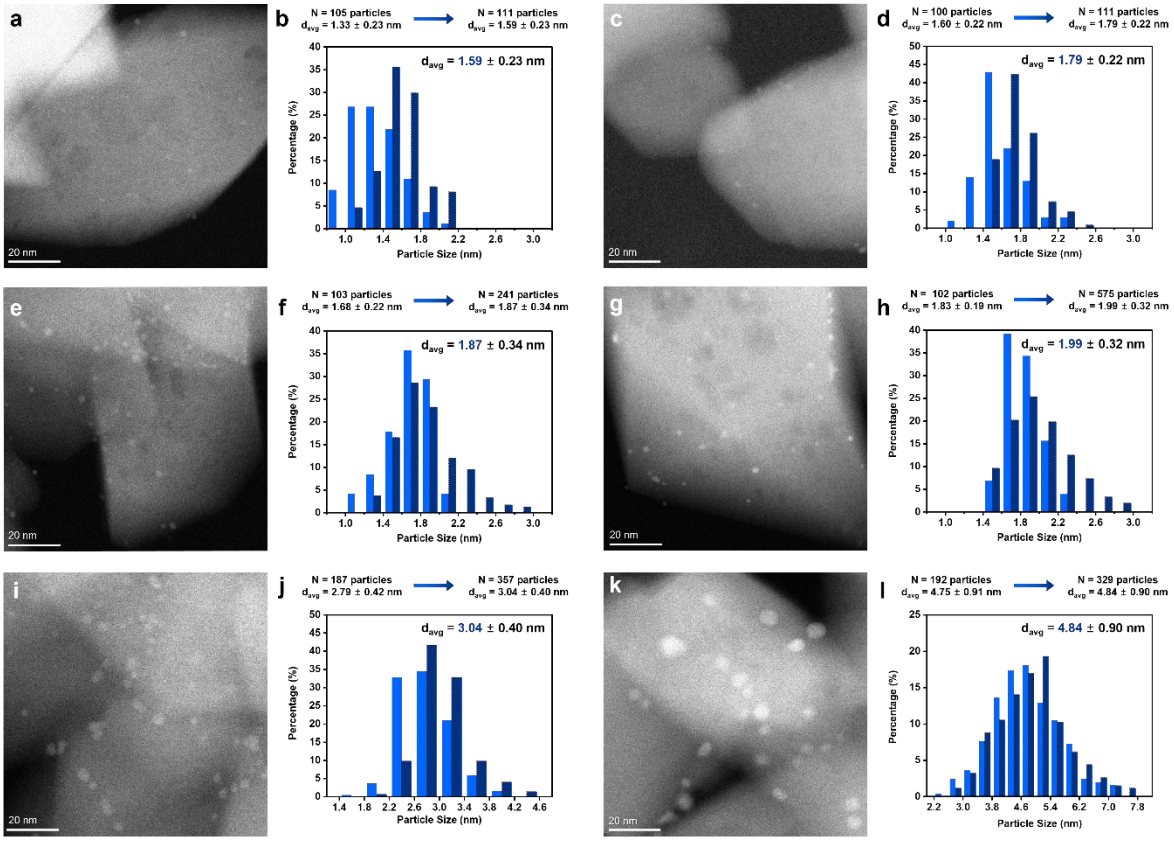

Supplementary Figure 18. Size distributions of Pt/TiO_2(101) catalysts with controlled Pt sizes. HAADF–STEM images and corresponding Pt NP size distributions of the size-controlled Pt/TiO_2(101) catalysts after CO oxidation, with final Pt sizes of (a, b) 1.59 nm, (c, d) 1.79 nm, (e, f) 1.87 nm, (g, h) 1.99 nm, (i–j) 3.04 nm, and (k–l) 4.84 nm. Each set shows the post-reaction STEM image together with the corresponding pre- and post-reaction size distributions. All samples were treated at 240 °C for 2 h under CO/O_2 = 1 to prevent thermal sintering while ensuring that the CO-adsorbate-induced reconstruction process is reflected.

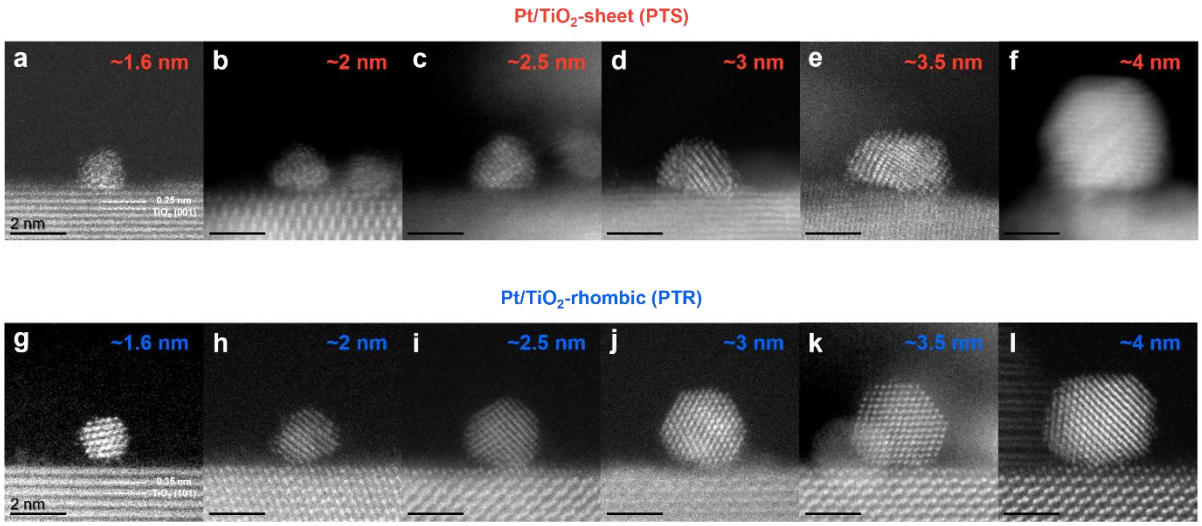

Supplementary Figure 19. Facet-dependent Pt NP morphologies across different NP sizes. High-magnification HAADF–STEM images of size-controlled Pt/TiO_2 catalysts after CO oxidation, with NP sizes ranging from ~1.6 to 4 nm. (a–f) Side-view images showing Pt NPs on the TiO_2(004) plane (PTS), and (g–l) side-view images showing Pt NPs on the TiO_2(101) plane (PTR). Each set demonstrates a size-independent trend in Pt morphology that depends on the exposed TiO_2 facet. All samples were treated at 240 °C for 2 h under CO/O_2 = 1 to prevent thermal sintering while ensuring that the CO-adsorbate-induced reconstruction process is reflected.

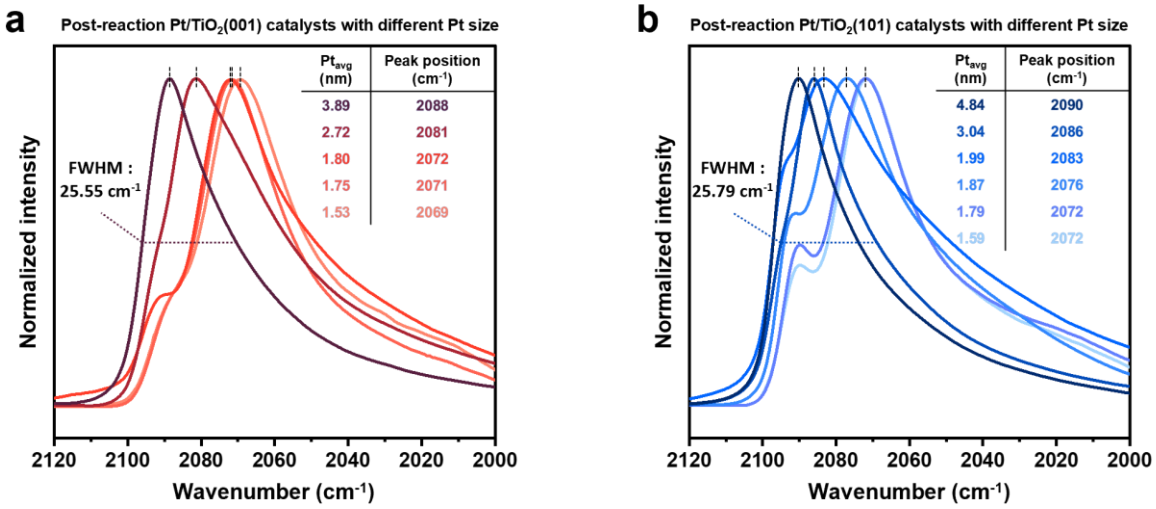

Supplementary Figure 20. CO adsorption characteristics of size-controlled Pt/TiO_2 catalysts. Post-reaction CO-DRIFTS spectra of size-controlled (a) PTS and (b) PTR catalysts with final Pt NP sizes ranging from ~1.5 to ~5 nm. All samples were treated at 240 °C for 2 h under CO/O_2 = 1 to suppress thermal sintering and to ensure that the CO-adsorbate-induced reconstruction process is reflected in the resulting Pt surface structures. The insets indicate the average Pt NP size, corresponding CO adsorption peak positions, and the decrease in FWHM observed for samples with Pt sizes above ~3 nm.

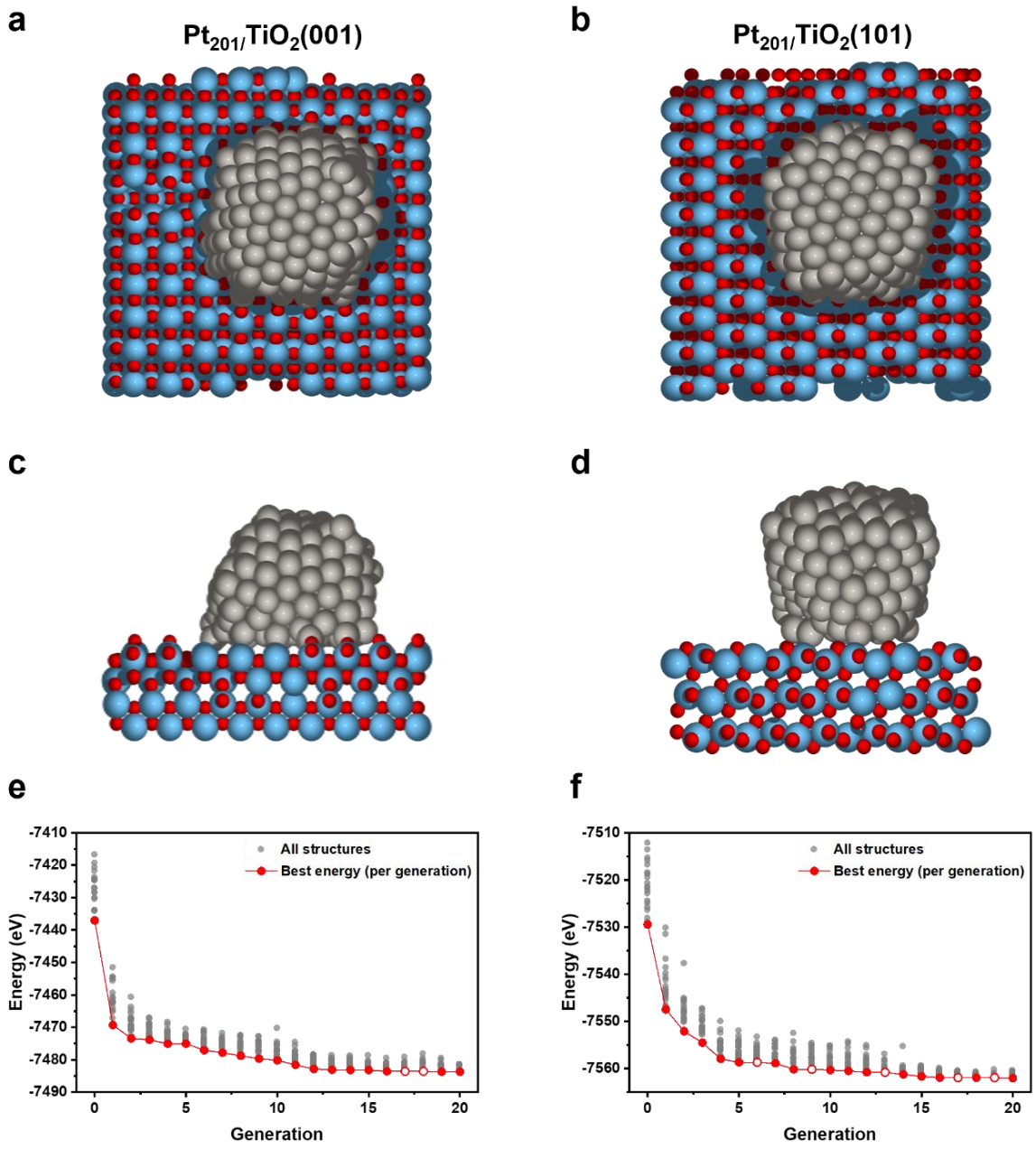

Supplementary Figure 21. Genetic algorithm optimisation of Pt NP structures on TiO_2. Facet-dependent equilibrium morphology of Pt_{201} NPs on TiO_2 obtained by GA optimisation. Top views of the lowest-energy Pt_{201} NP configurations supported on (a) $TiO_2(001)$ and (b) $TiO_2(101)$, and the corresponding side views shown in (c) and (d), illustrating facet-dependent wetting and metal–support contact geometry. The evolution of total energies during the GA optimisation is shown for (e) $Pt_{201}/TiO_2(001)$ and (f) $Pt_{201}/TiO_2(101)$. Grey dots represent the energies of all candidate structures sampled in each generation, while the red line denotes the lowest-energy structure per generation. Filled red circles indicate generations where a new global minimum energy was identified, whereas open red circles indicate generations in which the global minimum remained unchanged.

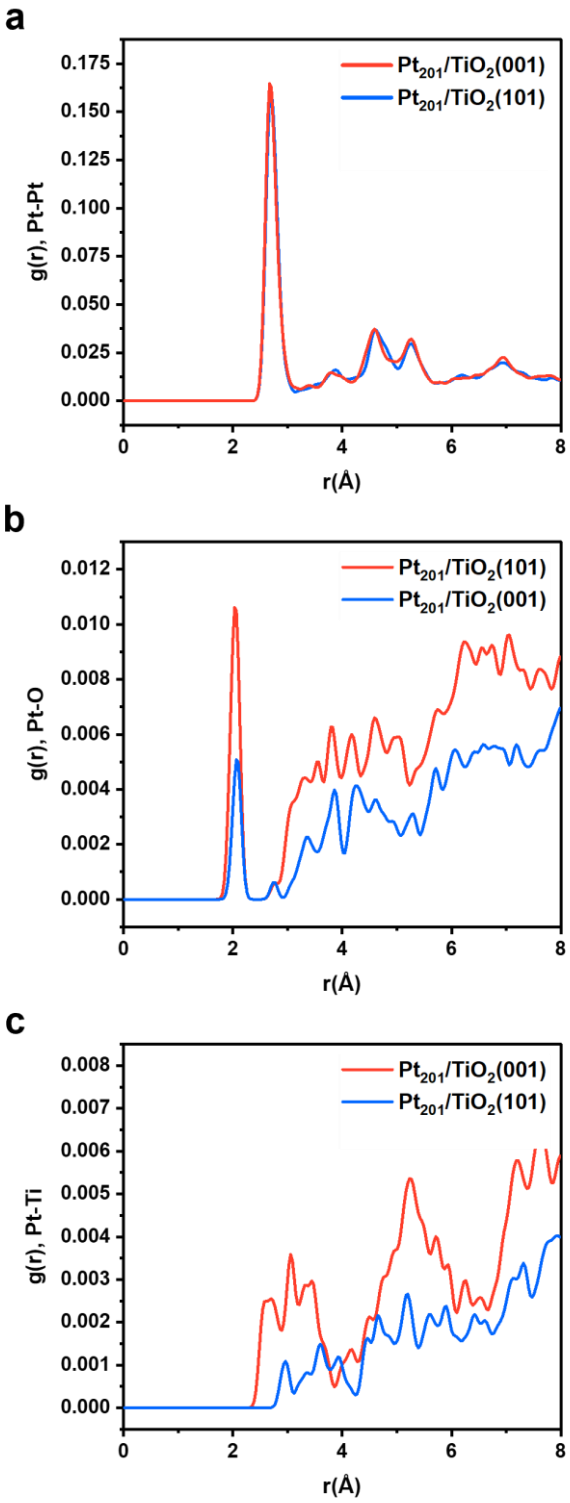

Supplementary Figure 22. Facet-dependent local atomic environments of Pt NPs. Radial distribution functions $g(r)$ for (a) Pt–Pt, (b) Pt–O, and (c) Pt–Ti atomic species obtained from genetic algorithm optimisation of Pt_{201}/TiO_2 species. Red: $Pt_{201}/TiO_2(001)$ and Blue: $Pt_{201}/TiO_2(101)$.

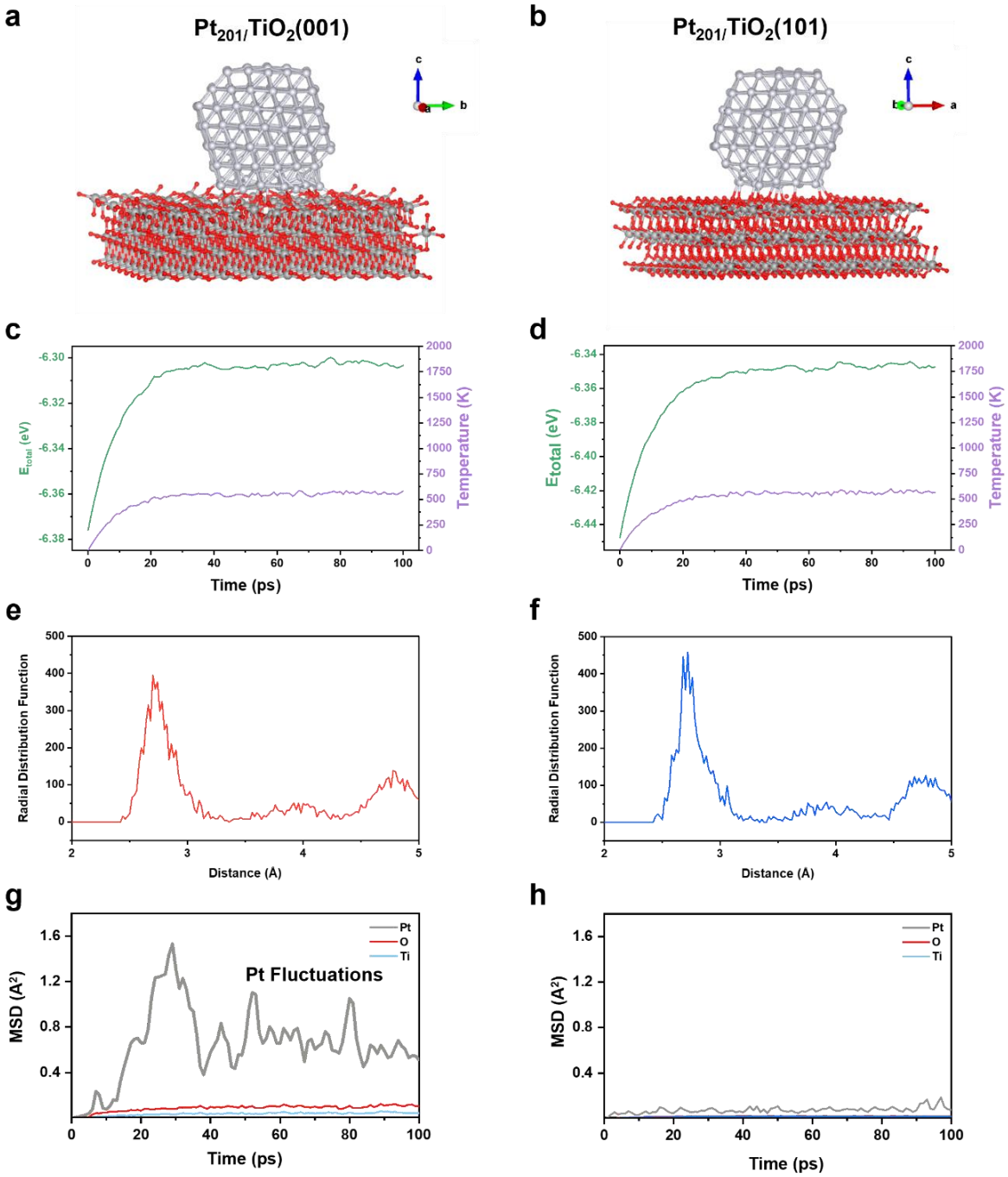

Supplementary Figure 23. Thermally induced structural evolution of Pt NPs on TiO_2 facets. Thermal convergence and facet-dependent structural evolution of Pt_{201} NPs on TiO_2 revealed by GNN–MD simulations under mild conditions. (a, b) Final snapshots after simulations at 573 K for 100 ps for (a) $Pt_{201}/TiO_2(001)$ and (b) $Pt_{201}/TiO_2(101)$. (c, d) Time evolution of total energy and temperature for (c) $Pt_{201}/TiO_2(001)$ and (d) $Pt_{201}/TiO_2(101)$, demonstrating thermal convergence. (e, f) Pt–Pt radial distribution functions (RDFs) for (e) $Pt_{201}/TiO_2(001)$ and (f) $Pt_{201}/TiO_2(101)$. (g, h) Mean square displacement (MSD) of each atom as a function of simulation time for (g) $Pt_{201}/TiO_2(001)$ and (h) $Pt_{201}/TiO_2(101)$.

Supplementary Table 3. Quantitative structural descriptors extracted from GNN–MD simulations after 0.8 ns at 1500 K for Pt_{201} NPs supported on different TiO_2 facets.

	ΔPt–Ti bonds	ΔO average z (Å)	ΔPt–O separation (Å)	ΔPt height (Å)
Pt/anatase TiO_2(001)	+11	+0.23	−2.22	+0.39
Pt/anatase TiO_2(101)	−1	+0.07	+0.05	+1.73

Reported values correspond to changes (Δ) relative to the corresponding initial configurations prior to MD simulations. Specifically, changes in number of Pt–Ti bonds (ΔPt–Ti bonds), the changes in the average vertical displacement of surface oxygen atoms (ΔO average z (Å)), the changes in the mean Pt–O separation (ΔPt–O separation (Å)), and the changes in the overall height of the Pt NP with respect to the initial structure (ΔPt height (Å))

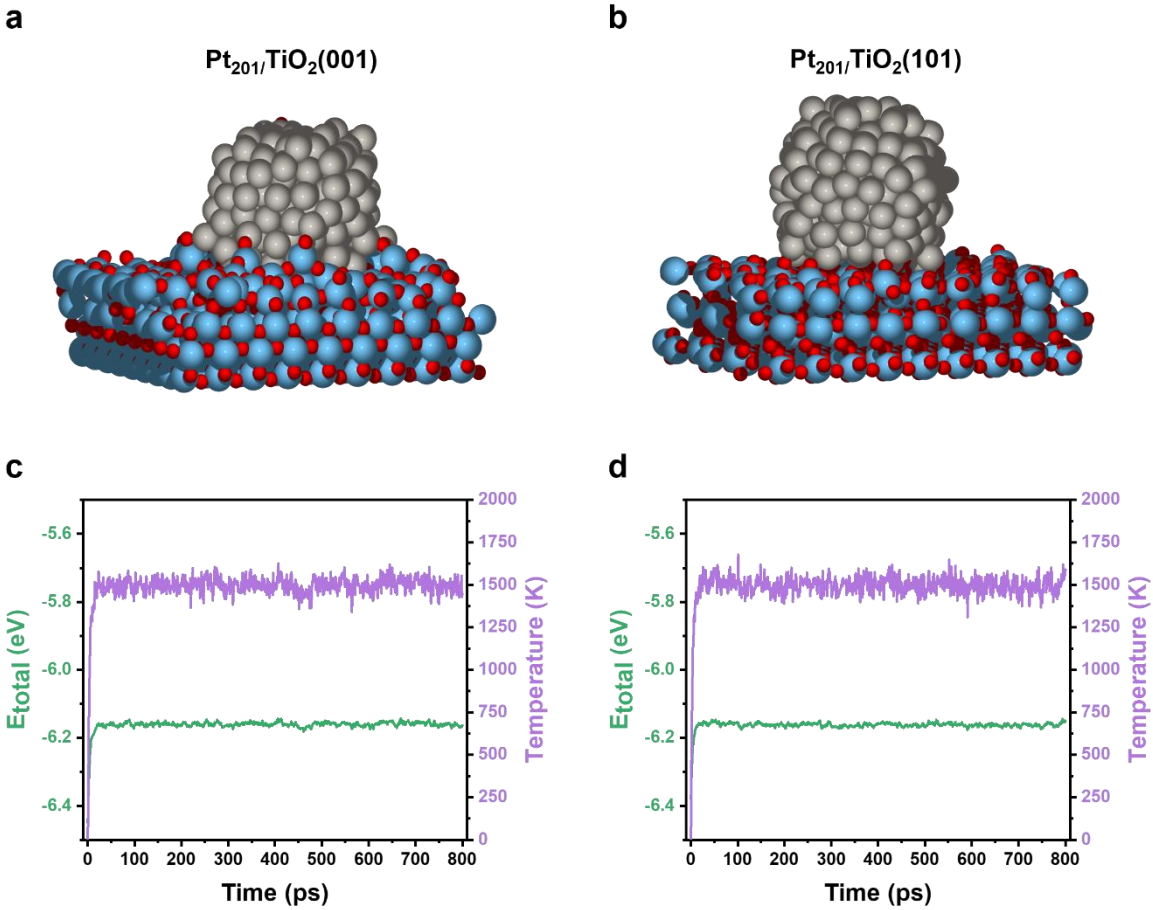

Supplementary Figure 24. Structural evolution of Pt NPs under extreme thermal conditions. Thermal convergence and facet-dependent structural evolution of Pt_{201} NPs on TiO_2 revealed by GNN–MD simulations under extreme conditions. Final snapshots after the simulations at 1500 K for 0.8 ns for (a) $Pt_{201}/TiO_2(001)$ and (b) $Pt_{201}/TiO_2(101)$, with time evolution of total energy and temperature confirming stable thermal equilibration during simulations for (c) $Pt_{201}/TiO_2(001)$ and (d) $Pt_{201}/TiO_2(101)$.

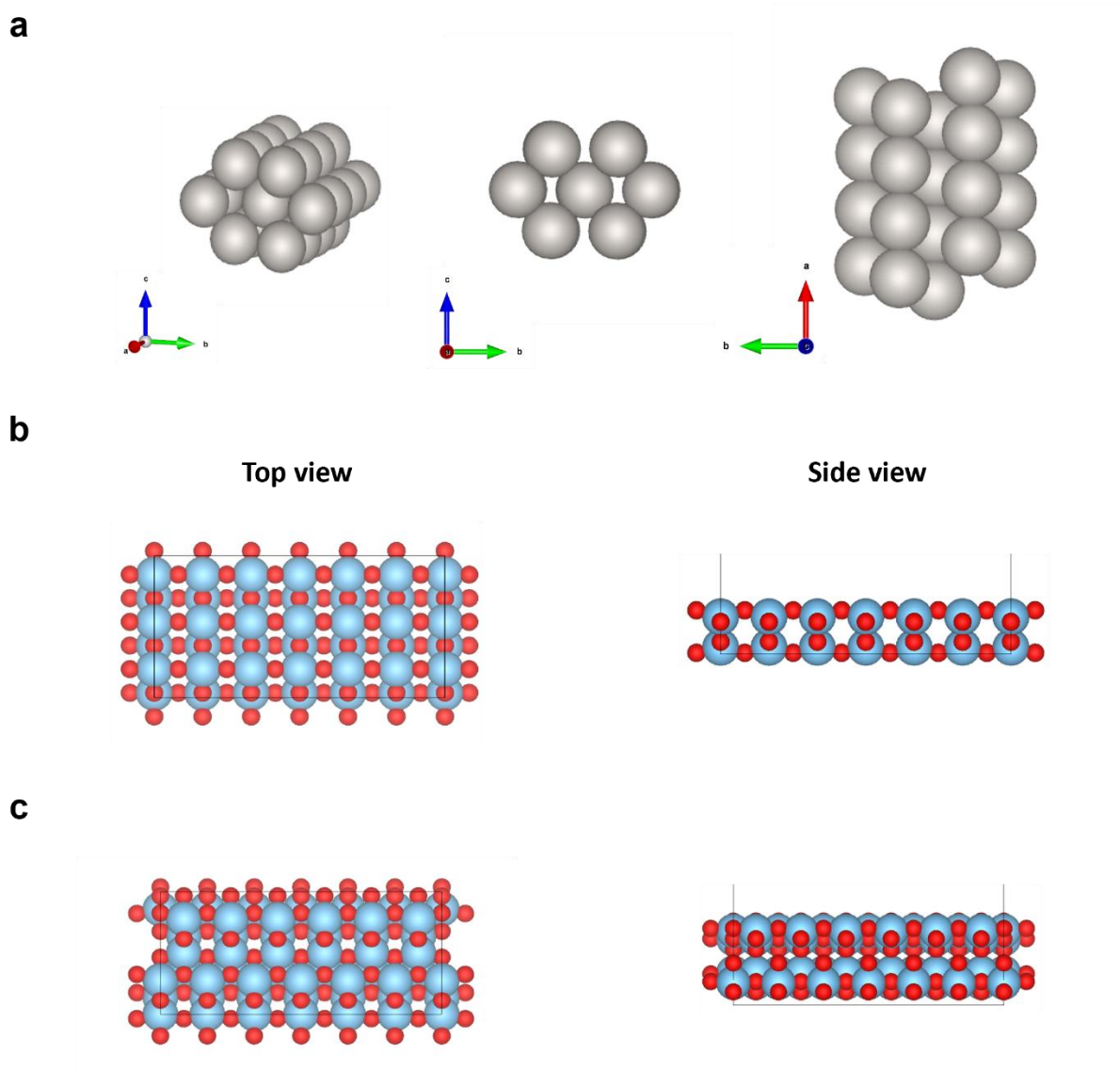

Supplementary Figure 25. Initial structural models for DFT calculations. Initial structural models used for DFT calculations: (a) rod-shaped Pt_{28} cluster, (b) TiO_2 sheet exposing the (001) facet, and (c) TiO_2 rhombic crystal exposing the (101) facet. Multiple viewing angles are shown to illustrate the atomic arrangement and surface orientations of each model.

Supplementary Table 4. Average Pt–Pt coordination number (CN) and corresponding bond distance (Å) with standard deviations in the DFT-optimised Pt_{28} rod models supported on TiO_2(001) and (101) facets.

	Pt/TiO_2(001) (PTS)	Pt/TiO_2(101) PTR
Average Pt–Pt coordination number	4.79	5.00
Average Pt–Pt distance [Å]	5.55	5.31
Standard deviation of Pt–Pt distances [Å]	2.23	2.01

Supplementary Table 5. Surface energies of TiO_2(001) and (101) facets and the corresponding normalised Pt binding energies (per Pt atom) in the DFT-optimised Pt_{28} rod on TiO_2 models.

	$Pt_{28}/TiO_2(001)$	$Pt_{28}/TiO_2(101)$
Surface energy of TiO_2 surface [$eV \cdot Å^{-2}$]	0.084	0.067
Normalized Pt binding E [$eV \cdot atom^{-1}$]	−0.78	−0.68
Normalized Adhesion E [$eV \cdot atom^{-1}$]	−0.86	−0.80
Interfacial area of Pt–TiO_2 [$Å^2$]	103.2	70.4
Surface area normalised Adhesion E [$eV \cdot Å^{-2}$]	−0.233	−0.316

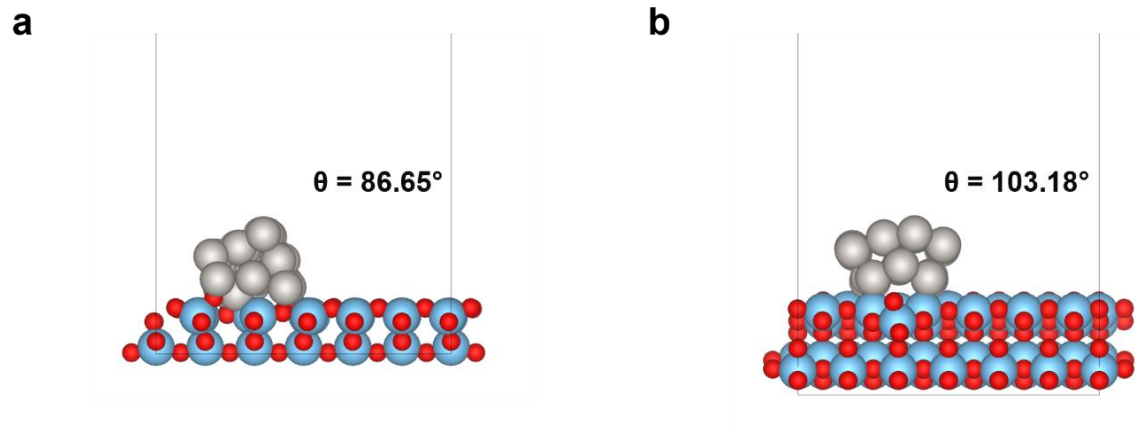

Supplementary Figure 26. DFT-optimised Pt_{28}/TiO_2 models. Side-view representations of DFT-optimised models of (a) Pt_{28} rod on $TiO_2(001)$ facet and (b) Pt_{28} rod on $TiO_2(101)$ facet.

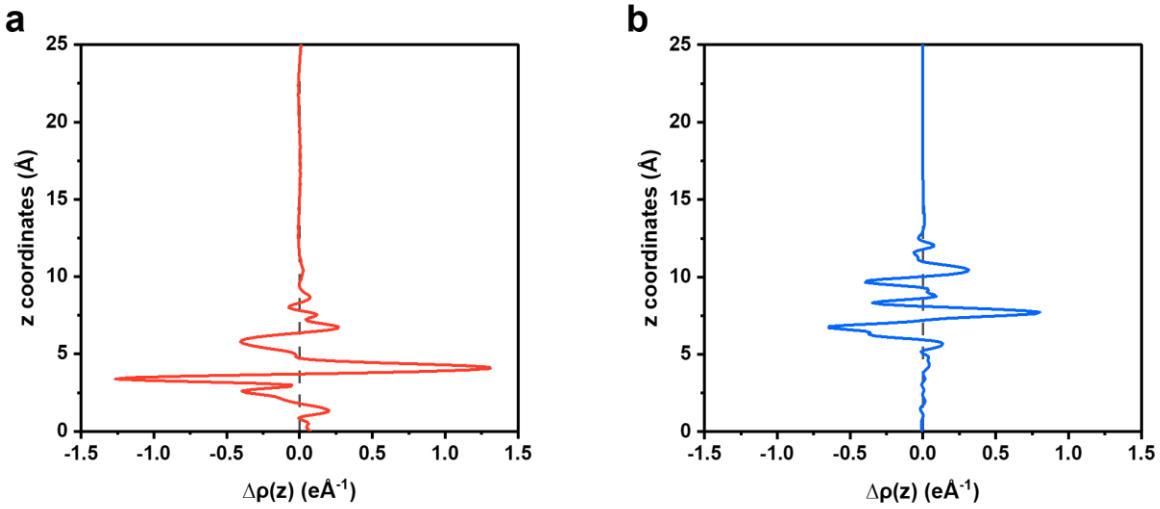

Supplementary Figure 27. Charge density distributions across Pt/TiO_2 interfaces. One-dimensional planar-averaged charge density along the z-direction for (a) $Pt_{28}/TiO_2(001)$ and (b) $Pt_{28}/TiO_2(101)$.

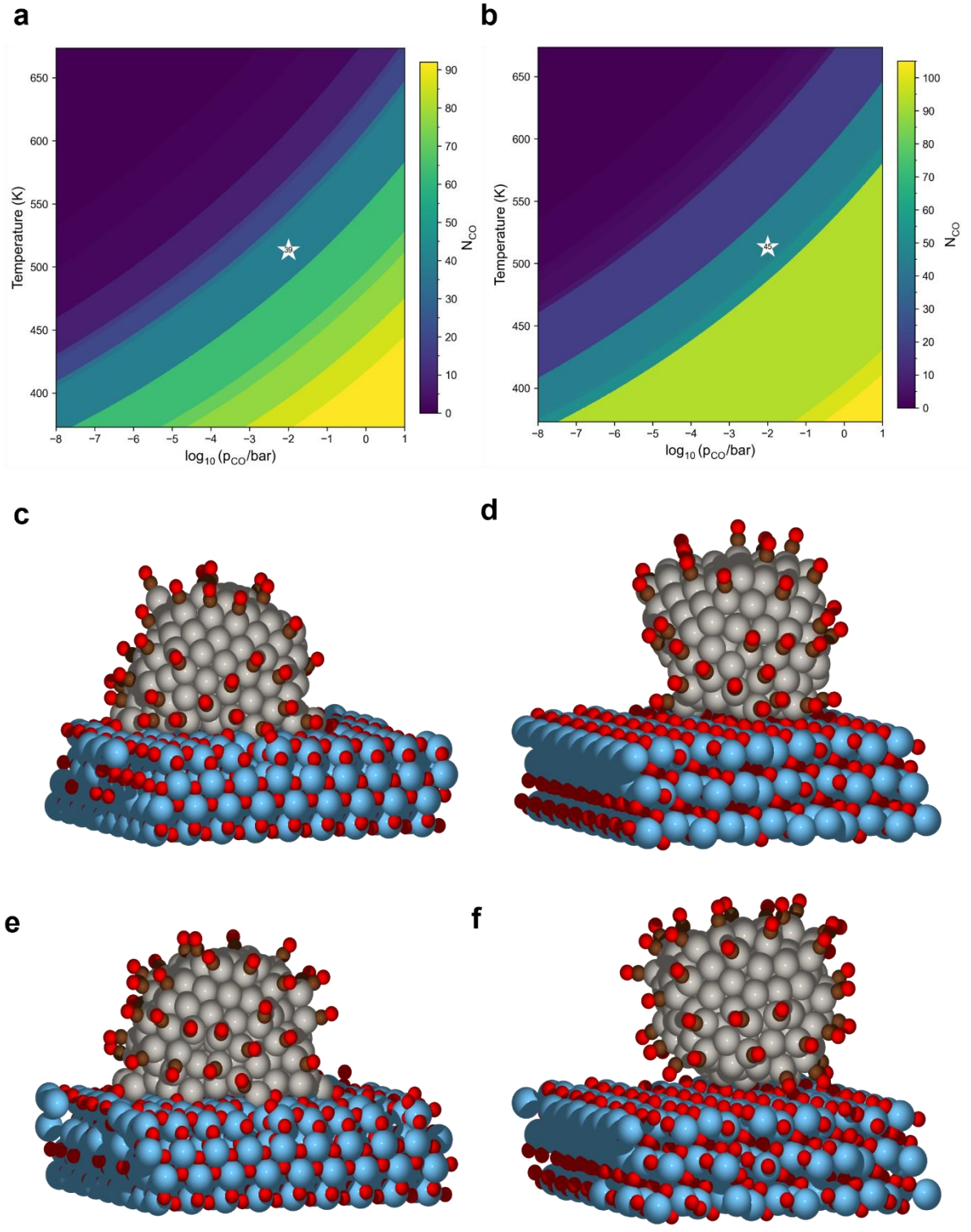

Supplementary Figure 28. CO-induced reconstruction of Pt NPs on TiO_2 facets. Grand-canonical surface phase diagram of CO coverage and CO-induced reconstruction of Pt_{201} NPs on TiO_2 facets. (a, b) Stable CO coverage as a function of temperature and CO partial pressure on (a) TiO_2(001) and (b) TiO_2(101). (c, d) Initial configurations with CO adsorbed at available Pt top sites on (c) TiO_2(001) and (d) TiO_2 (101). (e, f) Corresponding structures after GNN–MD simulations at 513 K for 100 ps under CO-rich conditions on (e) TiO_2(001) and (f) TiO_2(101).

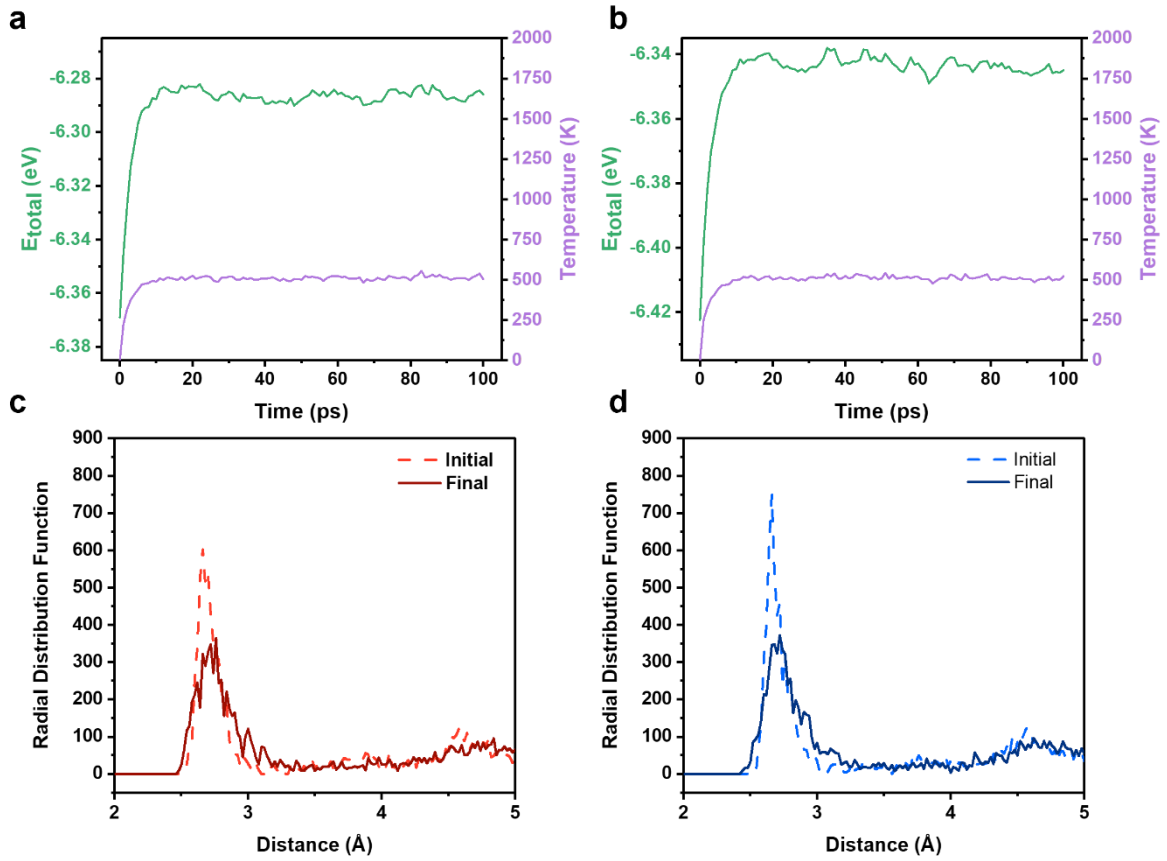

Supplementary Figure 29. Structural evolution of CO-covered Pt NPs during GNN-MD simulations. Thermal convergence and CO-induced structural evolution of Pt_{201} NPs on TiO_2 facets revealed by GNN–MD simulations. Time evolution of total energy and temperature for (a) $Pt_{201}/TiO_2(001)$ and (b) $Pt_{201}/TiO_2(101)$ during GNN–MD simulations at 513 K, confirming thermal equilibration under CO-rich conditions. Radial distribution functions of Pt atoms before and after simulation are shown for (c) $Pt_{201}/TiO_2(001)$ and (d) $Pt_{201}/TiO_2(101)$.

Supplementary Table 6. Pt–Pt coordination number statistics for CO-covered Pt_{201} NPs before and after GNN–MD simulations at 513 K, 100 ps.

System	Mean CN	Std. dev.
Initial $Pt_{201}/TiO_2(001)$	7.48	0.97
Final $Pt_{201}/TiO_2(001)$	7.40	1.07
Initial $Pt_{201}/TiO_2(101)$	7.54	0.98
Final $Pt_{201}/TiO_2(101)$	7.42	1.17

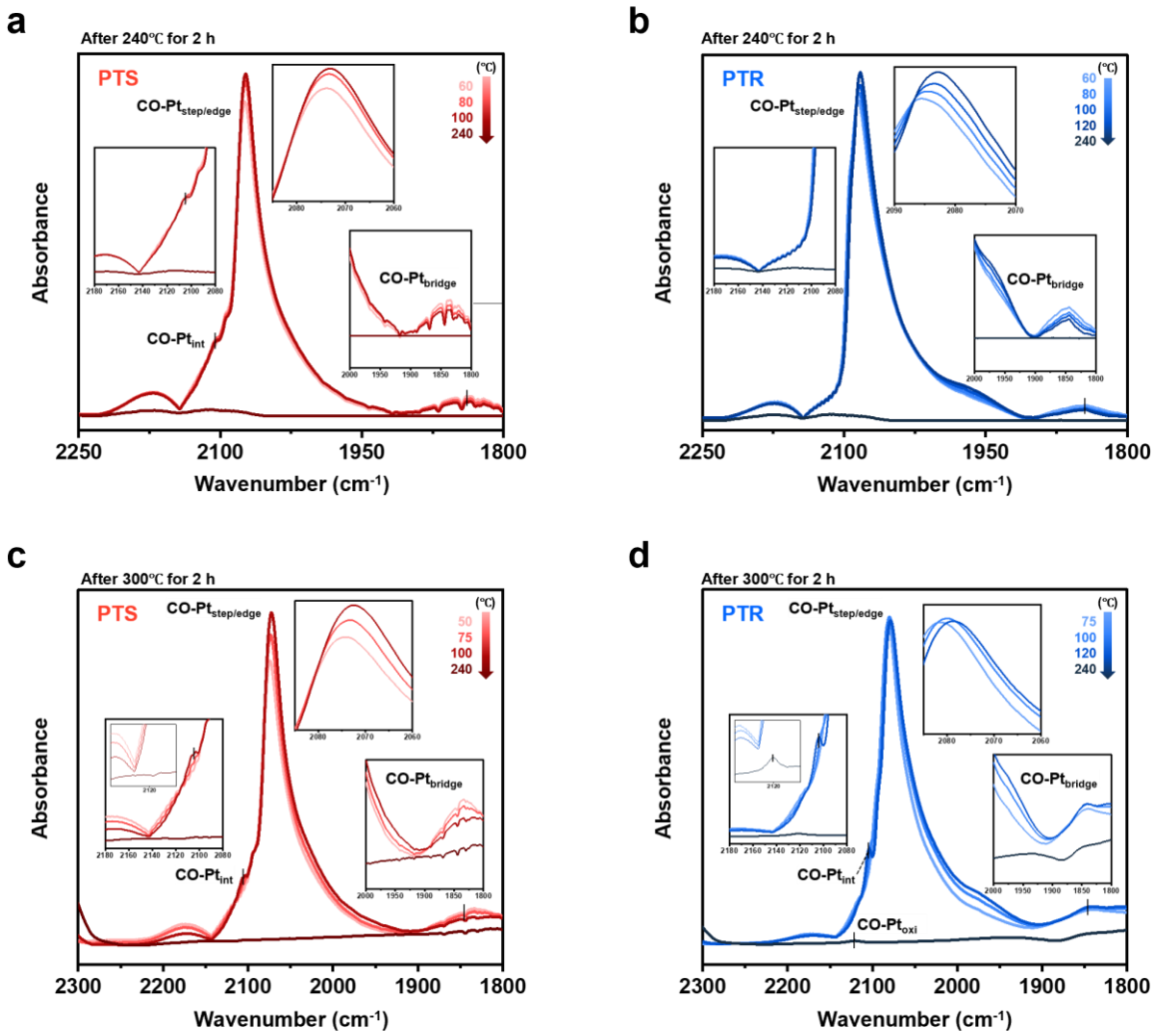

Supplementary Figure 30. Facet-dependent evolution of CO adsorption after Pt reconstruction. *In situ* DRIFT spectra of (a, c) spent PTS and (b, d) spent PTR catalysts under CO oxidation condition ($CO/O_2 = 1$) at increasing temperatures. Spent catalysts were prepared by treating the samples at (a, b) 240 °C for 2 h and (c, d) 300 °C for 2 h. Characteristic bands corresponding to CO adsorbed on Pt_{int} sites, along with surface roughening features, highlight facet-dependent CO-induced Pt restructuring. Note that the spectrum in (d) was obtained using a spent PTR catalyst in which thermally induced sintering was observed (Supplementary Fig. 15). Additionally, a peak at ~2120 cm^{-1} observed in the inset of (d) appears after ignition and is assigned to CO adsorbed on oxidized Pt sites (Pt_{oxi}), which may hinder catalytic activity due to stronger CO binding.[1, 2]

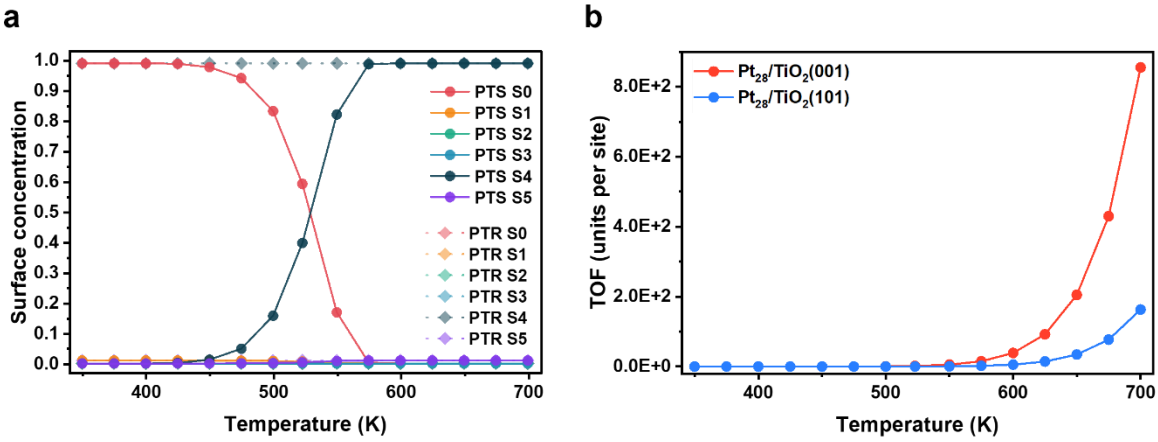

Supplementary Figure 31. Microkinetic analysis of CO oxidation on Pt/TiO_2 catalysts. Microkinetic modeling results for CO oxidation on Pt_{28}/TiO_2 catalysts. (a) Temperature-dependent surface coverages of reaction intermediates predicted for Pt_{28}/TiO_2(001) (PTS) and Pt_{28}/TiO_2(101) (PTR). (b) Corresponding CO_2 turnover frequencies (TOFs), highlighting the markedly enhanced activity of Pt_{28}/TiO_2(001) at elevated temperatures.

Supplementary Table 7. Comparison of per-site CO oxidation TOF ($s^{-1}\cdot site^{-1}$) at WHSV = 1.5×10^5 $mL\cdot g_{cat}^{-1}\cdot h^{-1}$, 1% CO, 1% O_2/Ar, 1 atm from the MvK microkinetic model and the experimentally measured rates, for PTS and PTR.

T (°C)	TOF_{exp}, PTS	TOF_{calc},PTS (MvK)	TOF_{exp}, PTR	TOF_{calc},PTR (MvK)
170	0.024	0.018	–	9.1×10^{-6}
180	0.075	0.034	–	4.0×10^{-5}
190	0.111	0.062	–	1.3×10^{-4}
200	0.148	0.115	–	4.4×10^{-4}
210	0.220	0.201	–	1.3×10^{-3}
220	0.372	0.347	0.036	3.8×10^{-3}
230	–	0.591	0.066	0.011
240	–	0.972	0.135	0.027
250	–	1.60	0.275	0.070

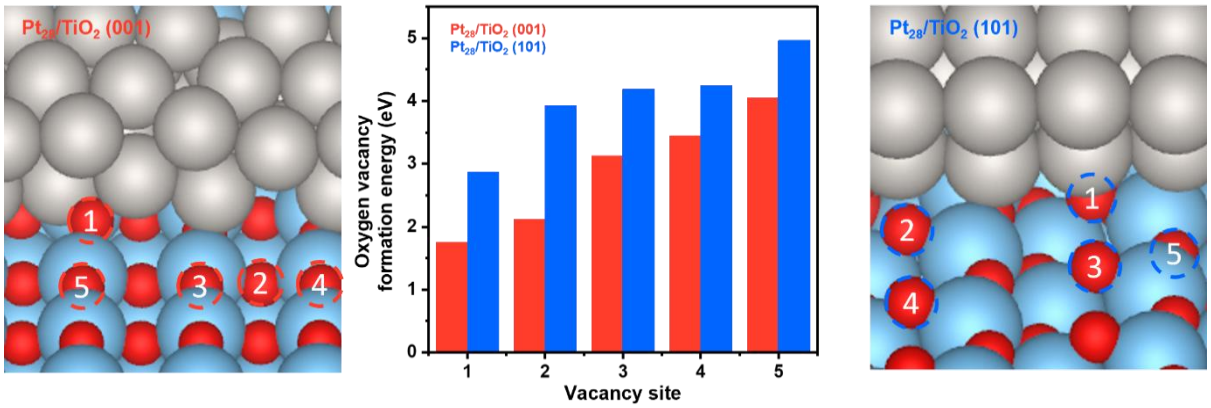

Supplementary Figure 32. Facet-dependent oxygen vacancy formation at Pt–TiO_2 interfaces. Possible oxygen vacancy formation sites at the Pt–TiO_2 interface for both (001) and (101) surfaces in the Pt_{28}/TiO_2 models, along with the corresponding calculated formation energies for each site. Pt_{28}/TiO_2(001) shows systematically lower vacancy formation energies (by ~0.3-0.6 eV) than Pt_{28}/TiO_2(101) across multiple surface sites.

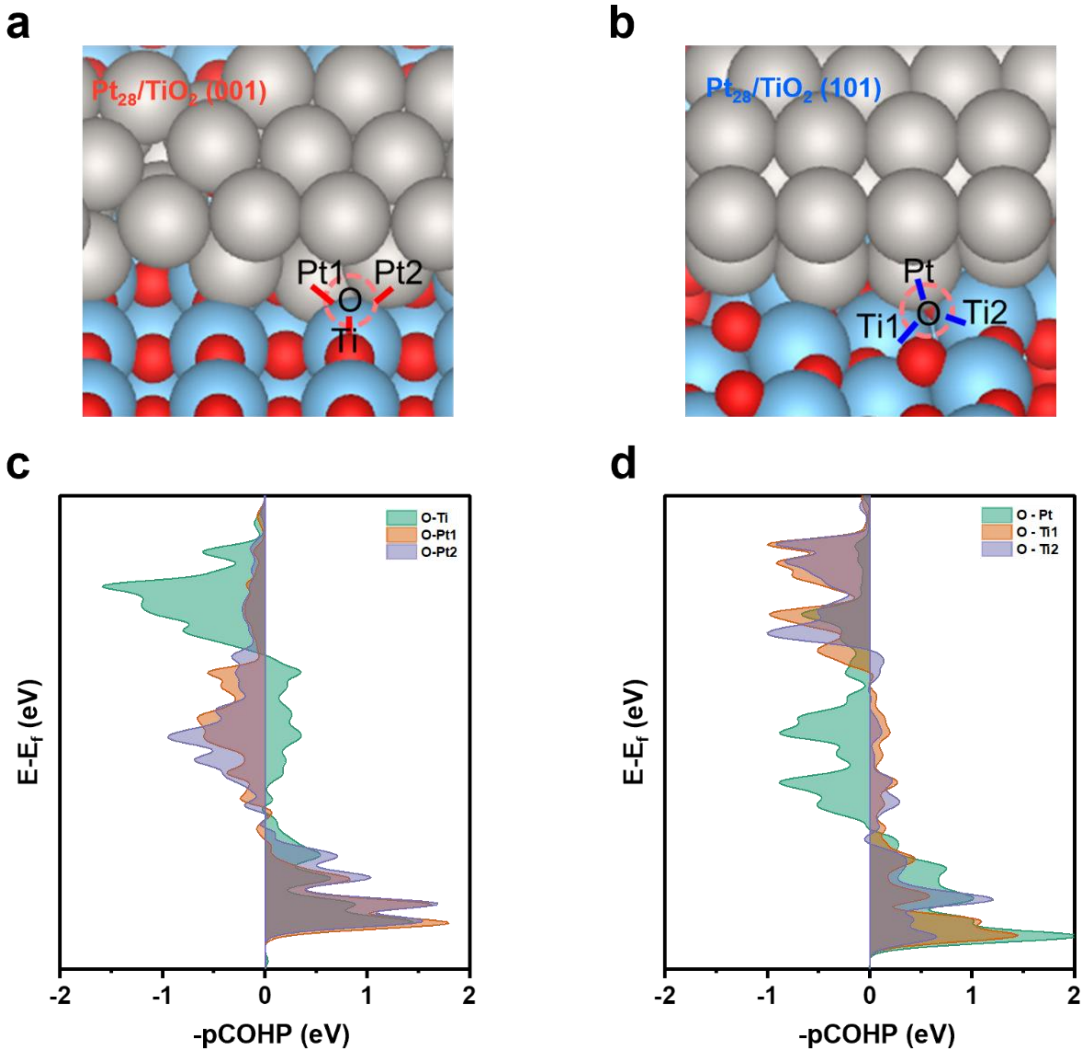

Supplementary Figure 33. Electronic interactions governing oxygen vacancy formation at Pt–TiO_2 interfaces. The active oxygen vacancy site and its neighboring bonds for (a) $Pt_{28}/TiO_2(001)$ and (b) $Pt_{28}/TiO_2(101)$, along with the corresponding −pCOHP analysis results for oxygen vacancy formation at the Pt–TiO_2 interface: (c) $Pt_{28}/TiO_2(001)$ and (d) $Pt_{28}/TiO_2(101)$. Colored curves indicate the −pCOHP for individual bonds between the selected oxygen vacancy site and its neighboring Pt/Ti atoms, as shown in (a) and (b).

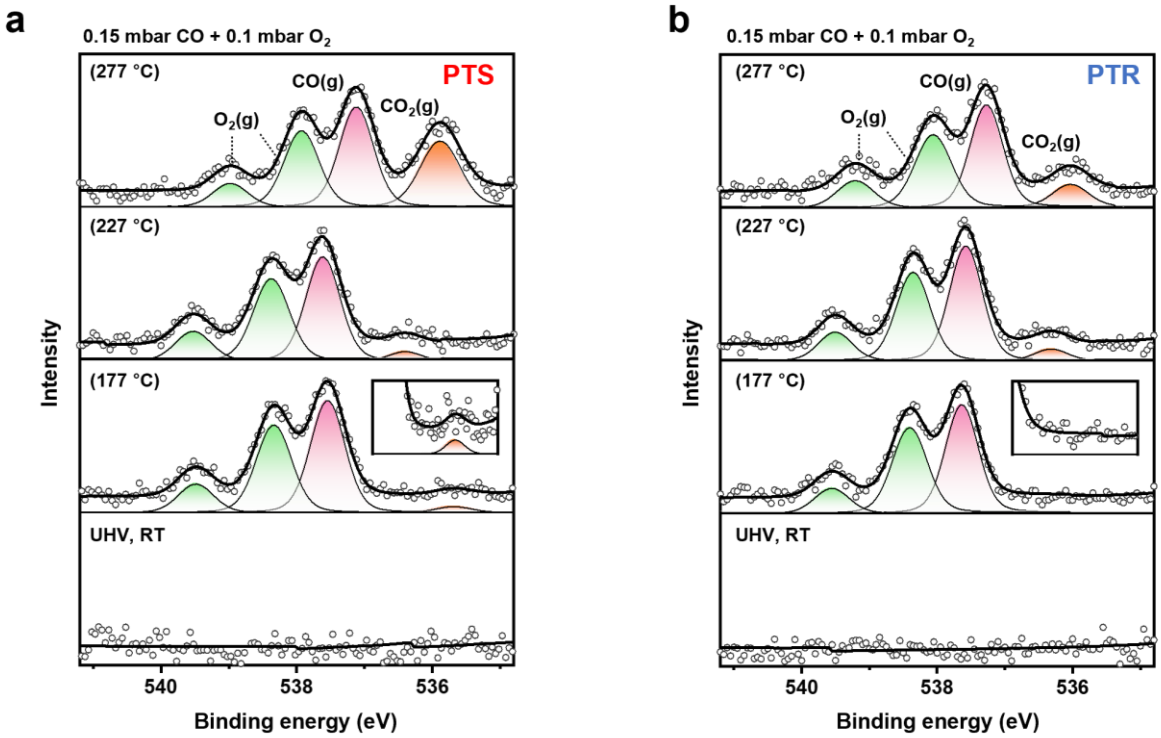

Supplementary Figure 34. Gas-phase O 1*s* NAP-XPS spectra under CO oxidation conditions. Enlarged view of the gas-phase region in the O *1s* NAP-XPS spectra ($h\nu$ = 640 eV) for (a) PTS and (b) PTR under UHV and CO oxidation conditions (0.15 mbar of CO and 0.1 mbar of O_2) at various temperatures (RT, 177, 227, and 277 °C).

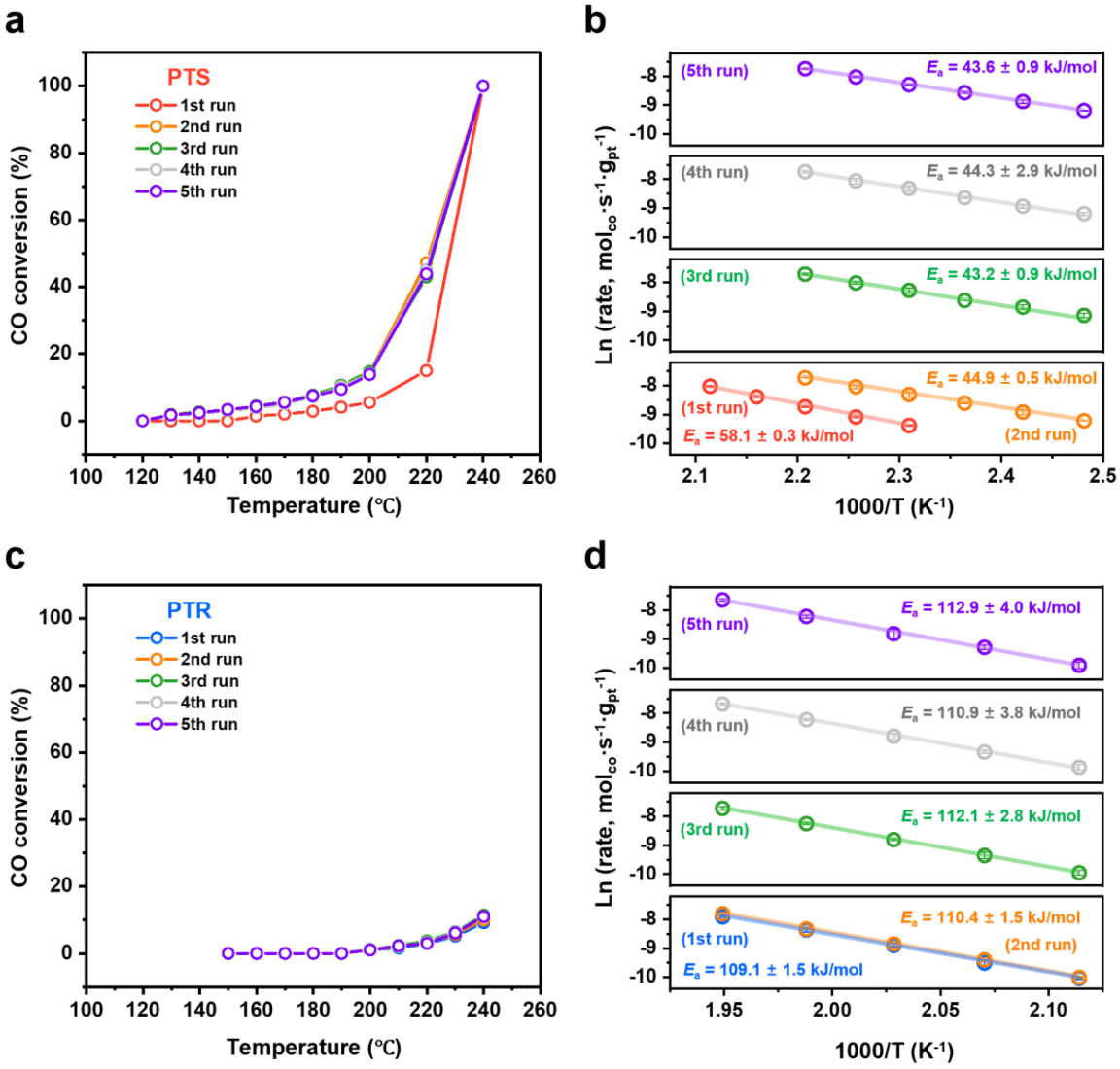

Supplementary Figure 35. Catalytic evolution during repeated CO oxidation cycles. Temperature-dependent catalytic cycle tests and corresponding apparent activation energies (E_a) for (a, b) PTS and (c, d) PTR. Five consecutive catalytic runs were performed for each catalyst in a single experiment over the temperature range up to 240 °C, where complete catalytic ignition was observed in the DRIFTS results. After the 1st run, the catalyst was held at 240 °C for 2 h before the 2nd run. All E_a values were obtained at a total flow rate of 100 mL·min^{-1} with a CO/O_2 ratio of 1 under the kinetically relevant regime (<10% CO conversion), and were averaged over three independent experiments using newly loaded catalysts to ensure reproducibility, with error bars representing the standard deviation.

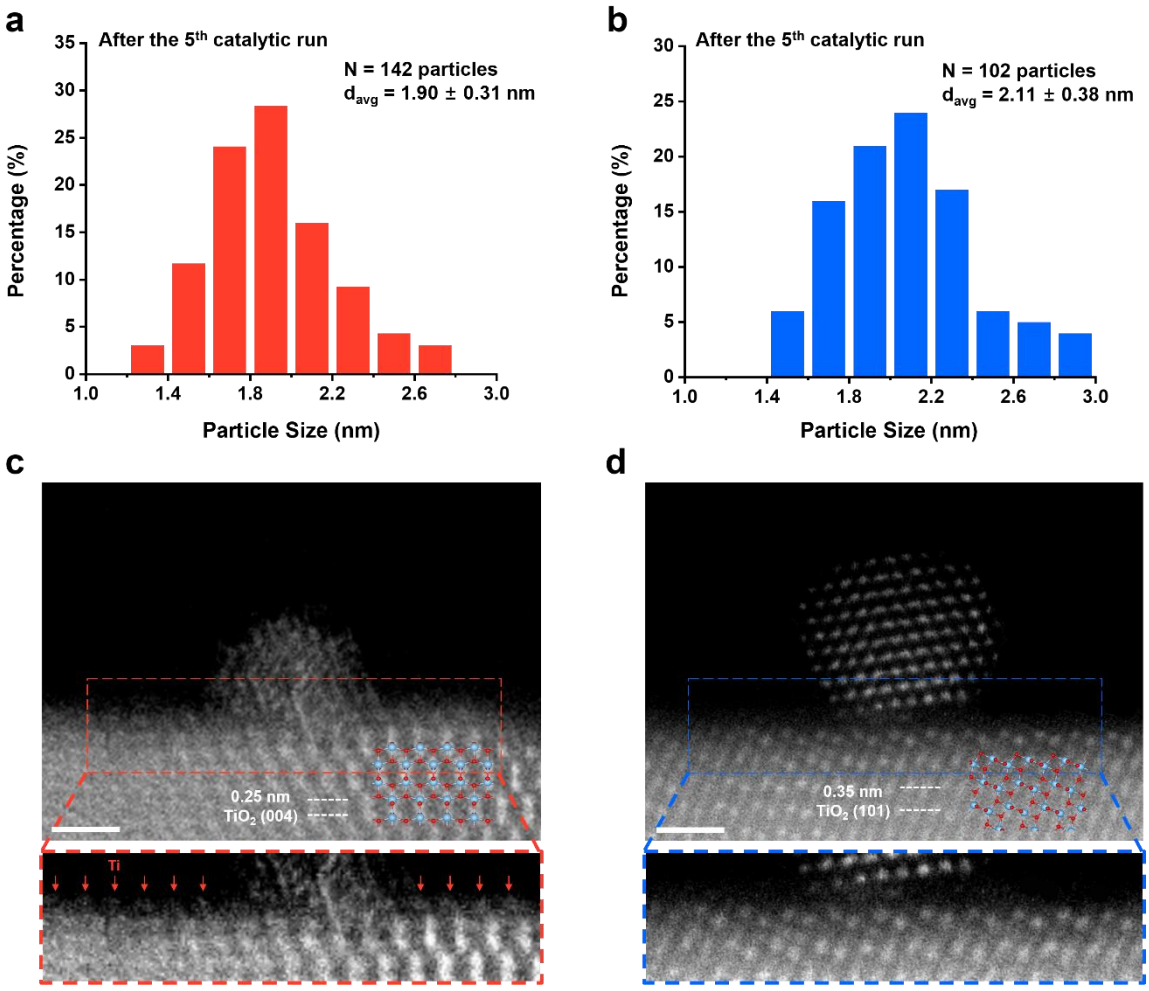

Supplementary Figure 36. Structural stability of Pt/TiO_2 catalysts after repeated catalytic cycles. (a, b) Histograms showing the Pt NP size distributions and (c, d) HAADF-STEM images of the spent catalysts after the 5th catalytic run for (a, c) PTS and (b, d) PTR. The HAADF-STEM images and corresponding atomic models show that both supports retain anatase TiO_2 lattice structures with predominantly exposed (001) and (101) facets, respectively. (Scale bars, 1 nm) The dashed rectangular regions further indicate that no clear TiO_2 surface reconstruction is observed near the Pt–TiO_2 interface under the present conditions.

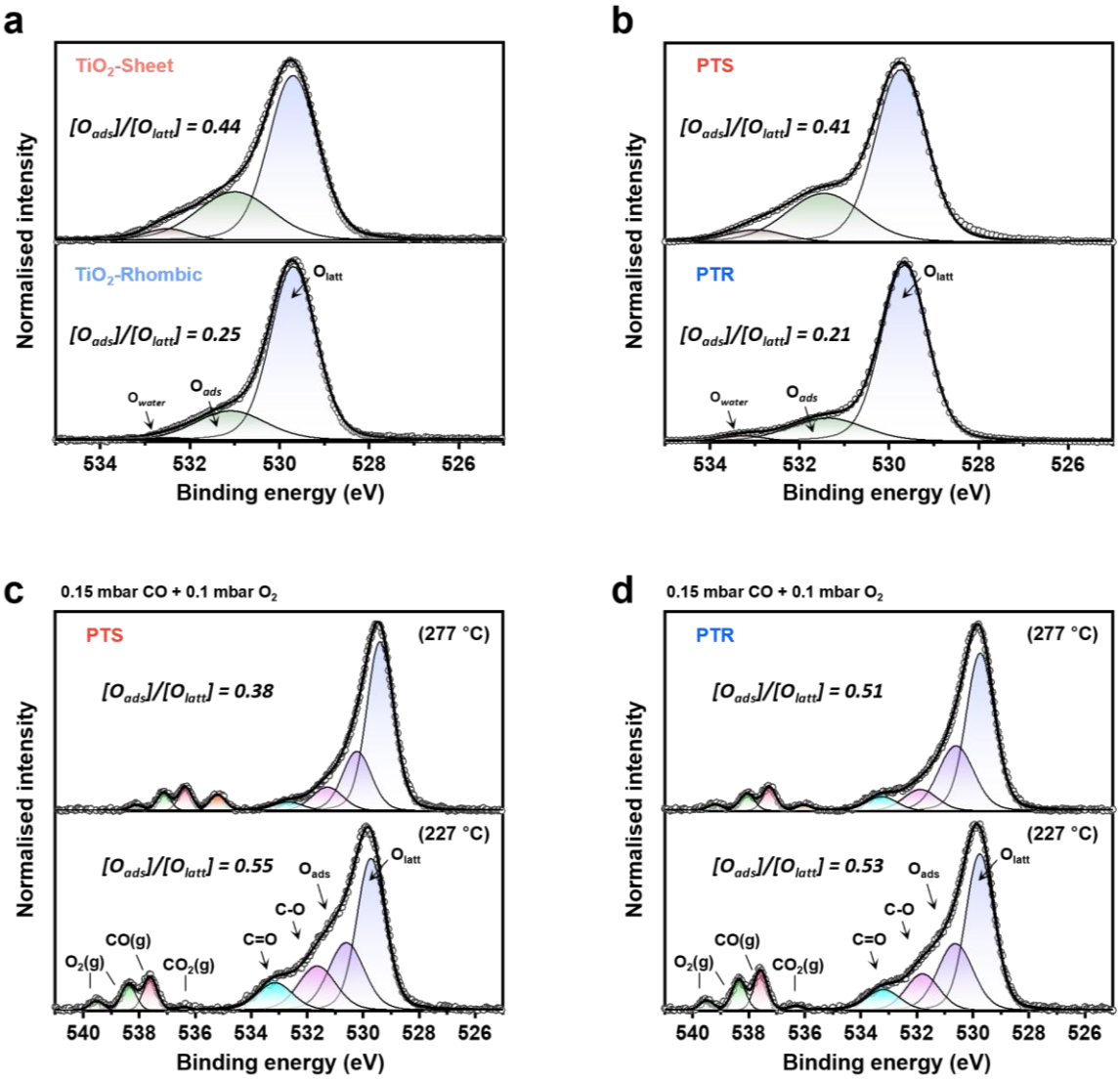

Supplementary Figure 37. O 1*s* XPS analysis of surface oxygen species under UHV and CO oxidation conditions. Normalised O 1*s* XPS spectra of (a) pristine TiO_2 and (b) Pt/TiO_2 catalysts measured under UHV conditions, and of (c) PTS and (d) PTR catalysts measured under CO oxidation conditions (0.15 mbar CO and 0.1 mbar O_2) at 227 and 277 °C.

a

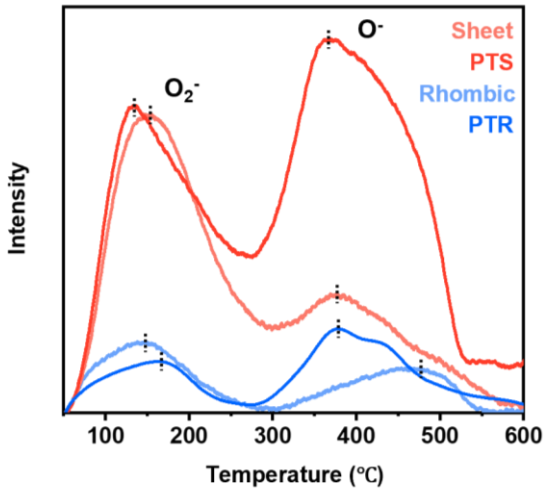

b

Catalysts	$O_{50\text{-}600\ °C}$ (μmol·m^{-2})
TiO_2 sheet (001), (TiO_2-S)	1.70
TiO_2 rhombic (101), (TiO_2-R)	2.06
PTS	3.13
PTR	2.85

Supplementary Figure 38. Facet-dependent oxygen activation and storage capacity of Pt/TiO_2 catalysts. (a) O_2-TPD profiles of pristine TiO_2 and Pt/TiO_2 catalysts, showing distinct desorption features attributed to superoxide (O_2^-, 100–300 °C) and peroxide (O^-, 300–600 °C) species. (b) Corresponding oxygen storage capacity values integrated from 50 to 600 °C and normalised by the specific surface area, highlighting enhanced oxygen mobility and activation upon Pt loading, particularly on the TiO_2(001) facet.

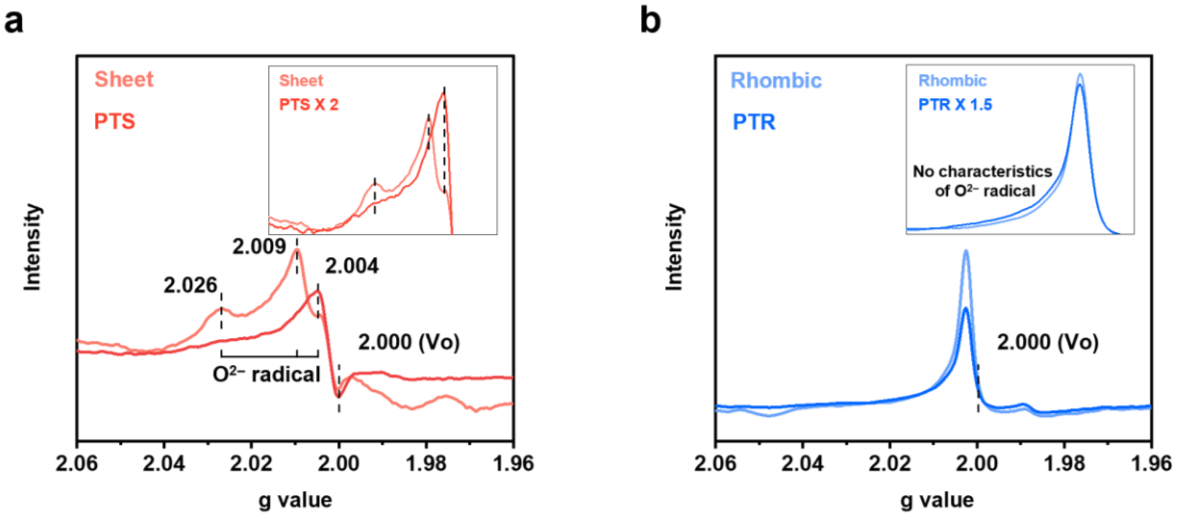

Supplementary Figure 39. Facet-dependent oxygen defect characteristics revealed by EPR spectroscopy. EPR spectra of (a) pristine TiO_2 sheet with predominantly exposed (001) the corresponding Pt-loaded catalyst (PTS), and (b) pristine TiO_2 rhombic with exposed (101) facets and the corresponding Pt-loaded catalyst (PTR). The inset figures in both panels highlight that the EPR signals exhibit facet-dependent characteristics of TiO_2 upon Pt loading.

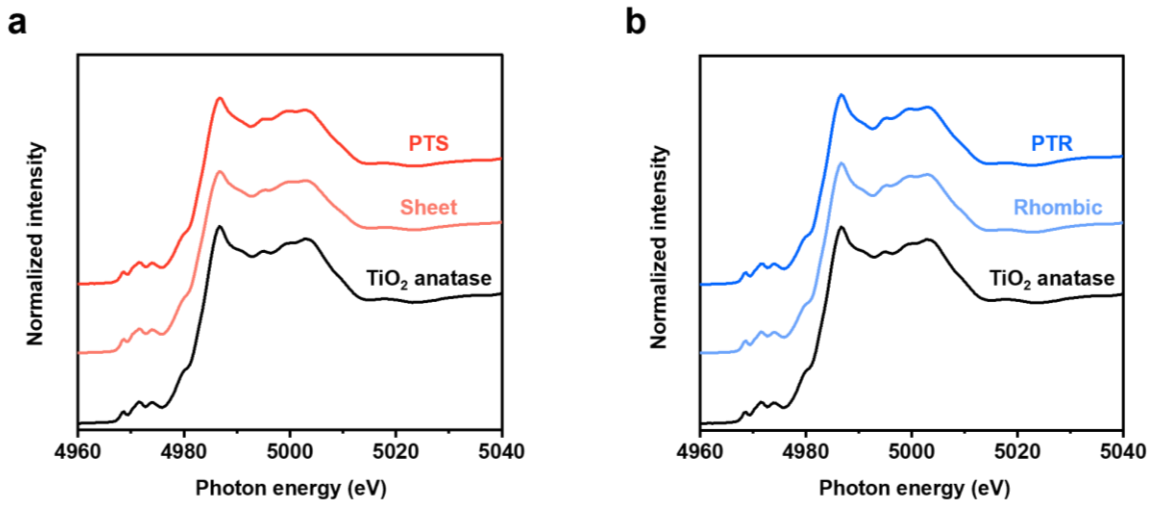

Supplementary Figure 40. Ti *K*-edge XANES spectra of Pt/TiO_2 catalysts. Ti *K*-edge XANES spectra of (a) pristine TiO_2 sheet and Pt-loaded PTS catalyst and (b) pristine TiO_2 rhombic and Pt-loaded PTR catalyst.

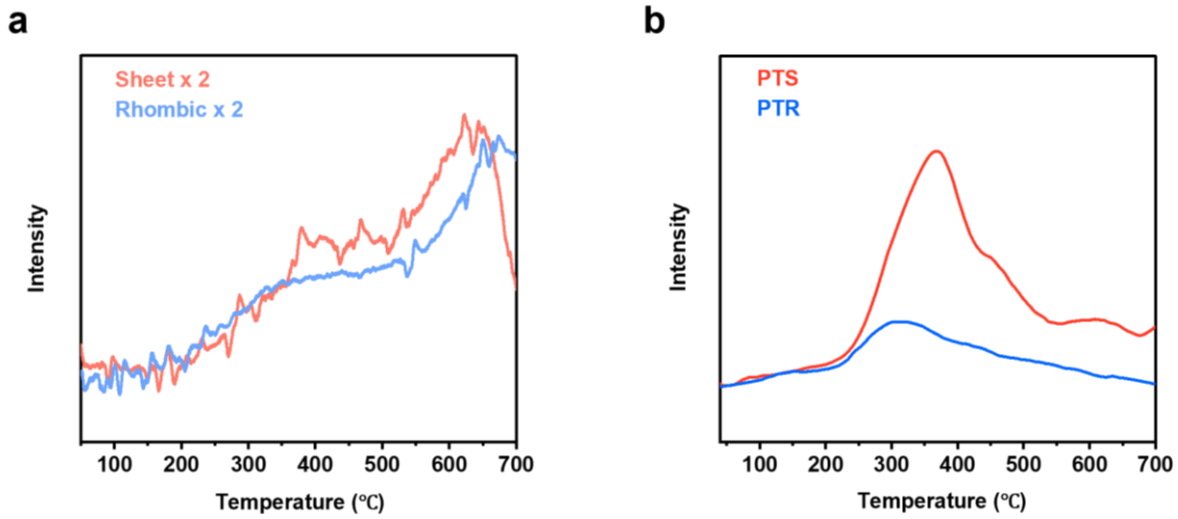

Supplementary Figure 41. Hydrogen reducibility of pristine and Pt-loaded TiO_2 catalysts. H_2-TPR profiles of (a) pristine TiO_2 supports and (b) Pt-loaded TiO_2 catalysts.

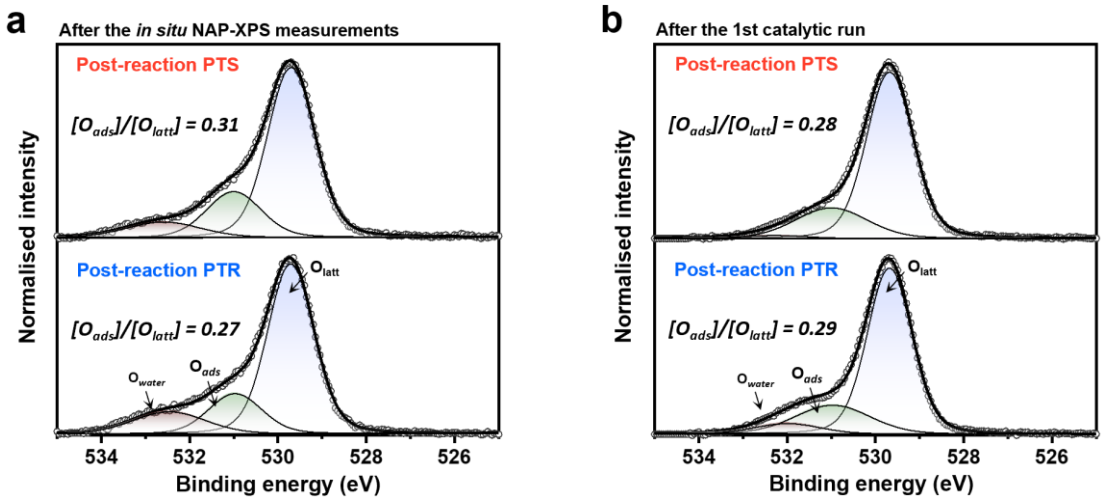

Supplementary Figure 42. Post-reaction evolution of surface oxygen species. Post-reaction O 1*s* XPS spectra of Pt/TiO_2 catalysts. (a) UHV O 1*s* spectra of PTS and PTR measured after the *in situ* NAP-XPS measurements sequence. (b) *Ex situ* UHV O 1*s* spectra of spent PTS and PTR obtained after the first catalytic run.

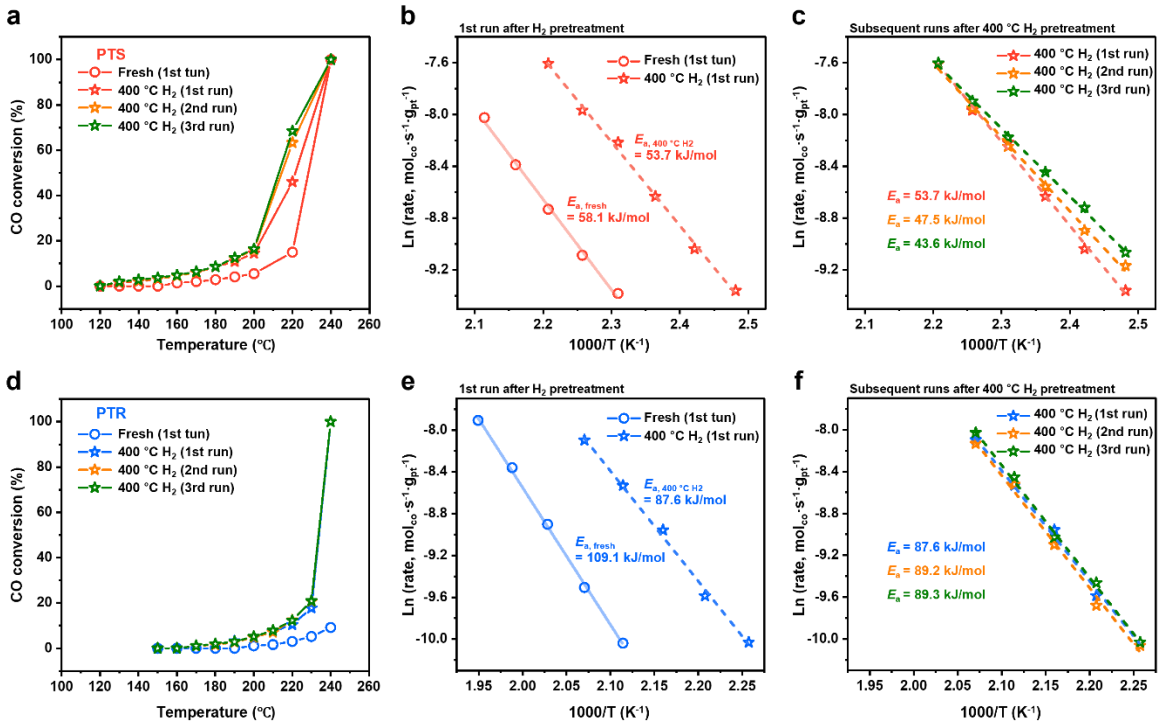

Supplementary Figure 43. Catalytic evolution of H_2-pretreated Pt/TiO_2 catalysts. Temperature-dependent CO conversion curves and Arrhenius plots for (a–c) PTS and (d–f) PTR after H_2 pretreatment at 400 °C. (a, d) Temperature-dependent CO conversion curves. (b, e) Arrhenius plots comparing the 1st-run activities of the fresh and 400 °C H_2-pretreated catalysts. (c, f) Arrhenius plots showing the subsequent catalytic runs after 400 °C H_2 pretreatment. For the 400 °C H_2-pretreated samples, the catalysts were held at 240 °C for 2 h under reaction conditions before the 2nd run. E_a values were calculated in the kinetically relevant regime (<10% CO conversion) at a total flow rate of 100 mL min^{-1} and a CO/O_2 ratio of 1.

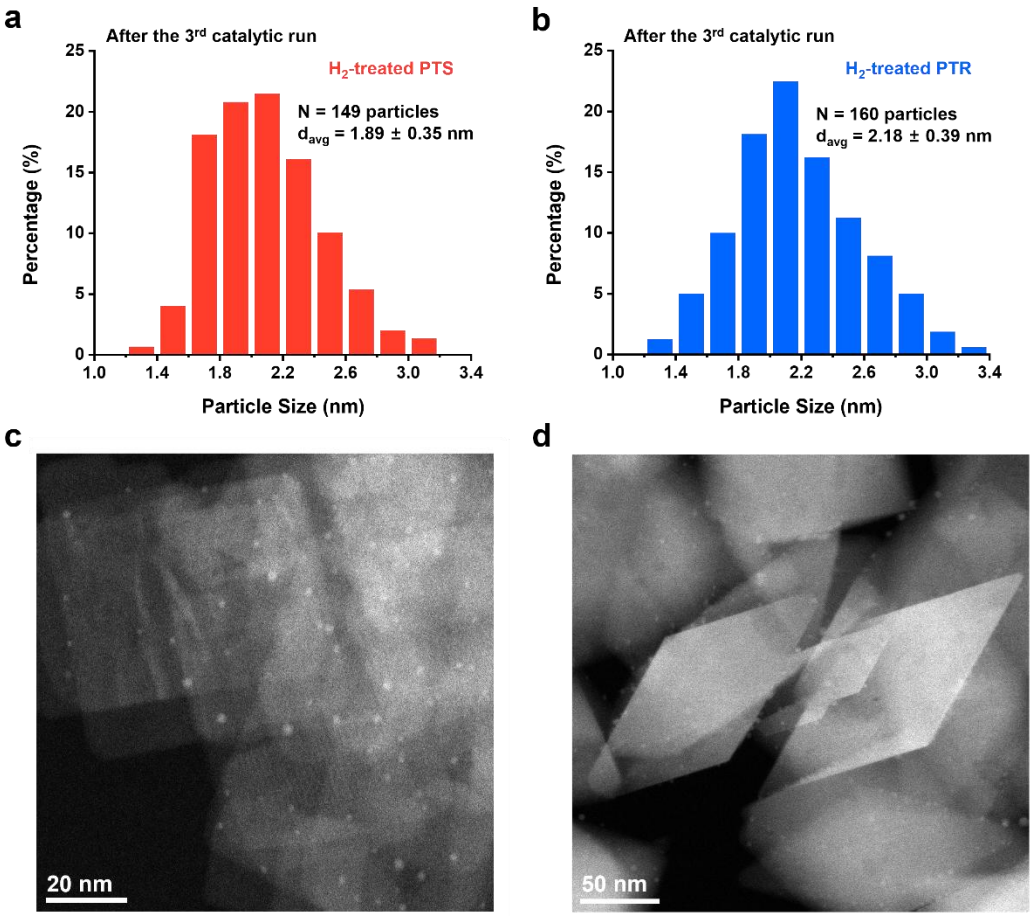

Supplementary Figure 44. Structural stability after H_2 pretreatment and catalytic cycling. (a, b) Histograms showing the Pt NP size distributions and (c, d) HAADF-STEM images of spent catalysts after the 3rd catalytic run following 400 °C H_2 pretreatment: (a, c) PTS and (b, d) PTR. Both catalysts show no significant sintering of Pt NPs or morphological degradation of the TiO_2 supports after H_2 pretreatment and subsequent CO oxidation cycles.

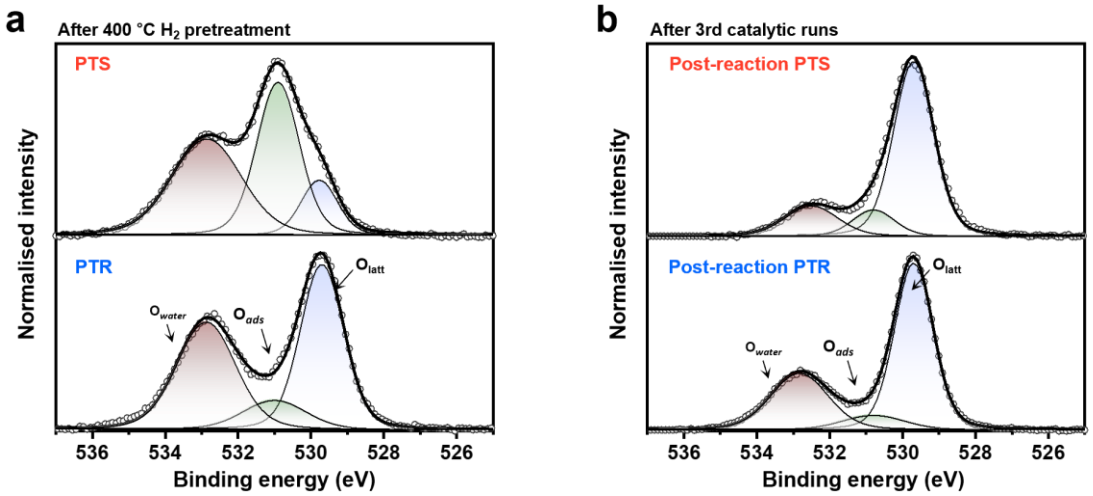

Supplementary Figure 45. Surface oxygen species following H_2 pretreatment and CO oxidation. O 1*s* XPS spectra of PTS and PTR after (a) H_2 pretreatment at 400 °C and (b) the 3rd CO oxidation run following the 400 °C H_2 pretreatment. The higher-binding-energy components include O_{ads} from adsorbed/hydroxyl- or defect-associated surface oxygen species and O_{water} from molecular or weakly bound water-related species.

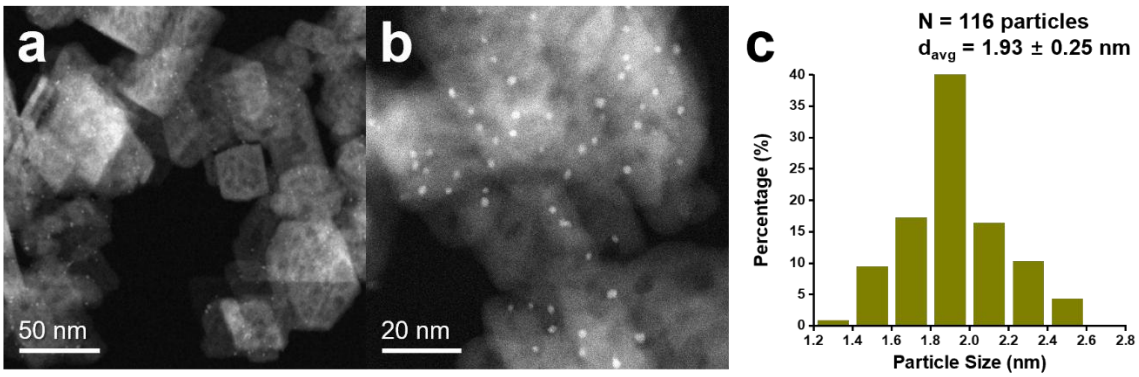

Supplementary Figure 46. Morphology and NP size distribution of the Pt/Al_2O_3 reference catalyst. (a, b) HAADF–STEM images of the as-prepared Pt/Al_2O_3 (PtA) catalyst. (c) Corresponding histograms showing the Pt NP size distributions for PtA.

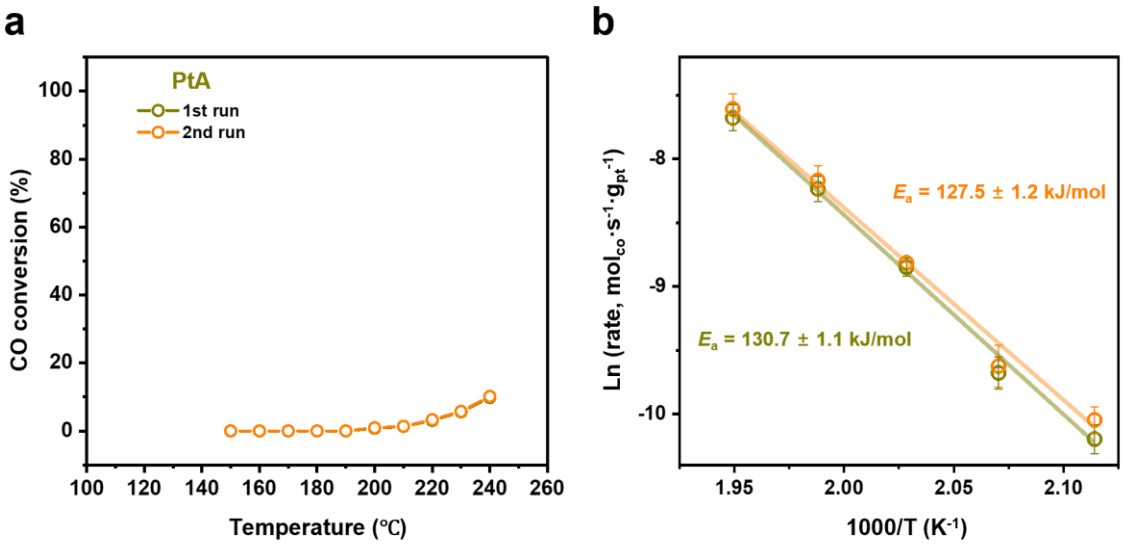

Supplementary Figure 47. Catalytic performance of the Pt/Al_2O_3 reference catalyst. (a) Temperature-dependent catalytic cycle tests and (b) corresponding apparent activation energies (E_a) for PtA. Two consecutive catalytic runs were performed for each catalyst in a single experiment over the temperature range up to 240 °C, where complete catalytic ignition was observed in the DRIFTS results. After the 1st run, the catalyst was held at 240 °C for 2 h before the 2nd run. All E_a values were obtained at a total flow rate of 100 mL·min^{-1} with a CO/O_2 ratio of 1 under the kinetically relevant regime (<10% CO conversion), and were averaged over three independent experiments using newly loaded catalysts to ensure reproducibility, with error bars representing the standard deviation.

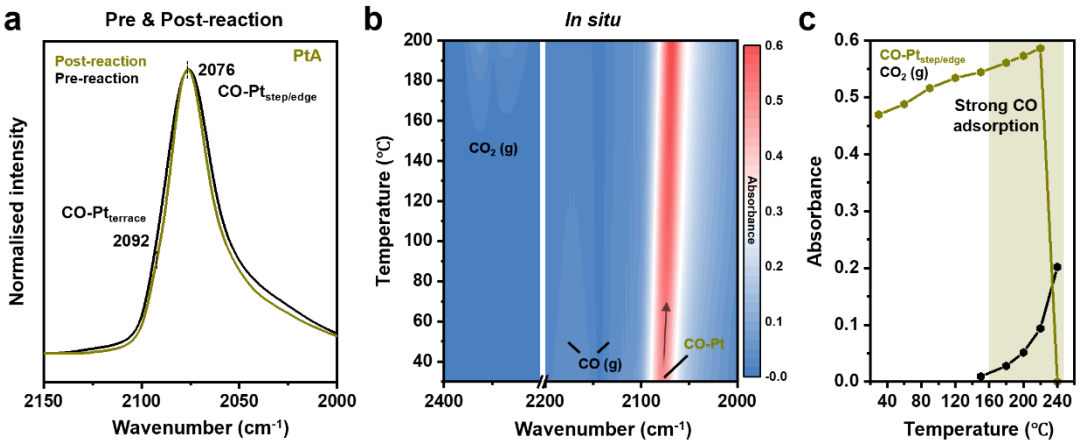

Supplementary Figure 48. CO adsorption behavior of the Pt/Al_2O_3 reference catalyst. *In situ* DRIFTS spectra of PtA catalyst during CO oxidation. (a) Normalised CO-DRIFTS spectra recorded pre- and post-CO oxidation at 25 °C. (b) Contour maps of *in situ* DRIFTS spectra acquired under CO oxidation. (c) Intensity plots tracking CO adsorbed on $Pt_{step/edge}$ sites and gas-phase CO_2 evolution.

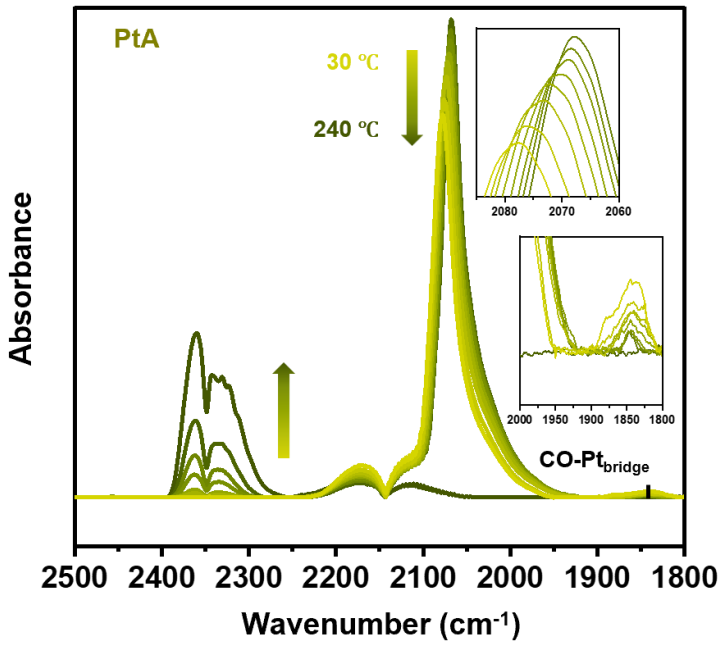

Supplementary Figure 49. Temperature-dependent CO adsorption on the Pt/Al_2O_3 reference catalyst. *In situ* DRIFTS spectra of PtA catalyst recorded under CO oxidation conditions ($CO/O_2 = 1$) at various temperatures. The spectra capture the temperature-dependent evolution of surface species, including CO adsorption and CO_2 formation.

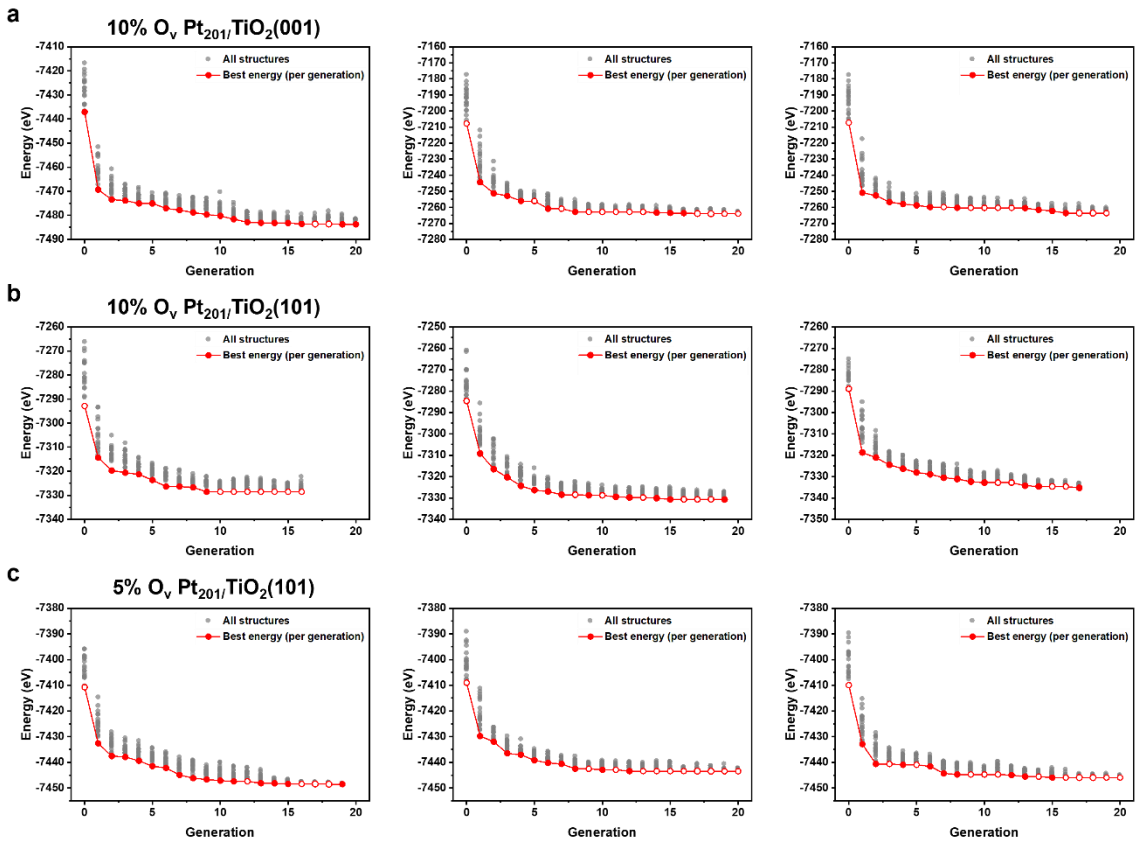

Supplementary Figure 50. GA optimisation of Pt NPs on oxygen-deficient TiO_2 surfaces. The evolution of total energies during the GA optimisation of Pt_{201} NPs on TiO_2 with surface O_v, shown for three independent random O_v configurations per facet: (a) 10% O_v $Pt_{201}/TiO_2(001)$, (b) 10% O_v $Pt_{201}/TiO_2(101)$, and (c) 5% O_v $Pt_{201}/TiO_2(101)$. Grey dots represent the energies of all candidate structures sampled in each generation, while the red line denotes the lowest-energy structure per generation. Filled red circles indicate generations where a new global minimum energy was identified, whereas open red circles indicate generations in which the global minimum remained unchanged.

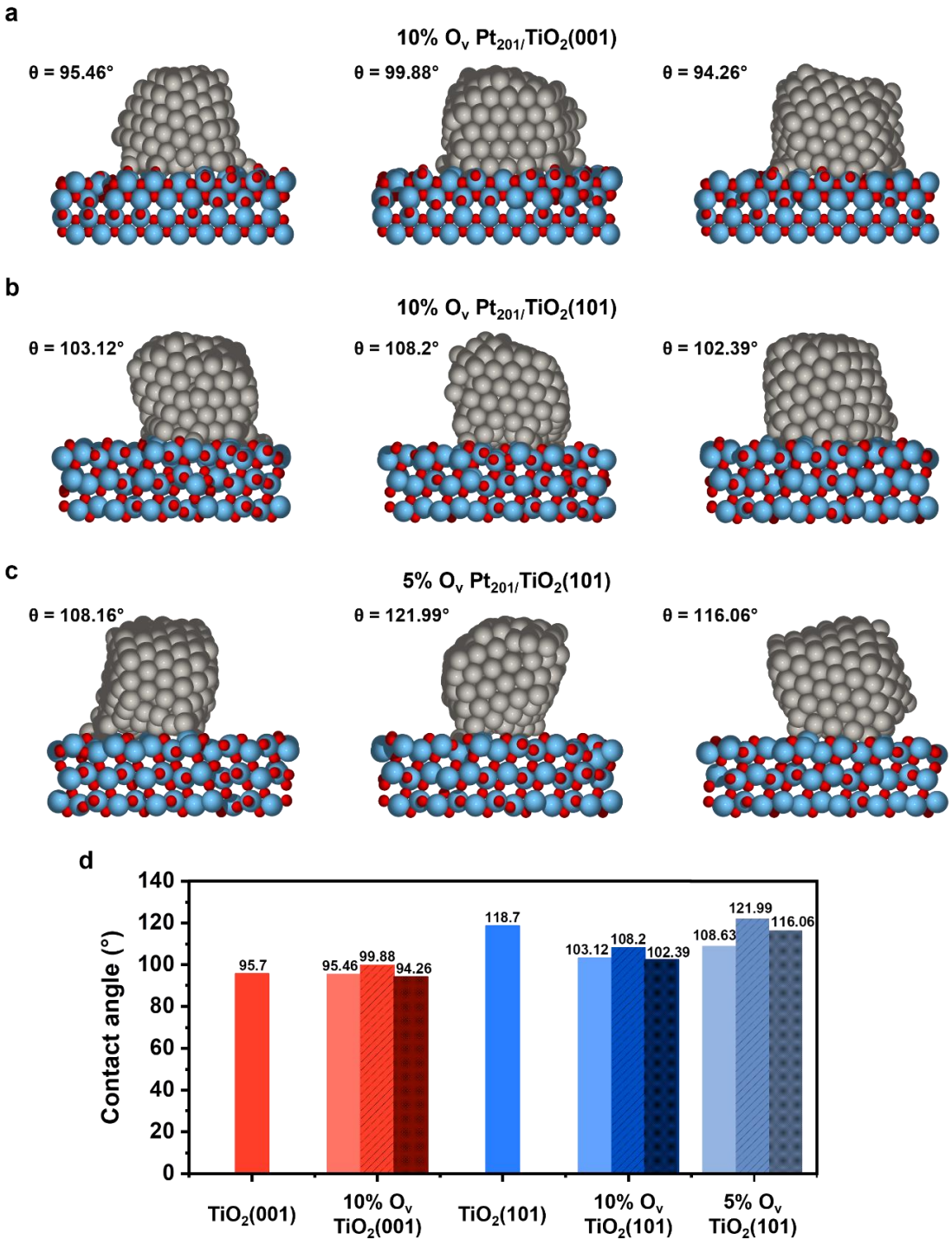

Supplementary Figure 51. Effect of oxygen vacancies on Pt NP wetting behavior. Side-view images of the lowest-energy Pt_{201} NP configurations on (a) 10% O_v TiO_2(001), (b) 10% O_v TiO_2(101), and (c) 5% O_v TiO_2(101), obtained by GA-based optimisation. Three independent O_v configurations were generated per facet by random placement to account for configurational variability of vacancy sites. The values indicated in side-view panels correspond to the effective contact angles (θ) of the Pt NPs on each O_v-modulated TiO_2 surfaces, extracted from the optimised geometries. (d) Summary of the contact angles obtained from the GA-optimised Pt_{201}/TiO_2 configurations on both stoichiometric and O_v-modulated TiO_2 surfaces.

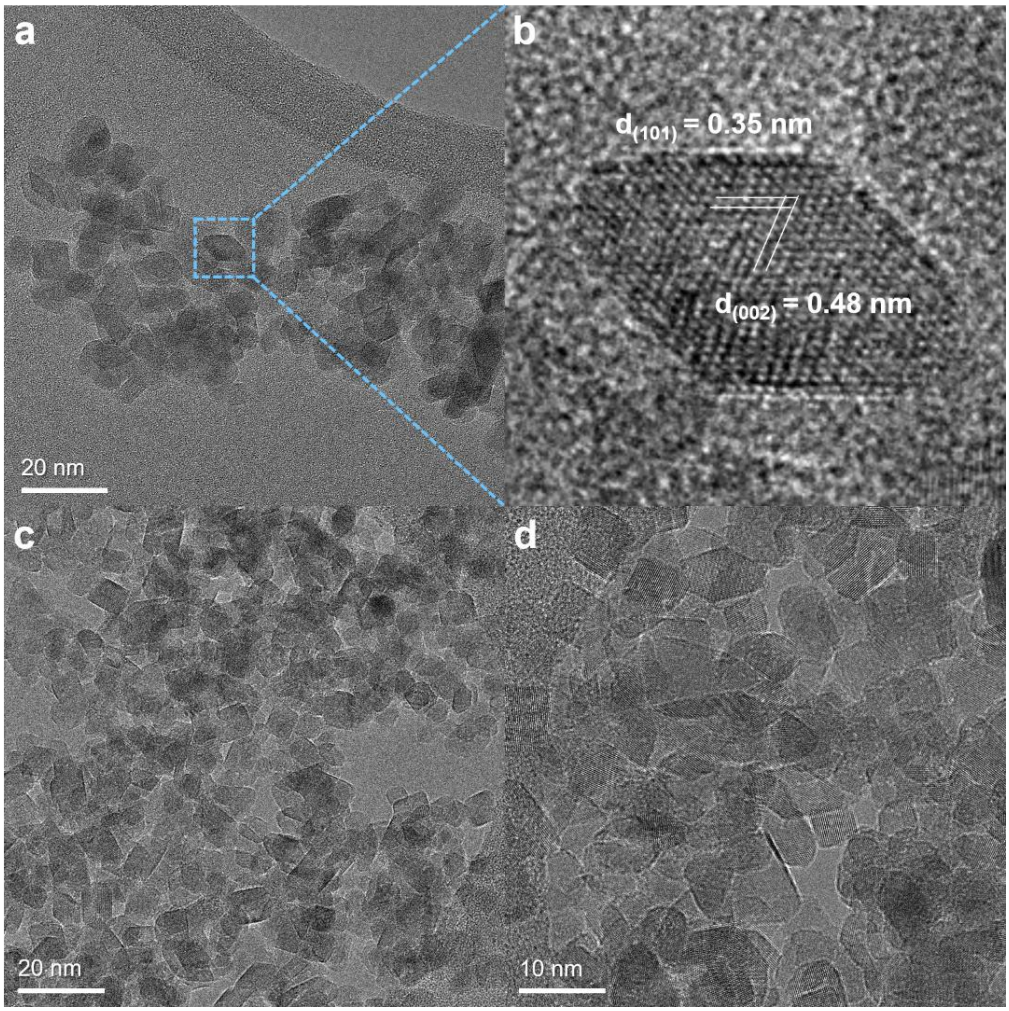

Supplementary Figure 52. Morphology of TiO_2-r crystals exposing predominantly the (101) facet. (a–d) TEM images of pristine TiO_2-r samples predominantly exposing the (101) facet, showing rhombic morphology. (b) Magnified HRTEM image of the boxed region in (a).

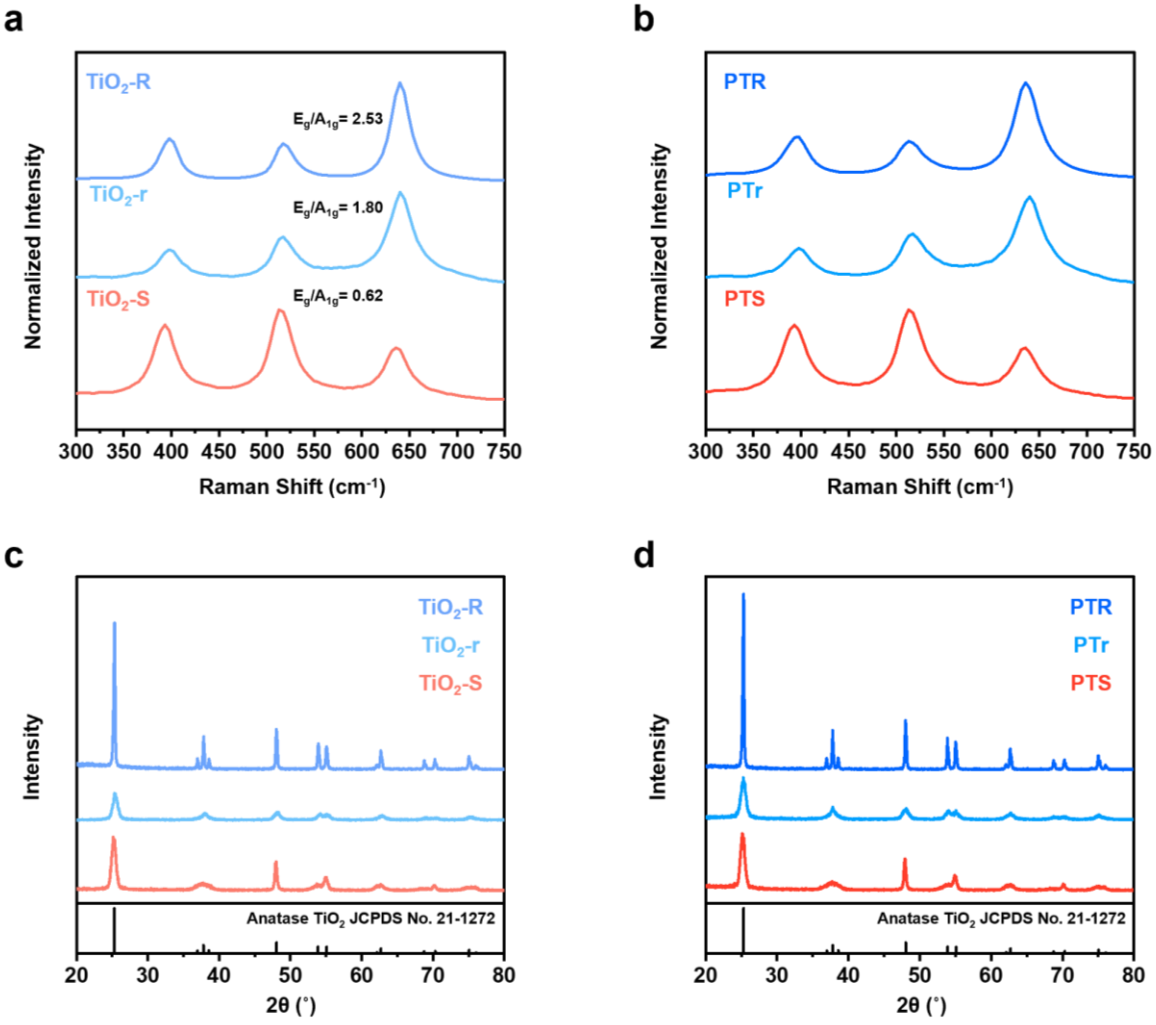

Supplementary Figure 53. Structural characterization of pristine and Pt-loaded catalysts. (a, b) Raman spectra of (a) pristine TiO_2 supports and (b) fresh Pt/TiO_2 catalysts. (c, d) XRD patterns of (c) pristine TiO_2 and (d) fresh Pt/TiO_2 catalysts.

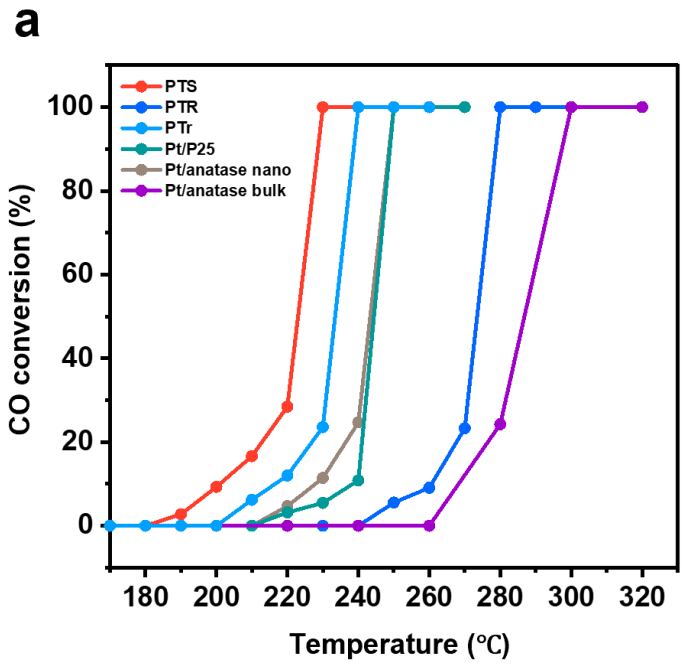

Supplementary Figure 54. Catalytic performance of Pt catalysts supported on different TiO_2 materials. CO conversion curves of Pt/TiO_2 catalysts prepared using synthesized TiO_2 supports (TiO_2-S, TiO_2-r, and TiO_2-R) and commercial TiO_2 powders (P25, anatase nanopowder, and bulk powder). Catalytic tests were conducted under a 2% CO + 2% O_2/Ar flow (Total 50 $mL \cdot min^{-1}$).

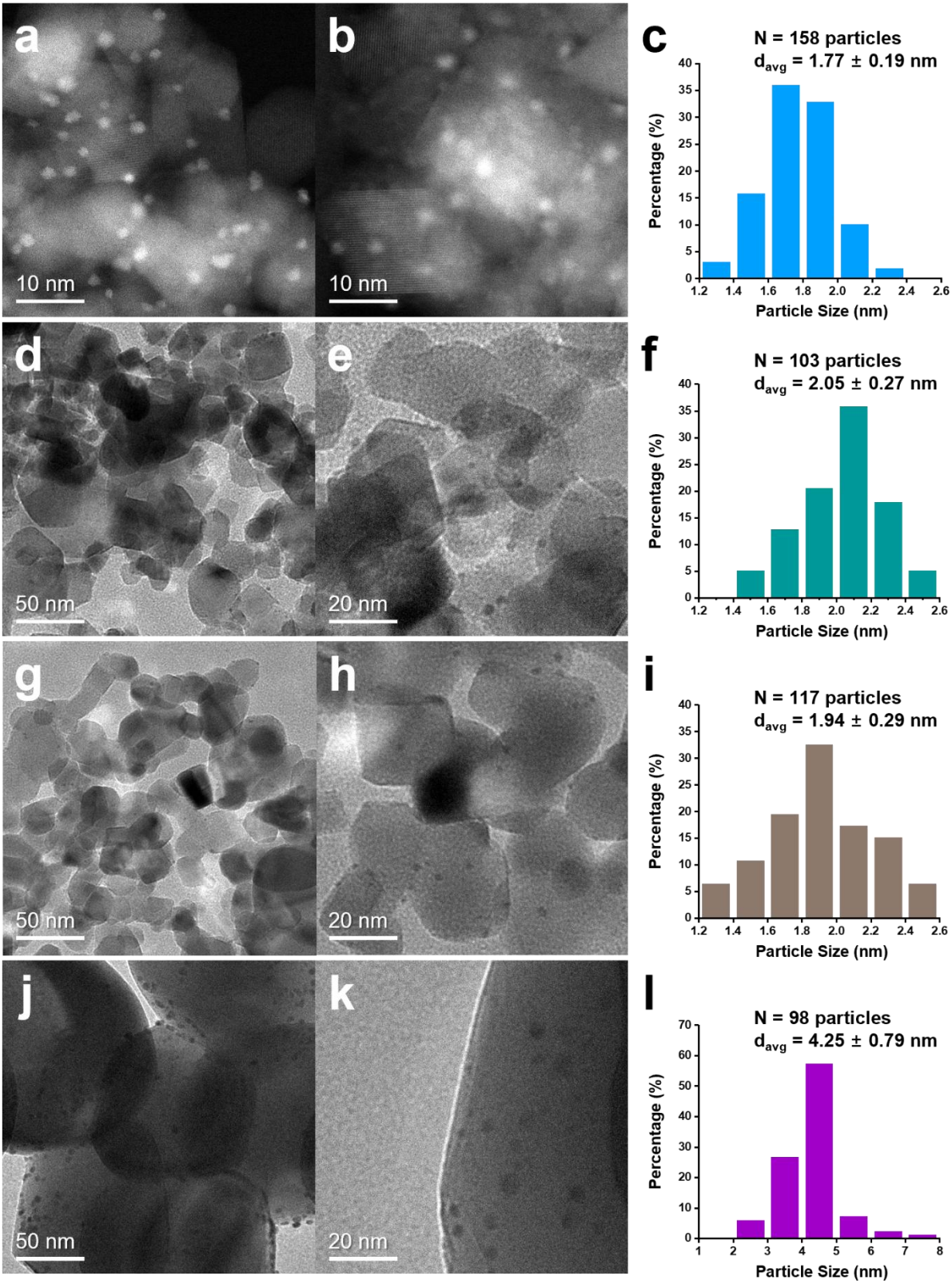

Supplementary Figure 55. Morphology and NP size distributions of Pt catalysts supported on different TiO_2 materials. HAADF–STEM images and corresponding Pt NP size distributions of Pt catalysts supported on (a–c) TiO_2-r (PTr), (d–f) commercial P25, (g–i) anatase nanopowder, and (j–l) anatase bulk powder.

Supplementary Table 8. Specific surface areas of pristine TiO_2 samples measured by the BET method.

Catalysts	Specific surface area ($m^2 \cdot g^{-1}$)
TiO_2 nanosheet (001), (TiO_2-S)	70.3
PTS	69.1
TiO_2 large rhombic (101), (TiO_2-R)	14.4
PTR	13.0
TiO_2 small rhombic (101), (TiO_2-r)	119.5
P25	51.8
Anatase nanopowder	52.2
Anatase bulk powder	8.9

*All samples were pretreated at 80 ℃ for overnight under vacuum

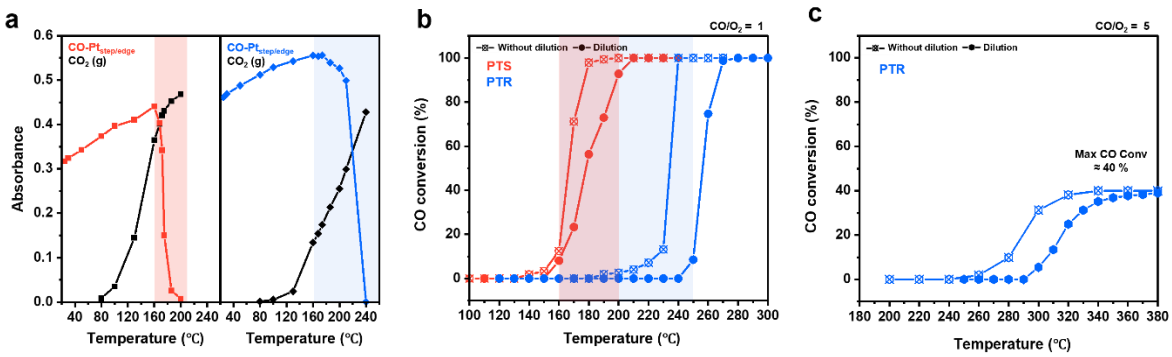

Supplementary Figure 56. Additional validation of catalytic ignition behavior. (a) Intensity plots tracking CO adsorbed on $Pt_{step/edge}$ sites and gas-phase CO_2 evolution under the $CO/O_2 = 1$ condition, corresponding to the data shown in Fig. 3. (b–c). Temperature-dependent CO conversion profiles of PTS and PTR catalysts, comparing diluted and undiluted catalyst beds under (b) $CO/O_2 = 1$ and (c) $CO/O_2 = 5$ conditions. The colored region highlights the catalytic ignition temperature range that matches the ignition behavior observed in both the *in situ* DRIFTS measurements and the reactivity tests under the $CO/O_2 = 1$ condition.

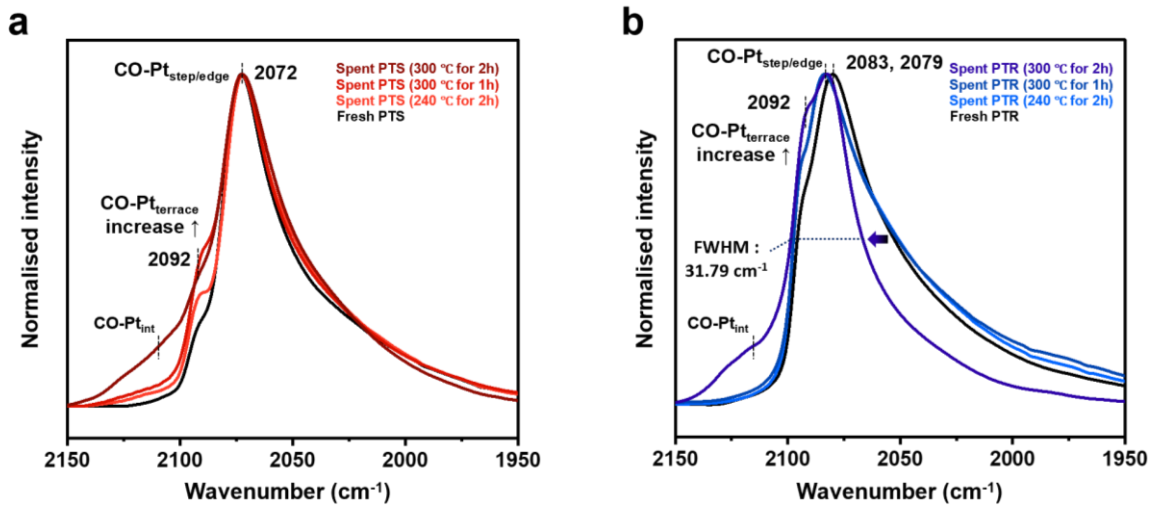

Supplementary Figure 57. Post-reaction CO adsorption following different thermal treatments. Post-reaction CO-DRIFTS spectra of (a) PTS and (b) PTR catalysts. The spent catalysts were prepared by post-reaction treatments at 240 °C for 2 h, 300 °C for 1 h, and 300 °C for 2 h under CO/O_2 = 1 reaction conditions prior to DRIFTS measurements.

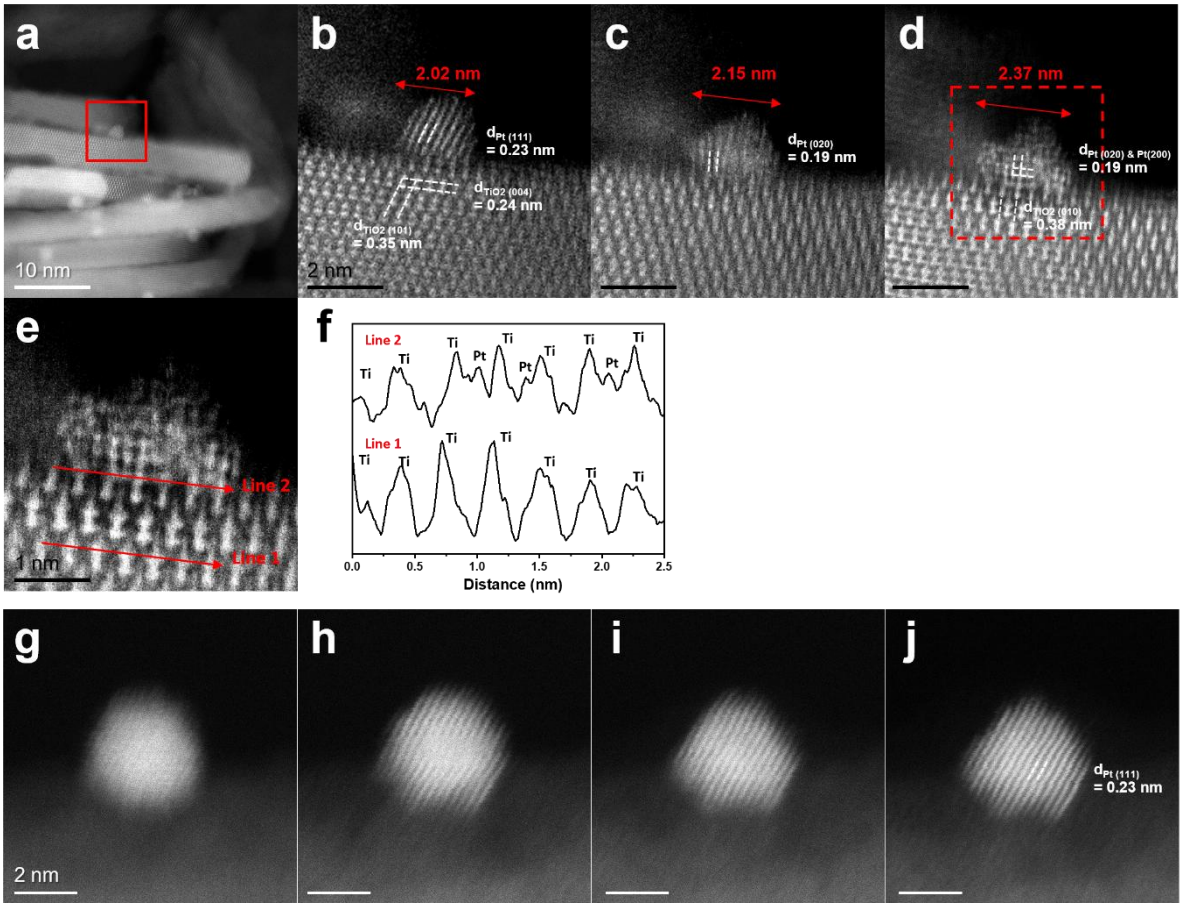

Supplementary Figure 58. Electron beam-induced reconstruction of Pt NPs. (a) HAADF–STEM image of fresh PTS catalyst. (b–d) Electron beam-induced reconstruction of Pt NPs within the red rectangular region in (a) under magnifications of (b) 5 M, (c) 8 M, and (d) 20 M. (e) Enlarged view of the red dashed rectangle in (d). (f) Intensity profiles extracted along the line in (e), showing changes in lattice spacings during reconstruction. (g–j) HAADF–STEM images of fresh PTR catalyst at magnifications of (g–i) 10 M and (j) 12 M, illustrating beam-induced morphological evolution of Pt NPs.

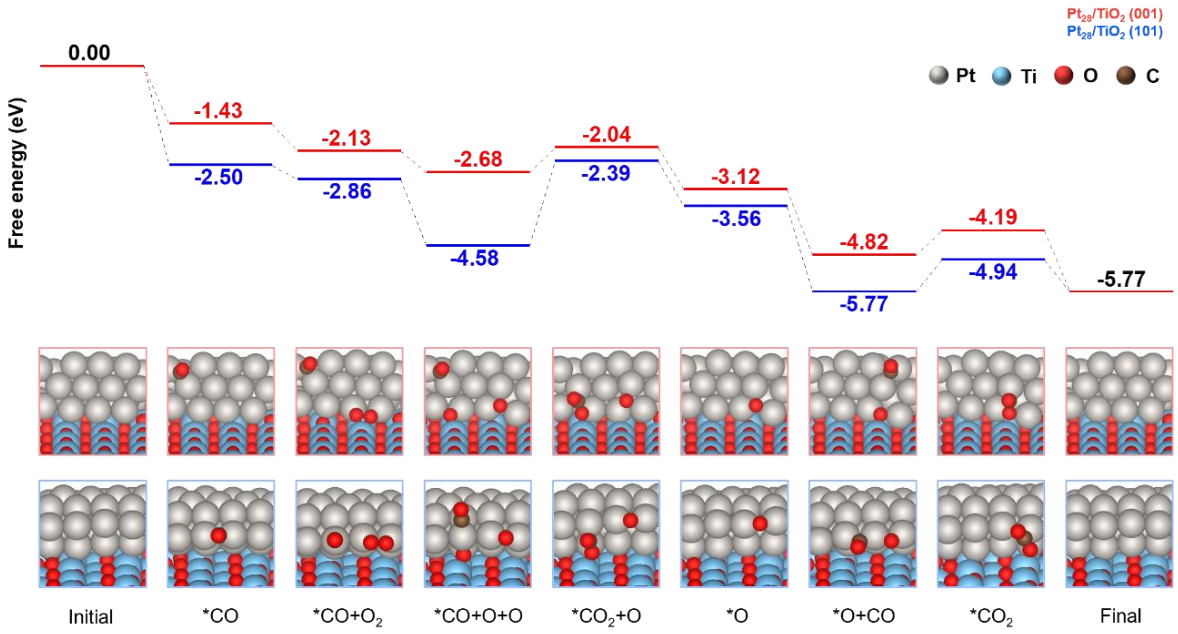

Supplementary Figure 59. Reaction energy profiles for the Langmuir–Hinshelwood pathway. Reaction energy profiles for CO oxidation via the L–H mechanism on $Pt_{28}/TiO_2(001)$ and $Pt_{28}/TiO_2(101)$ models. The energy barriers associated with the co-adsorbed *CO and *O reaction step highlight the facet-dependent differences in activation energy and rate-determining steps.

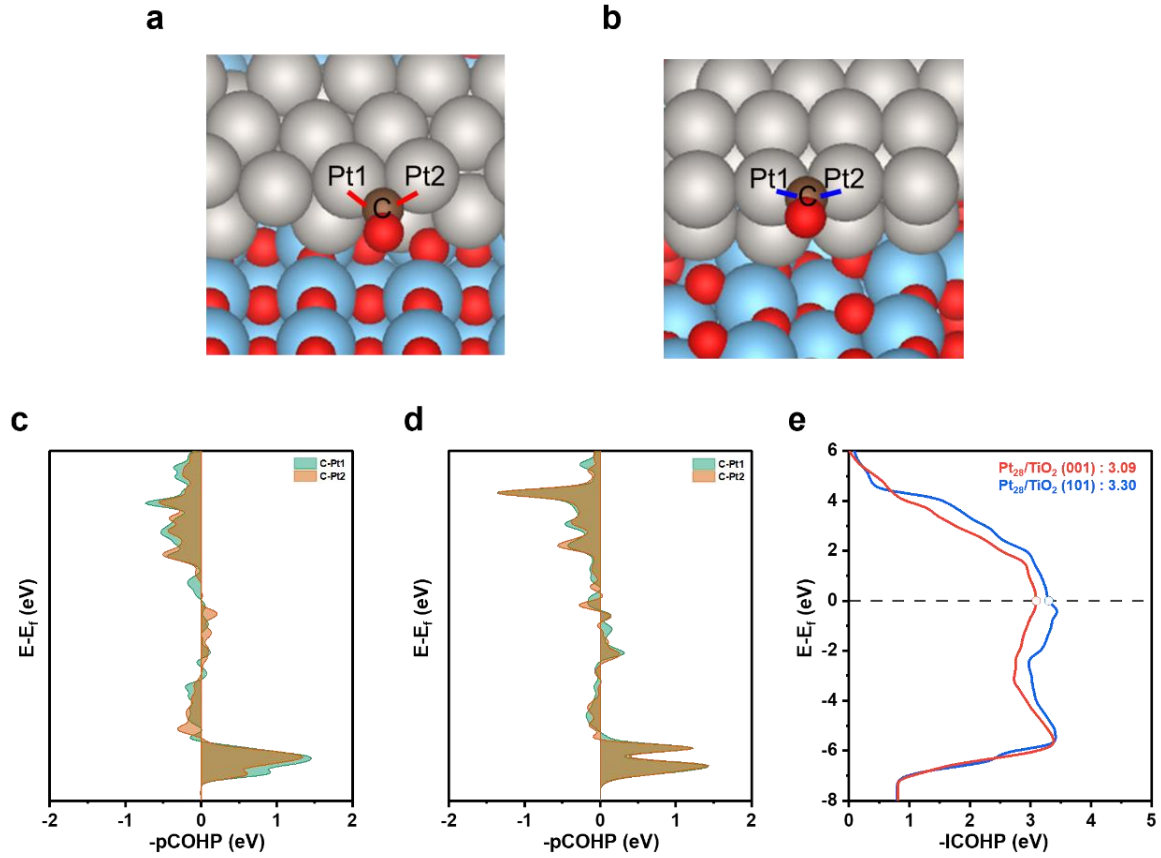

Supplementary Figure 60. Electronic interactions governing CO adsorption on Pt/TiO_2 interfaces. The active CO adsorption site and corresponding Pt–C bonds for (a) $Pt_{28}/TiO_2(001)$ and (b) $Pt_{28}/TiO_2(101)$, along with the −pCOHP analysis of CO adsorption at the Pt site for (c) $Pt_{28}/TiO_2(001)$ and (d) $Pt_{28}/TiO_2(101)$, and the corresponding integrated −COHP (−ICOHP) curves in (e). Colored curves in (c, d) represent the −pCOHP for individual Pt–C bonds between the adsorbed CO molecule (C atom) and the neighboring Pt atoms indicated in (a) and (b).

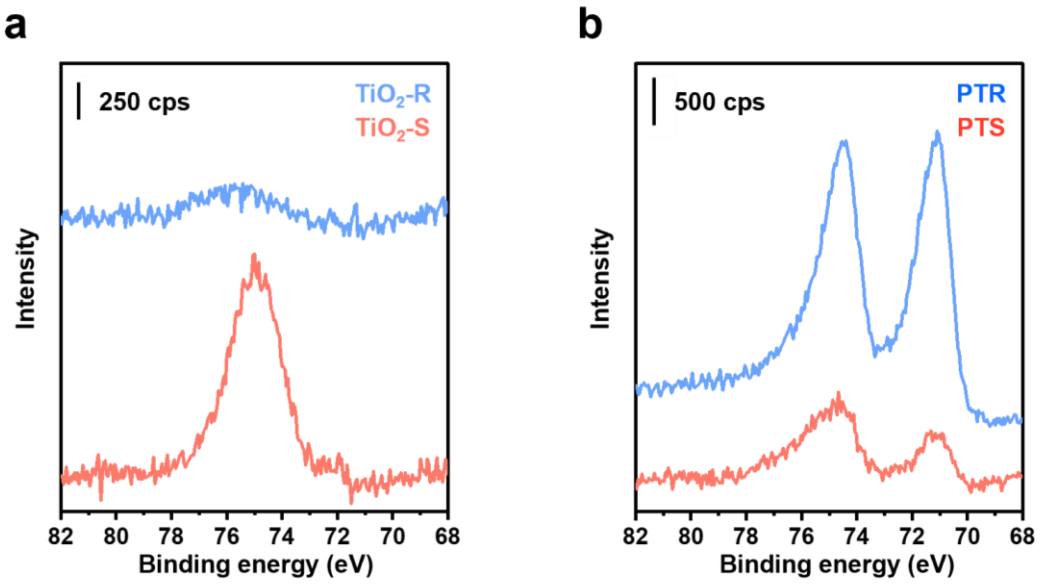

Supplementary Figure 61. Additional XPS characterization of TiO_2 supports and Pt/TiO_2 catalysts. (a) Ti 3*s* satellite spectra of TiO_2-S and TiO_2-R supports. (b) Pt 4*f* XPS spectra of PTS and PTR catalysts measured under UHV conditions.

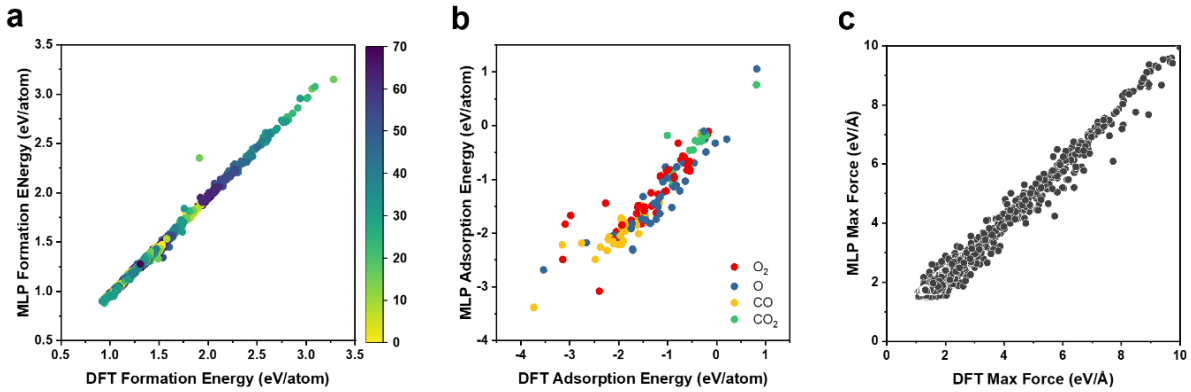

Supplementary Figure 62. Validation of the graph neural network potential against DFT calculations. Validation of the PFP GNN potential through comparison with DFT calculations. (a) Parity plot of Pt cluster formation energies predicted by PFP and DFT (b) Comparison of adsorption energies for key CO oxidation intermediates on Pt/TiO_2 surfaces calculated by PFP and DFT (c) Parity comparison of maximum atomic forces during structure optimisation between PFP and DFT.

Supplementary Note 1. Methods for Synthesizing Rhombic TiO_2 with Predominantly Exposed (101) Facets

In this study, we compared two anatase TiO_2 morphologies with predominantly exposed (001) and (101) facets. The synthesis of TiO_2 with predominantly exposed (001) facets typically involves the use of hydrofluoric acid (HF) during the hydrothermal stage, as F^- ions inhibit crystal growth along the [001] direction, leading to sheet-like morphologies with extensive (001) exposure. In contrast, anatase TiO_2 with predominantly exposed (101) facets can be obtained via three main strategies: (1) reducing the amount of HF during synthesis,[3, 4] (2) employing $Ti(OH)_4$ precursors derived from $TiCl_4$ hydrolysis,[5] and (3) using Na-titanate precursors formed by alkali treatment of commercial P25 TiO_2.[6] Among these, method (1) tends to result in relatively low (101) facet exposure, so we focused on methods (2) and (3), which are consistent with previous reports on facet-controlled catalysis.[5, 7, 8, 9]

As shown in Supplementary Fig. 52, TiO_2 synthesized via method (2) exhibited small crystals with rhombic morphology. However, a considerable portion of the sample lacked well-defined shapes. Although this observation is not explicitly discussed in prior studies, similar morphology appears in published TEM images, likely due to the small crystallite sizes (<10 nm edge length). Because this work aims to investigate how exposed TiO_2 facets affect Pt NP reconstruction and catalytic CO oxidation, well-defined TiO_2 morphologies are essential to isolate the facet effects. Therefore, method (3) was adopted to produce larger rhombic TiO_2 crystals with a high percentage of exposed (101) facets. As shown in Fig. 1, the TiO_2 product from method (3) exhibits a well-defined rhombic shape, although the surface area is reduced due to the increased crystallite size

Accordingly, we designated the TiO_2 synthesized by method (2) as TiO_2-r (small rhombic) and that by method (3) as TiO_2-R (large rhombic). The corresponding Pt-supported catalysts are referred to as PTr and PTR, respectively. Supplementary Fig. 53 compares their surface and crystal structures using Raman spectroscopy and XRD. Raman spectra show that TiO_2-r exhibits a higher E_g/A_{1g} intensity ratio (1.80) than TiO_2-R (2.53), while XRD confirms that all samples retain the anatase phase. This suggests that although TiO_2-r maintains the anatase structure, it does not expose the (101) facets as fully as TiO_2-R. Thus, TiO_2-R was selected for subsequent studies due to its more complete (101) facet exposure, which enables clearer identification of Pt reconstruction on well-defined (101) terrace surfaces.

To further assess the facet-dependent catalytic activity, we compared Pt/TiO_2 catalysts synthesized using these TiO_2 supports with those made from commercial TiO_2 (P25, anatase

nano powder, and bulk powder) (Supplementary Fig. 54). TEM images and Pt NP size distributions are provided in Supplementary Fig. 55. While the catalytic activity generally increased with increasing surface area (Supplementary Table 8), PTS (Pt supported on TiO_2 with exposed (001) facets) showed superior activity compared to all other samples, including PTr, despite TiO_2-r having 1.7 times larger surface area than TiO_2-S. This indicates that the (001) facet of TiO_2-S provides a more catalytically active environment for CO oxidation than the (101) facets of TiO_2-R or any commercial TiO_2 sample.

Taken together, these findings confirm that although surface area is an important factor in catalytic performance, the enhanced activity of PTS originates primarily from the intrinsic reactivity of the exposed (001) facet, not from surface area effects. Therefore, TiO_2-R synthesized via method (3) was used in the main study to reliably investigate the influence of the (101) facet on Pt structural evolution and CO oxidation catalysis.

Supplementary Note 2. Rationale for Post-Reaction Treatment Conditions

To prepare spent catalysts for post-reaction structural analysis, the final reaction temperatures were initially set to 300 °C for 2 h under CO/O_2 = 0.2 and 1, 350 °C for 2 h under CO/O_2 = 3, and 400 °C for 2 h under CO/O_2 = 5. These temperatures correspond to reaction conditions well above those required to achieve complete CO conversion in the reactivity comparison experiments (Fig. 1e and Supplementary Fig. 4), where both PTS and PTR had already surpassed 100% CO conversion. The use of such harsher temperatures was intended to ensure sufficient exposure of the catalysts to reaction environments prior to structural characterization.

STEM analysis of the spent catalysts treated under these conditions revealed that the overall facet-dependent Pt morphology was preserved across different reaction atmospheres (Supplementary Figs. 14 and 15). However, a pronounced increase in Pt NP size was observed for PTR, with the average Pt size increasing from 1.83 nm to 3.18 nm, whereas PTS remained largely resistant to NP growth under the same conditions. This observation indicates that, in addition to CO-induced Pt reconstruction (which is discussed based on *in situ* DRIFTS measurements in the main text), thermally driven sintering occurred for PTR under the high-temperature treatment conditions.

We attribute this sintering behavior of PTR to the use of a highly diluted catalyst bed during the reactivity tests, which inherently required higher reaction temperatures to reach complete CO conversion. As a result, the temperatures employed for preparing the spent catalysts were harsher than necessary to induce Pt NP reconstruction alone and could also promote thermally driven sintering, particularly for PTR, as evidenced by the significant increase in average Pt NP size under all measured conditions (Supplementary Fig. 15). Consequently, for samples treated under these conditions, size-related effects cannot be excluded from the interpretation of the corresponding DRIFTS and EXAFS structural analyses.

To eliminate thermally induced sintering effects while preserving CO-adsorbate-driven reconstruction, the final reaction temperature for preparing spent catalysts was therefore lowered to 240 °C. This temperature was selected based on *in situ* DRIFTS results showing that complete catalytic ignition occurs for both PTS and PTR at approximately 240 °C (Figs. 3 and 5). We further confirmed that undiluted catalysts reach 100% CO conversion within the same temperature range (Supplementary Figs. 56a, b). After holding the samples at 240 °C for 2 h under CO/O_2 = 1, both PTS and PTR exhibited no significant sintering in their post-reaction Pt size distributions (Supplementary Figs. 12 and 13). Under these conditions, the observed Pt morphology reflects the intrinsic facet-dependent influence of the TiO_2 support together with

reconstruction induced by adsorbed CO during reaction, allowing post-reaction structural analyses to be interpreted without contributions from sintering.

For spent catalyst analysis under $CO/O_2 = 0.2$, the same treatment condition (240 °C for 2 h) was applied to eliminate any influence arising solely from differences in the final reaction temperature. For $CO/O_2 = 5$, the catalyst was treated at 350 °C for 2 h, corresponding to the temperature at which the undiluted PTR catalyst reached its maximum achievable CO conversion (~40%), as shown in Supplementary Fig. 56c. Although this treatment temperature is lower than that used initially, it still lies within a regime where sintering may occur; therefore, this possibility is explicitly considered when interpreting the corresponding STEM and EXAFS results.

To further validate that sintering effects are excluded under the selected post-reaction conditions, additional CO-DRIFTS measurements were performed after a treatment at 300 °C for 1 h and compared with the post-reaction spectra obtained at 240 °C for 2 h and 300 °C for 2 h, as well as with those of the size-controlled Pt/TiO_2 catalysts.

Comparison of the DRIFTS spectra of the fresh catalysts with those collected after treatment at 240 °C for 2 h and 300 °C for 1 h (Supplementary Fig. 57) shows that both PTS and PTR exhibit moderate increases in terrace-related features. For PTS, the main CO adsorption band remains centered at ~2072 cm^{-1}, accompanied by a gradual increase in terrace contribution. For PTR, a modest shift of the CO band toward higher wavenumbers (2079 → 2083 cm^{-1}) is observed together with enhanced terrace-site intensity. Importantly, under both conditions, the overall peak shapes for PTS and PTR remain similar to those of their fresh counterparts, indicating that significant NP growth has not occurred.

As discussed above, PTS exhibits higher resistance to sintering. Accordingly, even after treatment at 300 °C for 2 h, the spent PTS catalyst shows only gradual increases in terrace-related and CO–Pt_{int} features without substantial changes in peak shape. In contrast, the spent PTR catalyst treated at 300 °C for 2 h displays a distinctly different spectral profile, characterized by a pronounced narrowing of the full width at half maximum (FWHM), as highlighted in Supplementary Fig. 57. This spectral narrowing is consistent with NP growth to approximately 3.1 nm, as independently confirmed by STEM analysis (Supplementary Fig. 18).

Consistent trends are observed from the post-reaction CO-DRIFTS spectra of the size-controlled Pt/TiO_2 catalysts (Supplementary Fig. 20), where Pt NPs larger than ~3 nm systematically exhibit narrowed FWHM values and terrace-dominated spectral features. The strong similarity—aside from minor FWHM differences—between the post-reaction DRIFTS

spectrum of the spent PTR catalyst treated at 300 °C for 2 h and those of the 3.04–4.81 nm size-controlled Pt/TiO_2(101) catalysts confirms that the 300 °C for 2 h treatment introduces a substantial sintering contribution in addition to intrinsic reconstruction effects.

By contrast, the DRIFTS spectra of spent PTR catalysts obtained after treatment at 240 °C for 2 h and 300 °C for 1 h closely resemble those of the fresh PTR catalyst. The preservation of the overall peak profiles—without the FWHM narrowing characteristic of NP growth—demonstrates that these conditions are not influenced by sintering. Accordingly, the terrace-related spectral changes observed under these conditions can be attributed to Pt NP reconstruction driven by facet-dependent metal–support interactions rather than by size-induced effects.

Supplementary Note 3. Facet-Dependent Pt NP Morphology Across Different NP Sizes

To further elucidate whether the facet-dependent Pt morphologies observed in this study persist across different NP sizes, additional experiments were conducted using size-controlled Pt/TiO_2 catalysts with average Pt diameters ranging from 1.5 to 5 nm. This size regime was intentionally selected because the dominant fractions of exposed Pt surface sites—particularly under-coordinated step/edge sites versus well-coordinated terrace sites—are known to vary substantially with NP size according to geometric NP models.[10] All size-controlled catalysts were subjected to identical post-reaction treatment at 240 °C for 2 h prior to structural and spectroscopic analyses. STEM images and corresponding Pt size distributions of the size-controlled catalysts (Supplementary Figs. 17 and 18) confirm well-defined Pt NPs across the investigated size range. High-magnification STEM images (Supplementary Fig. 19) reveal a consistent facet-dependent trend in Pt morphology that is largely preserved across different NP sizes. Regardless of size, Pt NPs supported on $TiO_2(001)$ preferentially adopt hemispherical geometries characterized by broad metal–support contact areas, whereas Pt NPs on $TiO_2(101)$ exhibit more faceted morphologies with smaller interfacial contact regions. As the NP size increases toward approximately 4 nm, Pt NPs on $TiO_2(001)$ gradually evolve toward more faceted shapes due to geometric size effects. Nevertheless, even in this size regime, the interfacial contact area between Pt and $TiO_2(001)$ remains noticeably larger than that observed for Pt NPs on $TiO_2(101)$, indicating that facet-dependent metal–support interactions continue to influence the equilibrium morphology beyond purely size-driven effects.

Post-reaction CO–DRIFTS spectra of the size-controlled catalysts (Supplementary Fig. 20) provide further insight into the relationship between NP size, surface coordination, and facet-dependent Pt morphology. As the Pt NP size increases, both $Pt/TiO_2(001)$ and $Pt/TiO_2(101)$ catalysts exhibit an increased relative intensity of the CO–$Pt_{terrace}$ feature (2100–2080 cm^{-1}) compared to the CO–$Pt_{step/edge}$ feature (2080–2060 cm^{-1}). This trend is consistent with geometric NP models, in which the fraction of exposed terrace sites increases with NP size. In addition, Pt NPs with average post-reaction sizes exceeding approximately 3 nm exhibit sharper CO adsorption bands with reduced full width at half maximum (FWHM) compared to sub-3-nm NPs. This spectral sharpening is consistent with enhanced dipole–dipole coupling of adsorbed CO molecules on flatter, more extended terrace surfaces, as reported previously for supported Pt NPs.[10, 11] Importantly, clear facet-dependent differences are observed even within comparable Pt size regimes. For example, a $Pt/TiO_2(001)$ catalyst with an average Pt size of 2.72 nm exhibits a CO adsorption peak at 2081 cm^{-1}, whereas a $Pt/TiO_2(101)$ catalyst—despite

its smaller average size of 1.99 nm—shows a higher-wavenumber peak at 2083 cm^{-1}. Although CO adsorption bands generally shift to higher wavenumbers with increasing NP size due to stronger dipole–dipole interactions, the larger Pt NPs on TiO_2(001) nonetheless display lower-wavenumber CO adsorption peaks than the smaller Pt NPs on TiO_2(101). Moreover, a distinct CO–$Pt_{terrace}$ feature is already evident for the smallest Pt/TiO_2(101) catalyst (1.59 nm). Across all catalysts with comparable Pt NP sizes, Pt/TiO_2(101) consistently exhibits more pronounced terrace-related spectral features than Pt/TiO_2(001), indicating a higher proportion of well-coordinated, faceted Pt surfaces on the TiO_2(101) facet—even when the NPs are small.

These combined STEM and CO–DRIFTS results demonstrate that the observed differences in Pt morphology and surface coordination are predominantly governed by the TiO_2 facet rather than by NP size alone. As discussed in the Introduction, the Wulff–Kaischew theorem predicts that the equilibrium morphology of supported metal NPs is determined by the balance between the metal–support interfacial free energy and the intrinsic surface free energy of the metal. In line with this framework, the stronger Pt–TiO_2 interaction on the TiO_2(001) facet favors hemispherical NPs with broader metal–support contact areas, whereas the weaker interaction on TiO_2(101) allows Pt to adopt more stable faceted geometries with higher terrace-site exposure. Importantly, these facet-dependent trends persist across a broad NP-size range, confirming that facet-dependent MSI play a dominant role in determining Pt NPs morphology and surface structure in this system, beyond purely geometric size effects.

Supplementary Note 4. Limitation of STEM Analyses and Indirect Evidence of Facet-Dependent Pt Reconstruction Behaviour

During TEM analysis of the PTS catalyst, it was difficult to manually align the Kikuchi patterns (i.e., zone axis) due to the small crystal size (~3–5 nm) of the TiO_2 nanosheets along the [001] direction. Therefore, observations were focused on the side view of the TiO_2 nanosheets, which were perpendicularly loaded onto the Cu grid, particularly targeting Pt NPs located near the edges of the (001) surface to minimize contrast differences between TiO_2 and Pt. As shown in Fig. 2h, our analysis concentrated on the parallel lattice alignment between the Pt(200) and TiO_2(004) planes, in contrast to the atomic-level interfacial structure of PTR discussed in Fig. 2j. We attempted to obtain similar atomic-resolution images of the PTS interface after the reaction; however, resolving the interfacial atomic structure with sufficient clarity remained challenging (Supplementary Figs. 12).

Interestingly, electron beam-induced reconstruction of Pt NPs was observed during STEM imaging of fresh PTS samples. As shown in Supplementary Fig. 58a, a well-aligned fresh PTS specimen exhibited parallel alignment of the Pt(111) plane with the TiO_2(101) plane. Upon increasing magnification to better examine the interfacial structure (Supplementary Figs. 58b–d), we observed beam-induced Pt reconstruction, where the lateral size of a Pt NP increased from 2.02 nm to 2.37 nm, indicating NP spreading. This reconstruction was accompanied by a reduction in the d-spacing from 0.23 nm, characteristic of the Pt(111) plane, to 0.19 nm, corresponding to Pt(200) and (020) planes. During this transformation, the TiO_2(001) surface facilitated partial embedding of Pt into the Ti lattice (Supplementary Figs. 58e, f), resulting in an epitaxial and parallel orientation with the TiO_2(010) and (004) planes. Similar Pt incorporation behavior was previously reported in single-atom Pt/TiO_2 nanosheet systems.[4] This suggests that the structural characteristics of the TiO_2(001) sheet enable enhanced interaction and epitaxial alignment with Pt NPs, promoting a spread morphology and increased interfacial contact area.

We also observed electron beam-induced reconstruction behavior in the fresh PTR sample (Supplementary Figs. 58g–j), albeit with slightly lower image quality. In this case, Pt NPs gradually transformed into sharper cuboctahedral shapes, consistent with the reconstruction behavior observed in the spent PTR sample (Fig. 2j). These transformations are likely driven by oxygen loss from TiO_2 under prolonged high-energy beam exposure. Nonetheless, the observations provide indirect yet supportive evidence for the facet-dependent Pt reconstruction behaviors described in the main text for spent Pt/TiO_2 catalysts.

Supplementary Note 5. Genetic Algorithm-Based Structure Search for Pt_{201}/TiO_2

A genetic algorithm (GA) was employed to identify the most stable configurations of Pt_{201} NPs supported on TiO_2 surfaces. The GA search was performed using the Atomic Simulation Environment (ASE), in which candidate structures were generated, evolved, and evaluated through iterative cycles combined with local structural relaxation using the LBFGS algorithm. Initial Pt_{201} NP candidates were randomly generated above the TiO_2 surface within a predefined three-dimensional region, allowing unbiased sampling of NP positions and orientations while avoiding unphysical overlap with the support. Minimum interatomic distance constraints based on covalent radii were applied during candidate generation to ensure physically reasonable Pt–Pt, Pt–O, and Pt–Ti separations.

To mimic bulk-like behavior of the oxide support, the bottom two atomic layers of the TiO_2 slab were fixed throughout the GA search and subsequent structural relaxation, while all Pt atoms and surface TiO_2 atoms were fully relaxed. The GA was executed with a population size of 20 over 20 generations. New candidate structures were generated using cut-and-splice crossover operations combined with stochastic mutation operations, including mirror and rattle moves, applied with a probability of 0.3. Each candidate structure was locally optimised using the LBFGS algorithm with a force convergence criterion of 0.05 $eV \cdot Å^{-1}$ and a maximum of 200 optimisation steps. The relaxed total energy was used as the fitness score for selection and population update. During the GA evolution, slightly relaxed distance criteria were adopted for Pt–Pt pairs to allow sufficient structural flexibility of the Pt NP while maintaining chemically reasonable bonding environments.

The fitness of each candidate was evaluated based on its total energy after relaxation, and lower-energy structures were preferentially retained in the population for subsequent generations. The GA search was continued until no further improvement in the lowest-energy structures was observed. The final optimised structures reported in this work correspond to the lowest-energy configurations obtained from the GA search for each TiO_2 facet.

The GA workflow was designed to ensure robust convergence of the structure search rather than to impose specific structural motifs. Distance constraints and generation limits were introduced solely to prevent unphysical configurations and numerical instabilities during candidate generation. Importantly, all reported Pt_{201}/TiO_2 structures were fully optimised without constraints on Pt atoms, ensuring that the final geometries reflect intrinsic energetic preferences rather than algorithm-induced bias.

Supplementary Note 6. Construction of Pt_{201}/TiO_2 Models for GNN−MD Simulations

Pt_{201} NPs were generated using an ASE-based Wulff construction and placed on TiO_2 slab models constructed with facet-dependent supercells. For anatase $TiO_2(001)$ and $TiO_2(101)$, stoichiometric slabs were used without introducing oxygen vacancies, and Pt_{201} was positioned above the surface following the same placement protocol prior to relaxation. For each slab model, the Pt_{201} NP was first translated such that its geometric center in the xy plane coincided with the center of the slab surface, while the lowest Pt atom was aligned above the topmost surface layer. The initial vertical separation between the NP and the slab was determined based on the sum of the covalent radii of the surface TiO_2 atoms and the lowest-coordinated Pt atoms, followed by a small additional downward displacement to ensure interfacial contact without unphysical overlap.

To sample different interfacial registries, the Pt_{201} NP was rotated around the surface normal (z axis) in increments of 15°, corresponding to a total of 24 distinct rotational configurations spanning a full 360° rotation. For each rotational orientation, the NP–slab composite structure was generated using the same placement protocol and subsequently subjected to structural relaxation. The total energies of the relaxed configurations were compared, and the lowest-energy structure among the rotational ensemble was selected as the most stable initial configuration for subsequent GNN-MD simulations. All initial structures were subsequently relaxed and used as starting configurations for GNN-MD simulations under identical thermostat and ensemble settings.

Supplementary Note 7. CO-Induced Reconstruction Simulations

CO-induced structural reconstruction of Pt NPs was investigated using a grand-canonical determination of the experimentally relevant CO coverage, followed by structural relaxation and molecular dynamics (MD) simulations under the *in situ* DRIFTS reaction condition. For each optimised Pt_{201}/TiO_2 structure, surface Pt atoms were first identified based on a combined coordination and geometric criterion. Pt–Pt coordination numbers were evaluated using a cutoff distance of 3.0 Å, while interactions with the TiO_2 support (Ti and O atoms) were identified using a cutoff distance of 3.5 Å. Pt atoms with reduced Pt coordination were classified as surface atoms when they were either located at the metal–support interface, positioned far from the cluster center, or exhibited very low Pt coordination. In addition, Pt atoms located near the top of the NP were also considered surface atoms if their coordination number was below a threshold. This procedure enabled robust identification of catalytically accessible surface Pt sites across different NP morphologies.

The thermodynamically stable CO coverage on each Pt_{201}/TiO_2 facet was then identified from a grand-canonical surface phase diagram. The stable number of adsorbed CO molecules, N*, was obtained by minimizing the surface grand potential,

$$\Omega(N) = E(N) - N \cdot \mu_{CO}(T, p_{CO}), \qquad (S7.1)$$

where E(N) is the total energy of the Pt_{201}/TiO_2 system with N CO molecules adsorbed in order of decreasing binding strength, evaluated using the Preferred Potential (PFP) machine learning interatomic potential implemented in the Matlantis platform, and $\mu_{CO}(T, p_{CO})$ is the chemical potential of gas-phase CO, evaluated as

$$\mu_{CO}(T, p_{CO}) = E_{CO}(DFT) + \Delta H(T) - T \cdot \Delta S(T) + k_B T \ln(p_{CO} / p^{\circ}), \qquad (S7.2)$$

where $\Delta H(T)$ and $\Delta S(T)$ were obtained from JANAF thermochemical tables managed by NIST, and the reference pressure $p^{\circ} = 1$ bar. To account for the partial retention of entropy by adsorbed CO through constrained surface modes, an approximate adsorption entropy correction was applied to the effective CO chemical potential using the empirical scaling relation reported by Campbell and Sellers,[12]

$$S_{ads} \approx 0.70 \cdot S_{gas} - 3.3R. \qquad (S7.3)$$

CO adsorption energies were computed individually for every distinct surface Pt site identified above and ranked in order of decreasing binding affinity to construct E(N). The surface grand potential was minimized over N at each (T, p_{CO}) grid point, yielding the two-

dimensional surface phase diagram shown in Supplementary Figs. 28a, b. At the reference condition, matching the *in situ* DRIFTS protocol (T = 513 K, p_{CO} = 0.01 bar), N* corresponded to 39 CO molecules on $Pt_{201}/TiO_2(001)$ (PTS) and 45 CO molecules on $Pt_{201}/TiO_2(101)$ (PTR), as summarised by the adsorption-energy landscapes in Figs. 4e, f and Supplementary Figs. 28c, d.

CO molecules were adsorbed on the N* most strongly binding surface Pt sites using a site-by-site construction protocol. For each selected Pt atom, a CO molecule was placed along an outward direction defined relative to the NP geometry, with a fixed Pt–C distance of 1.85 Å and a C–O bond length of 1.15 Å. To avoid unphysical steric overlap, newly added CO molecules were excluded if the distance between any CO atom and existing atoms was smaller than 1.8 Å; when overlap was detected, the corresponding adsorption site was skipped.

The CO-covered structures were subsequently relaxed using the limited-memory Broyden–Fletcher–Goldfarb–Shanno (LBFGS) algorithm to remove residual forces arising from the initial CO placement. Structural optimisation was performed until the maximum atomic force fell below 0.05 eV $Å^{-1}$. The relaxed CO-covered configurations were then used as initial structures for finite-temperature MD simulations.

MD simulations were carried out in the canonical (NVT) ensemble using a Langevin thermostat at the experimental reaction temperature of 513 K, matching the *in situ* DRIFTS measurement condition. A time step of 1.0 fs was employed, and a friction coefficient of 0.001 was used to ensure stable temperature control while allowing sufficient atomic mobility. Each simulation was propagated for 100,000 MD steps, corresponding to a total simulation time of 100 ps. Atomic trajectories and thermodynamic quantities were recorded at regular intervals throughout the simulation.

To connect the MD trajectories to the *in situ* DRIFTS signal, which reports mainly on CO bound to under-coordinated Pt, the coordination-number (CN) distribution of the CO-adsorbable surface Pt subpopulation, defined as Pt atoms with CN ≤ 9 following the DRIFT-based criterion of Kappers and van der Maas,[13] was extracted before and after each 100 ps trajectory. These simulations enabled direct observation of CO-induced structural rearrangements of Pt NPs under experimentally observed CO-induced Pt roughening.

Supplementary Note 8. Microkinetic Simulations

Microkinetic analysis was performed using the MKMCXX code, an ordinary-differential-equation-based microkinetic solver developed by the group of Ivo Filot at Eindhoven University of Technology, which has been previously applied to CO oxidation on metal and reducible oxide catalysts.[14, 15]

Within this framework, the elementary steps involved in the Mars–van Krevelen CO oxidation mechanism were described by a set of coupled rate equations and solved by time integration until steady-state surface coverages and reaction rates were obtained. Surface states and elementary reaction steps are illustrated below.

[Surface states]

S0: *

(Initial stoichiometric surface with an empty active site)

S1: CO*

(CO adsorbed on metallic Pt site)

S2: O_v*

(Oxygen vacancy formed after CO oxidation)

S3: O_2*O_v

(O_2 adsorbed at an oxygen vacancy)

S4: O*

(Activated oxygen species after O_2 dissociation)

S5: CO* + O*

(Co-adsorbed CO and activated oxygen)

[Elementary reaction steps]

R1: CO(g) + S0 ⇌ S1

(CO adsorption and desorption on Pt)

R2: S1 → S2 + CO_2(g)

(CO oxidation by lattice oxygen and CO formation, vacancy generation)

R3: O_2(g) + S2 ⇌ S3

(O_2 adsorption at oxygen vacancy)

R4: S3 ⇌ S4

(O_2 dissociation and formation of activated oxygen)

R5: CO(g) + S4 ⇌ S5

(CO adsorption adjacent to activated oxygen)

R6: S5 → S2 + CO_2(g)

(CO oxidation by activated oxygen and regeneration of vacancy)

This approach enables a self-consistent description of steady-state kinetics without explicitly assuming a predefined rate-determining step, allowing the relative contributions of adsorption, surface reactions, and lattice oxygen redox processes to be evaluated within a unified kinetic framework.

Gas–surface adsorption and desorption steps were modeled using the Hertz–Knudsen formalism, while surface reaction steps were described by Arrhenius-type rate expressions with activation free energies derived from density functional theory calculations. All thermodynamic quantities were consistently treated in terms of Gibbs free energies, ensuring direct correspondence between DFT-derived energetics and kinetic parameters.

A direct comparison between the calculated per-site MvK turnover frequencies and the experimentally measured CO oxidation rates is summarised in Supplementary Table 7. The model reproduces the experimentally observed facet ordering ($TOF_{PTS} \gg TOF_{PTR}$); the calculated per-site TOFs lie below the measured rates by less than an order of magnitude on PTS and by approximately one order of magnitude on PTR, an offset that falls within the typical accuracy range of DFT-based microkinetic modelling for heterogeneous oxidation.[16]

Supplementary Note 9. Langmuir-Hinshelwood Type Reaction Pathway Energy Profile Calculation

The detailed reaction energy profiles for the L−H pathway are illustrated in Supplementary Fig. 59. Consistent with trends observed for the MvK pathway, the $Pt_{28}/TiO_2(101)$ model exhibits a higher thermodynamic activation barrier (2.19 eV) for the reaction between co-adsorbed *CO and *O where strongly adsorbed CO reacts with oxygen atoms resulting from O_2 dissociation, compared to 0.64 eV for the $Pt_{28}/TiO_2(001)$ model. This step is recognized as the RDS in the L-H mechanism. Among the elementary steps, CO adsorption is often critical for overall efficiency due to its strong interaction with Pt surfaces.[17] CO binding strengths on Pt sites were evaluated by COHP analysis of Pt-C(O) bonds (Supplementary Fig. 60). The calculated ICOHP value for the Pt-C bond was 3.09 for $Pt_{28}/TiO_2(001)$, significantly lower than 3.30 for $Pt_{28}/TiO_2(101)$, indicating stronger Pt-CO interaction in the $Pt_{28}/TiO_2(101)$ system. This is consistent with the lower energy state of CO adsorbed on $Pt_{28}/TiO_2(101)$ for both pathways and with CO-TPR experiments, where CO desorption from PTR requires higher temperatures than from PTS (Supplementary Fig. 6).

Supplementary Note 10. Challenges in Interpreting NAP-XPS Spectra

To gain a comprehensive understanding of the surface chemical states and valence behavior of the catalysts, we analyzed the *in situ* NAP-XPS spectra of the Pt 4*f* region for each sample. As shown in Supplementary Fig. 61, it is important to note that interpretation of the Pt 4*f* region is complicated by the overlap with the Ti 3*s* energy loss feature located near ~75 eV.[4, 18] This spectral interference poses a significant challenge to accurate quantification of the Pt 4*f* signals.

The issue is particularly pronounced for TiO_2-S and its corresponding Pt/TiO_2 catalyst, compared to TiO_2-R, due to the relatively low surface density of Pt NPs. Despite similar Pt loading and NP size, the larger surface area of the TiO_2 nanosheets in TiO_2-S results in a more dilute distribution of Pt, further complicating the detection and deconvolution of Pt 4*f* signals.

Moreover, variations in the Ti 2*p* and O 1*s* core-level spectra were minimal, likely due to the small contribution of interfacial Pt–TiO_2 interactions relative to the overwhelming signal from bulk TiO_2. Given these challenges—including spectral overlap, weak Pt signal intensity, and the low proportion of reactive interfacial zones relative to the support bulk—we focused our attention on the O 1*s* region.

Specifically, we examined the behavior of the carbonate-related C=O peak and the corresponding evolution of the CO_2(g) signal under CO oxidation conditions. These features provide more interpretable and reliable insights into the dynamic changes occurring at the catalyst surface during reaction, particularly at the Pt–TiO_2 interface.

Supplementary Note 11. Facet-Dependent Properties of Oxygen Species on TiO_2

In addition to carbonate-related species, we further considered the role of oxygen-vacancies (O_v), which are widely recognized as a critical factor governing the catalytic activity of oxide-supported catalysts.[19] O_v are commonly evaluated via O 1*s* XPS analysis, where the relative contribution of adsorbed oxygen or surface hydroxyl–related components is used as an indirect descriptor of O_v concentration.[20, 21] Following this established approach, we performed a comparative analysis of O 1*s* XPS spectra for both pristine TiO_2 supports and Pt/TiO_2 catalysts measured under UHV conditions, as well as for Pt/TiO_2 catalysts measured under CO oxidation conditions at 227 and 277 °C.

Under reactive gas environments, the O 1*s* region is further complicated by overlapping contributions from gas-phase intermediates (e.g., C–O and C=O species). Therefore, rather than comparing the total O 1*s* intensity (O_{total}), we evaluated the O_{ads}/O_{latt} area ratios to enable a consistent relative comparison of O_v-related oxygen species with respect to bulk lattice oxygen. In addition, because the presence of gas molecules induces significant inelastic scattering of photoelectrons—leading to signal attenuation, peak broadening, and reduced surface sensitivity—our analysis was restricted to relative comparisons of O_{ads}/O_{latt} ratios between catalysts measured under identical environments, rather than absolute quantification across different conditions.

O 1*s* XPS analyses under UHV conditions (Supplementary Figs. 37a, b) show that pristine $TiO_2(001)$ and PTS exhibit O_{ads}/O_{latt} ratios—as a descriptor of O_v abundance—that are 1.76 and 1.95 times higher, respectively, than those of their $TiO_2(101)$ counterparts, indicating that the (001) facet intrinsically possesses a higher abundance of O_v–related sites irrespective of Pt loading. O 1*s* XPS analyses under reaction environments (Supplementary Figs. 37c, d) further show that PTS exhibits a pronounced decrease in the O_{ads}/O_{lat} ratio with increasing temperature (from 0.56 to 0.38), whereas PTR shows only a marginal change (from 0.53 to 0.51), consistent with more efficient oxygen transfer from the $TiO_2(001)$ support to interfacial Pt sites In line with this trend, O_2-temperature-programmed desorption (O_2-TPD) profiles of Pt/TiO_2 and pristine TiO_2 (Supplementary Fig. 38a) exhibit two broad peaks between 100 and 300 °C and between 300 and 600 °C attributed to the superoxide (O_2^-) and peroxide (O^-) species, respectively.[22] The calculated oxygen storage capacity (Supplementary Fig. 38b) increased substantially on the (001) facet from 9.65 to 18.17 $\mu mol \cdot m^{-2}$ upon Pt loading, whereas the (101) facet showed a smaller increase from 11.97 to 16.58 $\mu mol \cdot m^{-2}$. The desorption peak temperatures for PTS were also lower than those for PTR and the pristine supports, indicating

the presence of more reactive oxygen species at the Pt–TiO_2 interface, driven by the stronger MSI on the (001) facet. Electron paramagnetic resonance (EPR) spectra (Supplementary Fig. 39) confirm the presence of superoxide radicals ($O_2^{\bullet-}$) with signals at g = 2.001–2.033 in PTS, while no such signals are observed for pristine TiO_2 rhombic and PTR samples.[23, 24, 25, 26] Overall, these results demonstrate that the TiO_2(001) facet intrinsically possesses a higher abundance of O_v and more reactive oxygen species, which are further promoted at the Pt–TiO_2 interface by stronger MSI.

Supplementary Note 12. Evaluating Reduction/O_v-related Contributions to Catalytic Activation

To examine the possible influence of surface reduction and changes in O_v-related oxygen species on the activity enhancement after the first catalytic run, post-reaction O 1*s* analyses and H_2 pretreatment experiments were performed. The post-reaction O 1*s* analyses compared the surface oxygen states of PTS and PTR after CO oxidation, while the H_2 pretreatment experiments provided a reductively modified Pt/TiO_2 state for comparison with the catalyst state evolved during CO oxidation. As shown in Supplementary Fig. 42, the initially higher O_{ads}/O_{lat} ratio of PTS relative to PTR became comparable after CO oxidation, both after the *in situ* NAP-XPS reaction sequence and after the first catalytic run. Together with the catalytic cycle results, where PTS shows an additional E_a decrease from the 2nd run onward whereas PTR remains nearly unchanged, this result indicates that the enhanced activity of PTS after the first run cannot be described simply by the initial O_v abundance.

H_2 pretreatment was performed in 10% H_2/Ar at 400 °C for 1 h with a total flow rate of 50 mL·min^{-1}. This condition was selected based on the H_2-TPR profile, where Pt-related reduction occurs below ~250 °C and the broader feature around ~350 °C is associated with H_2-spillover-assisted partial reduction of surface TiO_2 species adjacent to Pt. After H_2 pretreatment, both PTS and PTR showed enhanced initial CO oxidation activity, with lower 1st-run E_a values and improved light-off behaviour compared with the corresponding fresh catalysts (Supplementary Fig. 43). However, different trends were observed during subsequent catalytic runs. For PTS, the E_a decreased from 53.8 kJ mol^{-1} in the 1st run to 47.5 and 43.6 kJ mol^{-1} in the 2nd and 3rd runs, respectively, reaching the low-E_a state observed in the original catalytic cycling test. In contrast, PTR maintained similar E_a values over repeated runs after H_2 pretreatment, changing from 87.6 to 89.2 and 89.3 kJ mol^{-1} from the 1st to 3rd runs. These results show that reductive pretreatment enhances the initial activity of both catalysts, but the additional E_a decrease during subsequent CO oxidation occurs only for PTS. Pt size distributions and STEM analyses after the 3rd run over the H_2-pretreated catalysts showed no significant Pt NP growth or apparent degradation of the TiO_2 support morphology, indicating that the observed catalytic evolution is not associated with Pt sintering or support morphological degradation (Supplementary Fig. 44).

The O 1*s* spectra of the H_2-pretreated catalysts further show that the relative contribution of high-binding-energy O 1*s* components increased after H_2 pretreatment for both catalysts (Supplementary Fig. 45). These components include adsorbed oxygen, hydroxyl species,

water-related species, and defect-associated surface oxygen, which are used as indirect descriptors of O_v-related surface states. After the 3rd catalytic run following H_2 pretreatment, the O 1*s* spectral features of PTS and PTR again became comparable, consistent with the post-reaction O 1*s* results described above.

Taken together, these results show that reductive surface modification and O_v-/hydroxyl-related surface oxygen species contribute to the catalytic behaviour of Pt/TiO_2 catalysts. However, the enhanced activity of PTS after the first catalytic run cannot be described solely by the initial O_v abundance or by reductive surface modification. Rather, the kinetic and O 1*s* results support that the low-E_a state of PTS is associated with the reaction-evolved Pt–TiO_2(001) interfacial structure, which provides a favourable environment for support-oxygen participation during CO oxidation.

Supplementary Note 13. Indirect Evaluation of O_v-Related Catalytic Contributions and O_v Effects on Facet-dependent Pt Structural Evolution

Pt/Al_2O_3 (PtA) was examined as a qualitative reference for Pt supported on an irreducible oxide. Although PtA shows a Pt size distribution comparable to those of PTS and PTR (Supplementary Figs. 46a–c and Supplementary Table 1), it is not considered a direct structural analogue of the Pt/TiO_2 catalysts because Al_2O_3 is an irreducible support that does not provide a well-defined facet-controlled surface and exhibits different metal–support interactions from TiO_2. Therefore, the PtA results are used only to provide qualitative context for Pt behaviour on an irreducible support, rather than for quantitative comparison of catalytic activity or Pt structural evolution with the Pt/TiO_2 catalysts.

PtA exhibited a relatively high E_a (Supplementary Fig. 47) among the examined catalysts, consistent with the limited involvement of support oxygen on irreducible Al_2O_3 and the predominance of a Pt-surface-mediated L–H pathway.[27] Unlike the spectral evolution observed for Pt/TiO_2 catalysts during CO-DRIFTS experiments (Fig. 3), the normalized pre- and post-reaction CO-DRIFTS spectra of PtA were nearly unchanged (Supplementary Fig. 48a). However, the *in situ* DRIFTS contour map showed a pronounced redshift of the CO–$Pt_{step/edge}$ feature during reaction (Supplementary Figs. 48b and 49), indicating that PtA also undergoes CO-induced spectral changes in Pt surface coordination. In addition, the temperature-resolved CO_2(g) and CO–$Pt_{step/edge}$ intensity profiles showed persistent CO adsorption accompanied by a weak CO_2(g) signal (Supplementary Fig. 48c). These observations suggest that, although CO-induced Pt surface roughening can also occur on PtA, the Pt surface remains strongly CO-covered and less effective for CO oxidation, consistent with L–H-type behaviour without direct support-oxygen participation.[27] Thus, PtA is used here as a qualitative irreducible-support reference to distinguish reversible CO-induced Pt surface roughening from the more persistent reaction-evolved Pt–TiO_2 interfacial restructuring observed on reducible TiO_2.

To further examine how O_v influence facet-dependent Pt morphology within the Pt/TiO_2 system, we performed additional GA-optimised simulations using O_v-modulated TiO_2 models. The original GA optimisation for the Pt_{201}/TiO_2 models (Figs. 4a, b) was carried out on stoichiometric anatase TiO_2 facets without introducing O_v, to isolate the role of TiO_2 surface geometry itself in determining facet-specific equilibrium Pt morphologies. Even in the absence of O_v, these calculations already revealed a pronounced facet dependence in Pt wetting, with the effective contact angle on TiO_2(001) (95.7°) substantially lower than that on

TiO_2(101) (118.7°). This ~23° difference indicates that the intrinsic geometric characteristics of the TiO_2 facet alone are sufficient to generate the distinct Pt morphologies observed experimentally, without invoking O_v as a prerequisite.

At the same time, the real catalyst system is expected to contain facet- and condition-dependent O_v populations, which may additionally influence Pt morphology through local changes in metal–support interactions. To examine this effect directly, we performed additional GA optimisations using O_v-modulated TiO_2 models containing 10% surface O_v in the relaxed top two layers, corresponding to 5% of the total lattice oxygen in the slab. O_v were placed within the top two layers with a minimum inter-vacancy separation of 5 Å to preserve the dilute-limit interpretation of isolated defects. This concentration falls within the 5–10% range commonly used in DFT studies of anatase oxygen vacancies.[28, 29] Three independent GA optimisations were carried out for each facet using distinct randomly generated O_v distributions to account for configurational variability in vacancy placement. The corresponding GA energy convergence profiles are shown in Supplementary Fig. 50.

The additional GA-optimised simulations reveal a clear facet dependence in the structural response to O_v (Supplementary Fig. 51). On TiO_2(001), introducing O_v leaves the Pt contact angle nearly unchanged, from 95.7° for the stoichiometric surface to 94.3–99.9° (mean 96.5°) across the three O_v-containing realizations, indicating that Pt wetting on this facet is governed primarily by intrinsic surface geometry rather than by O_v. By contrast, on TiO_2(101), introducing 10% surface O_v decreases the Pt contact angle from 118.7° to 102.4–108.2° (mean 104.6°), showing that O_v can partially promote Pt wetting on this facet. However, even at 10% surface O_v, Pt/TiO_2(101) still retains a contact angle on average approximately 8° higher than that of Pt/TiO_2(001).

Notably, the O 1*s* XPS results show that the O_v-related oxygen ratio on TiO_2(101) is only about one-half of that on TiO_2(001). To reflect this experimentally observed asymmetry, we additionally performed GA optimisation for Pt/TiO_2(101) at 5% surface O_v, corresponding to 2.5% of the total lattice oxygen. The resulting contact angles from three independent realizations were 108.2°, 122.0°, and 116.1° (mean 115.4°), remaining close to the value for stoichiometric TiO_2(101). These results indicate that, although O_v can modulate local Pt wetting, they do not override the dominant role of facet-dependent TiO_2 surface geometry and its resulting MSI in determining the experimentally observed Pt morphology.

Taken together, the PtA results provide a qualitative irreducible-support reference showing that CO-induced Pt surface roughening can occur without persistent Pt–support interfacial

restructuring. In parallel, the O_v-modulated GA simulations evaluate O_v effects within the Pt/TiO_2 framework and show that O_v can locally influence Pt wetting, but does not override the facet-dependent morphology trend. These results indicate that O_v-related effects and support reducibility can influence Pt structural evolution, while the enhanced reactivity of PTS is more consistently understood as the combined contribution of higher O_v-related redox reactivity and a reaction-evolved $Pt–TiO_2(001)$ interfacial configuration derived from the initially wetted Pt morphology.

Supplementary Note 14. Graph Neural Network Potential and Validation

Large-scale molecular dynamics (MD) simulations in this study were performed using a graph neural network (GNN) interatomic potential, the Preferred Potential (PFP, version 4.0.0), as implemented in the Matlantis platform. PFP is a pre-trained, universal neural network potential developed by Preferred Networks and is designed to reproduce density functional theory (DFT)-level energies and forces across a wide range of chemical environments, including bulk materials, surfaces, cluster, and disordered structures.

As a proprietary pre-trained model, detailed architectural parameters and training hyperparameters are defined by the developer and were not modified in this study. The performance of PFP has been benchmarked in previous reports,[30, 31] showing mean absolute errors (MAEs) of approximately 5–14 meV per atom for total energies and 0.065–0.13 eV·Å^{-1} for atomic forces, indicating DFT-level accuracy suitable for MD simulations.

To further validate the applicability of PFP to the Pt/TiO_2 systems studied here, we directly compared PFP predictions with DFT reference calculations for representative properties (Supplementary Fig. 62). First, the formation energies of Pt clusters spanning a wide size range (approximately 5–55 atoms) were evaluated. The resulting parity plot demonstrates excellent agreement between PFP and DFT, with a mean absolute error of 0.043 eV per atom across the entire size range (Supplementary Fig. 62a). Second, adsorption energies of key species involved in the CO oxidation reaction (CO, O_2, and O) on Pt/TiO_2 catalyst surfaces were compared between PFP and DFT calculations. An MAE of approximately 0.22 eV was obtained for adsorption energies (Supplementary Fig. 62b), which is sufficient for identifying facet-dependent trends in adsorption energetics and reaction pathways. Third, force convergence during structural relaxation closely matches DFT results, confirming the reliability of PFP for geometry optimisation and MD simulations (Supplementary Fig. 62c).

Overall, these validation results demonstrate that PFP reliably reproduces DFT trends for Pt cluster energetics, adsorption energies, and force predictions within the scope relevant to this work. This level of accuracy justifies the use of PFP for capturing facet-dependent structural dynamics and CO-induced reconstruction phenomena of Pt NPs supported on TiO_2 surfaces.

Supplementary References

1. Boubnov, A. et al. Oscillatory CO oxidation over Pt/Al_2O_3 catalysts studied by in situ XAS and DRIFTS. *Top. Catal.* **56**, 333-338 (2013).
2. DeRita, L. et al. Catalyst Architecture for Stable Single Atom Dispersion Enables Site-Specific Spectroscopic and Reactivity Measurements of CO Adsorbed to Pt Atoms, Oxidized Pt Clusters, and Metallic Pt Clusters on TiO_2. *J. Am. Chem. Soc.* **139**, 14150-14165 (2017).
3. Yu, J. et al. Enhanced photocatalytic CO_2-reduction activity of anatase TiO_2 by coexposed {001} and {101} facets. *J. Am. Chem. Soc.* **136**, 8839-8842 (2014).
4. Zang, W. et al. Distribution of Pt single atom coordination environments on anatase TiO_2 supports controls reactivity. *Nat. Commun.* **15**, 998 (2024).
5. Liu, L. et al. Crystal-plane effects on the catalytic properties of Au/TiO_2. *ACS Catal.* **3**, 2768-2775 (2013).
6. Yang, M.H. et al. Alkali metal ion assisted synthesis of faceted anatase TiO_2. *CrystEngComm* **15**, 2966-2971 (2013).
7. Jia, A. et al. Selective hydrogenation of crotonaldehyde over Ir/TiO_2 catalysts: unraveling the metal-support interface related reaction mechanism. *J. Catal.* **425**, 57-69 (2023).
8. Tang, M. et al. Facet-Dependent Oxidative Strong Metal-Support Interactions of Palladium-TiO_2 Determined by In Situ Transmission Electron Microscopy. *Angew. Chem. Int. Ed.* **60**, 22339-22344 (2021).
9. Yuan, W. et al. Direct In Situ TEM Visualization and Insight into the Facet-Dependent Sintering Behaviors of Gold on TiO_2. *Angew. Chem. Int. Ed.* **57**, 16827-16831 (2018).
10. Ro, I. et al. Approaches for understanding and controlling interfacial effects in oxide-supported metal catalysts. *ACS Catal.* **8**, 7368-7387 (2018).
11. Allian, A.D. et al. Chemisorption of CO and mechanism of CO oxidation on supported platinum nanoclusters. *J. Am. Chem. Soc.* **133**, 4498-4517 (2011).
12. Campbell, C.T. et al. The entropies of adsorbed molecules. *J. Am. Chem. Soc.* **134**, 18109-18115 (2012).
13. Kappers, M. et al. Correlation between CO frequency and Pt coordination number. A DRIFT study on supported Pt catalysts. *Catal. Lett.* **10**, 365-373 (1991).
14. Chang, M.-W. et al. Dynamics of gold clusters on ceria during CO oxidation. *J. Catal.* **392**, 39-47 (2020).
15. Chen, C. et al. Reactant-induced dynamic stabilization of highly dispersed Pt catalysts on ceria dictating the reactivity of CO oxidation. *ACS Catal.* **14**, 3504-3513 (2024).
16. Xie, W. et al. Achieving theory–experiment parity for activity and selectivity in heterogeneous catalysis using microkinetic modeling. *Acc. Chem. Res.* **55**, 1237-1248 (2022).
17. Bosio, N. et al. Interface Reactions Dominate Low-Temperature CO Oxidation Activity over Pt/CeO_2. *J. Phys. Chem. C* **126**, 16164-16171 (2022).
18. Chen, J.J. et al. Reverse oxygen spillover triggered by CO adsorption on Sn-doped Pt/TiO_2 for low temperature CO oxidation. *Nat. Commun.* **14**, 3477 (2023).
19. Ruiz Puigdollers, A. et al. Increasing oxide reducibility: the role of metal/oxide interfaces in the formation of oxygen vacancies. *ACS Catal.* **7**, 6493-6513 (2017).
20. Huang, H. et al. Complete oxidation of formaldehyde at room temperature using TiO_2 supported metallic Pd nanoparticles. *ACS Catal.* **1**, 348-354 (2011).
21. Lee, J. et al. Reversible Pd catalysts supported on hierarchical titanate nanosheets for an N-methylindole-based liquid organic hydrogen carrier. *ACS Catal.* **13**, 13691-13703 (2023).

22. He, K.L. In situ DRIFTS and TPD studies on surface properties affecting SO_2-resistance of Pt/TiO_2 catalyst in low-temperature CO oxidation. *Surf. Sci.* **734**, 122315 (2023).
23. Hayyan, M. et al. Superoxide Ion: Generation and Chemical Implications. *Chem. Rev.* **116**, 3029-3085 (2016).
24. Lee, C.W. et al. Photochemical tuning of dynamic defects for high-performance atomically dispersed catalysts. *Nat. Mater.* **23**, 552-559 (2024).
25. Collado, L. et al. Unravelling the effect of charge dynamics at the plasmonic metal/semiconductor interface for CO photoreduction. *Nat. Commun.* **9**, 4986 (2018).
26. Feng, N. et al. Efficient and selective photocatalytic CH_4 conversion to CH_3OH with O_2 by controlling overoxidation on TiO_2. *Nat. Commun.* **12**, 4652 (2021).
27. Kale, M.J. et al. Utilizing Quantitative FTIR Spectroscopy To Identify Well-Coordinated Pt Atoms as the Active Site for CO Oxidation on Al_2O_3-Supported Pt Catalysts. *ACS Catal.* **6**, 5599-5609 (2016).
28. Cheng, H. et al. Energetics and diffusion of intrinsic surface and subsurface defects on anatase TiO_2(101). *J. Chem. Phys.* **131**, 054703 (2009).
29. Elahifard, M. et al. Dispersion of defects in TiO_2 semiconductor: Oxygen vacancies in the bulk and surface of rutile and anatase. *Catalysts* **10**, 397 (2020).
30. Takamoto, S. et al. TeaNet: Universal neural network interatomic potential inspired by iterative electronic relaxations. *Comput. Mater. Sci.* **207**, 111280 (2022).
31. Takamoto, S. et al. Towards universal neural network potential for material discovery applicable to arbitrary combination of 45 elements. *Nat. Commun.* **13**, 2991 (2022).